October 2019

POLYMERIC IMPULSIVE ACTUATION MECHANISMS: DEVELOPMENT, CHARACTERIZATION, AND MODELING

Yongjin Kim
University of Massachusetts Amherst

POLYMERIC IMPULSIVE ACTUATION MECHANISMS:

DEVELOPMENT, CHARACTERIZATION, AND MODELING

A Dissertation Presented

by

YONGJIN KIM

Submitted to the Graduate School of the
University of Massachusetts Amherst in partial fulfillment
of the requirements for the degree of

DOCTOR OF PHILOSOPHY

September 2019

Polymer Science and Engineering

POLYMERIC IMPULSIVE ACTUATION MECHANISMS:

DEVELOPMENT, CHARACTERIZATION, AND MODELING

A Dissertation Presented

by

YONGJIN KIM

Approved as to style and content by:

_____
Alfred J. Crosby, Chair

_____
Ryan C. Hayward, Member

_____
Christian D. Santangelo, Member

_____
E. Bryan Coughlin, Department Head
Polymer Science & Engineering

DEDICATION

To my family

ACKNOWLEDGMENTS

First and foremost, I would like to thank my thesis advisor, Professor Al Crosby, for guiding me throughout my Ph.D. studies. Al has been a great advisor, mentor, and father of his family, always showing me the best examples of how I mush think like, work like and live like. I will always keep the lessons in mind. Additionally, I want to express my thank to Kerry for her interest in my family.

I would like to thank my committee members, Professors Ryan Hayward and Christian Santangelo for providing thoughtful suggestions and questions that helped me developing my researches.

I must thank all of the past members of the Crosby group. Pham, Han Yu, Marcos, Mikey, Dan, Yujie, Yucheng, Minchao, Richard, Satyan, and Shruti for helping me adjust to the group and teaching me how to conduct research. Your knowledge, passion, and warmth led me to choose the best research group and encouraged me to pursue my Ph.D. studies.

I would like to thank present group members, Chao, Keith, Xudong, Konane, Chris, Dylan, Hannah, Cindy, Hongbo, and Meredith for devoting their valuable times and efforts for correcting and polishing my presentations and writings. I really appreciate and value each one of the Crosby group members and I am so proud of the fact that I am one of the Crosby group members who care each other and endeavor to make the group better. Chya Yan, Mark, Chris, and Chao, thanks for being great roommates. Every day was so fun and memorable moments.

Outside of the group, I would like to thank Jay and Tim who worked with me for the snapping-shell project and many other unfinished works. I hope you still have great interests in Science and wish you the best of luck. I would like to thank Doug for helping me with developing analytical models and teaching me Mathematica. I would like to thank all MURI team members for great discussions and for inspiring me with different domain of sciences. I would like to thank my Korean friends, Woojin, Jihwan, Dukman, Hyeyoung, Janghun, Hyunki, Juyoung, Minjung, Soeun, Hyeongjun, Jaechul, Jaejun, and Hongkyu for helping each other.

Especially, I want to thank Hyunki, Konane, and Keith for being always supportive and reliable. I wouldn't have been able to finish my Ph.D. without you.

Lastly, I would like to thank my parent, family, and my wife, Minju for endless supports, sacrifices, and love.

ABSTRACT

POLYMERIC IMPULSIVE ACTUATION MECHANISMS: DEVELOPMENT, CHARACTERIZATION, AND MODELING

SEPTEMBER 2019

YONGJIN KIM, B.S., SEOUL NATIONAL UNIVERSITY

M.S., UNIVERSITY OF MASSACHUSETTS AMHERST

Ph.D., UNIVERSITY OF MASSACHUSETTS AMHERST

Directed by: Professor Alfred J. Crosby, Ryan C. Hayward and Christian D. Santangelo

Recent advances in the field of biomedical and life-sciences are increasingly demanding more life-like actuation with higher degrees of freedom in motion at small scales. Many researchers have developed various solutions to satisfy these emerging requirements. In many cases, new solutions are made possible with the development of novel polymeric actuators. Advances in polymeric actuation not only addressed problems concerning low degree of freedom in motion, large system size, and bio-incompatibility associated with conventional actuators, but also led to the discovery of novel applications, which were previously unattainable with conventional engineered systems.

This dissertation focuses on developing novel actuation mechanisms for soft polymeric gel systems with easily adjustable mechanochemical properties and applicability to various environmental conditions. Inspired by stunning examples in nature which exhibit extremely fast motion in a repeatable manner, termed impulsive

motion, we have developed polymeric gel actuators applicable for small-scale, self-contained impulsive systems.

In particular, we focused on the effect of geometry and the mechanics of surface-mediated stresses on the dynamic shape-change of polymer gel actuators. We found new opportunities from observation of transient deformations which occur during swelling, or deswelling, of asymmetric gels. We described the development of time-dependent three-dimensional deformation mechanism (4D fabrication) by the utilization of transient inhomogeneous swelling state of the asymmetric polymer gel. We discussed the mechanism and the application of the new deformations mechanism for the development of a novel functionality: chemical gradient sensor.

In addition, we developed a high-rate and large-strain reversible actuation mechanism for sub-micrometer scale polymeric gel actuators by utilizing balanced effects of two surface-mediated phenomena, surface diffusion and interfacial-tension, and elasticity of soft and small-scale hydrogels.

These new findings were harnessed for developing autonomously controlled power amplified polymeric gel devices. Utilizing deswelling induced transient deformation of gel, we developed design principles for generating meta-stable structures and inducing self-regulating transition forces for repeated snap-through buckling transition of polymeric gel devices.

In parallel, we deconvoluted the effect of material properties and geometry on dynamic deformations by establishing simulation models and conducting analyses on the performances of actual synthetic systems. The systematic approach will serve to broaden the application spectrum and manufacturing possibilities of polymeric actuator systems.

TABLE OF CONTENTS

Page

LIST OF FIGURES

Figure Page

CHAPTER 1

INTRODUCTION

1.1 Motivation and overview

Actuators are devices that can convert energy to mechanical work [1, 2]. Conventionally, engineered actuators have been made of inorganic materials (mostly, metals and ceramics) adopting various drive mechanisms, including electromagnetic (motor), electrostatic (comb-drive actuator [3]), piezoelectric (piezo-actuator [4]), crystallographic movement (shape-memory alloy [5]), or pneumatic (hydraulic cylinders). These actuators exhibit advantages in structural robustness, precision, and responsiveness. On the other hand, due to the nature of inorganic materials and the drive mechanism, such actuators are rigid, heavy and limited in degrees of freedom of movement.

Recent advances in the field of biomedical sciences and life-sciences, meanwhile, are increasingly demanding more life-like actuation with higher degrees of freedom in motion at small scales [6]. Many researchers have developed various solutions to satisfy emerging requirements. In many cases, the new solutions were made possible with the development of novel polymeric actuators [7–9]. The advances not only tackled problems of inorganic actuators but also led to the discovery of novel applications, which were unavailable with the conventional engineered systems.

Various novel applications that could benefit from the development of polymeric actuation systems are presented in Figure 1.1 Harnessing soft and transparent characteristics of hydrogels, pneumatic actuation of hydrogel grips could minimize the damage and stress while manipulating a live aquatic animal [7]. Increased degrees of

freedom of the movements and the biocompatible nature of soft actuators could bring the reduction of invasive procedures [8]. Moreover, advances in actuation systems opened up more opportunities to unravel secrets of nature. For examples, soft robotic fish, developed by Katzschmann and coworkers, provided more information on aquatic animals by approaching them closely without attracting attention [9].

Examples of novel aspects of polymeric actuators are:

- Wide ranges of mechanical properties (modulus: 1 kPa ~ 10 GPa)
- Biocompatibility and biodegradability
- Ease of processing (i.e., 3D printing, molding)
- Unique properties (i.e., transparency, chemical affinity to solvent, stimuli responsiveness)

For these reasons, endeavoring for the development of novel actuation mechanism and new fabrication strategies is critical for the advance of technologies, which will contribute to the enhancement quality of life and the harmonious coexistence of human and nature.

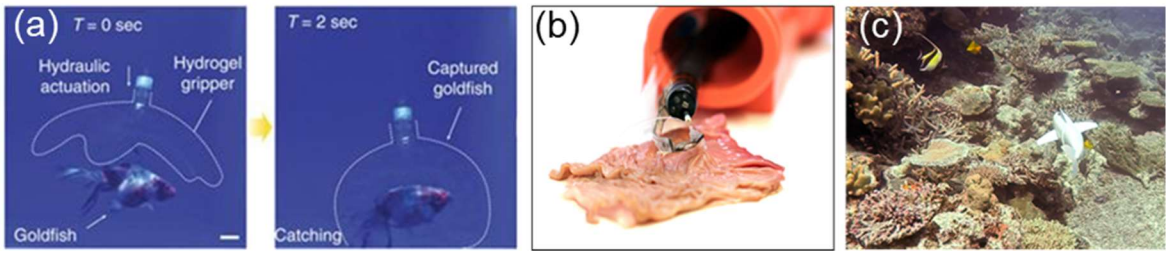

Figure 0.1. Images of soft robots demonstrating their functionality. (a) Hydraulic transparent hydrogel gripper. Reprinted with permission from ref [7]. (b) Soft endoscopic robot. Reprinted with permission from ref [8]. (c) Soft robotic fish. Reprinted with permission from ref [9].

1.2 Thesis organization

Among the many polymeric actuation systems, we have chosen to study polymeric gel systems due to the advantages of easily adjustable mechanochemical properties and applicability to various environmental conditions. Moreover, knowledge acquired from gel-based actuation system can be adapted to other volume-change-induced actuation mechanisms (i.e., heat expansion, pneumatic system).

We have found new opportunities from transient deformations occurring during swelling or deswelling of gel and the interfacial tension change of a specific material for generating active deformation in mesoscale. These new findings were harnessed for overcoming current limitations in the swelling induced actuation systems concerning slow dynamics and size scale. Furthermore, we demonstrated new functionality such as autonomous controls to polymeric actuator systems based on the nature of transient deformations.

In parallel, we deconvoluted the effect of material properties and geometries on the dynamic deformations by establishing simulation models and conducting analyses on the performances of actual systems. The systematic approach will serve to broaden application spectrum and manufacturing possibilities of polymeric actuator systems.

This thesis is organized into an introduction, three experimental sections, and a concluding section. The first chapter provides a background review of polymeric actuation systems focusing on the possibilities and challenges of swelling induced actuation. It will cover:

- Hydration induced shape morphing mechanism in plant systems and equivalents in engineered systems

- Thermodynamics and diffusion dynamics in the solvent swelling phenomena of polymer gels
- Previous approaches for tackling limitations in kinetic performances of gel-based actuators

In the second section, we describe the development of time-dependent three-dimensional deformation mechanism (4D fabrication) by the utilization of transient inhomogeneous swelling state of the asymmetric polymer gel. In this chapter, we discuss:

- A new global deformation mechanism (non-zero Gaussian curvature and mean curvature) based on the transient swelling inhomogeneity of polymer gels with asymmetric geometries under a homogeneous swelling condition
- Experimental details for the deconvolution of the effect of material properties and geometries on the dynamics and the extent of deformations
- Discussion on the application of the new deformation mechanism for the development of a novel functionality: chemical gradient sensor

In the third section, we deal the development of high-rate and large-strain reversible actuation of sub-micrometer scale polymer gel. In this chapter, we discuss:

- A new deformation mechanism based on the balanced effects of two surface-mediated phenomena (surface tension and surface diffusion) and elasticity on the control of shape transformation of a compliant object

- Application of the micro-assembly technique established in the Crosby group to generate reversible deformation of compliant (low modulus or thin) object adapting the two surface-mediated phenomena. Experimental details on estimating solid-liquid interfacial tension of stimuli-responsive hydrogels
- Discussions on the effect of material properties, geometries, and the dynamical environmental condition on the kinetics of mesoscale actuator

In the fourth section, we explain how autonomously controlled power amplified polymer gel devices were developed based on deswelling induced transient deformation mechanism. In this chapter, we discuss:

- Introduction of the new autonomous control mechanism for generating meta-stable structures and inducing self-regulating transition forces for repeated snap-through buckling transition of polymer gel devices.
- Experimental details for the understanding of design principles for an autonomous motion and the dependence of the kinetic performances on the material properties and geometries
- Discussion on the tunable kinetic performance of autonomous snap jumping shells

1.3 Shape morphing mechanism in natural and synthetic systems

Despite the absence of active muscle-contraction mechanism, botanical systems have evolved simple yet effective ways of generating motions (or deformations) in their

stems, leaves, or flowers by harnessing hydration induced volume change of porous matrices. Shape morphing phenomena of plant systems are astonishingly diverse regarding the diversity of shapes, as well as the kinetic performances. For example, morphogenesis in growing tissues such as climbing stems of bines and vines happens over hours or days in helical conformation [10]. On the contrary, explosive seed dispersal of *Cardamine hirsuta* [11], or snap closing of Venus flytrap [12], can be finished within milliseconds through a sophisticatedly selected shape morphing process.

Inspired by the various examples observed in nature, intensive studies have been conducted with the purpose of 1) enabling complex deformations in a predictable manner, 2) understanding the thermodynamics of the swelling induced deformation, and 3) mimicking the extraordinary kinetic performances of certain bio-organisms.

1.3.1 **Multi-component composites for prescribed three-dimensional deformation**

Studies on how plant systems can exhibit dynamic morphological change revealed that the inhomogeneous generation of turgor pressure causes the deformation of initial geometries [13, 14]. Where turgor refers a pressure exerted by plasma membrane on a rigid cell wall of plants. Turgor increases as a cell become more hydrated and vice versa [10]. The inhomogeneity was imposed by the anisotropic distributions of cellulose fibrils in cell walls (Figure 1.2) that have been prescribed in their gene or evolved later in response to the environmental conditions [13].

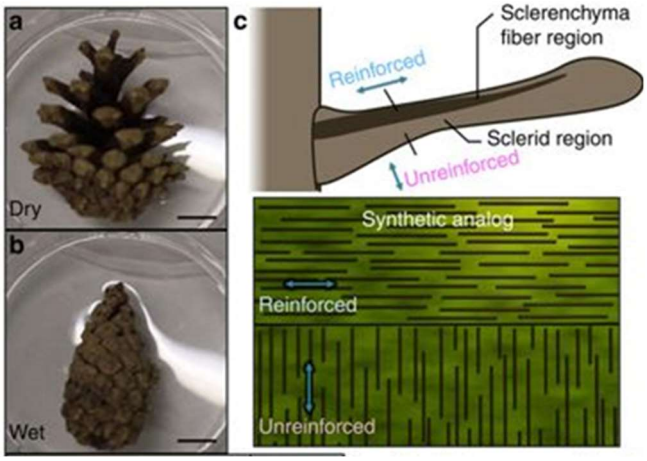

Figure 0.2 Hydration induced deformation of the pine cone and the hierarchical alignment of reinforcing fibers. Reprinted with permission from ref [15].

Inspired by the analogy between the turgor pressure and swelling pressure (stress arose by swelling of confined gel), many types of engineering principles were developed such as self-shaping bilayer composites [16] and four-dimensional printing [17]. The efficacy of these methods relies on the anisotropy between the transversal swelling (direction perpendicular to the aligned fiber reinforcements) and longitudinal swelling (direction parallel to the aligned fiber reinforcements) of fiber filled hydrogel [17]. The degree of anisotropy could be controlled by altering the degree of alignment and contents of fibrous fillers. In Figure 1.3, various deformations including the generation of intrinsic curvature (Gaussian curvature $K = \kappa_1 \cdot \kappa_2$), extrinsic curvature (mean curvature $H = (\kappa_1 + \kappa_2)/2$), and even more complicated, ruffled structures and helicoidal structures were demonstrated. The control of different deformation was possible due to the inscribing of the spatial distribution of fiber alignments.

These design principles, however, are practically limited in the engineering of microscale systems (the importance of small system-size is discussed in 1.4) due to the resolution limits in the current manufacturing techniques. The low time-efficiency is also

one of the demerits of the fabrication method, imposed by the nature of additive-manufacturing (or bottom-up) process.

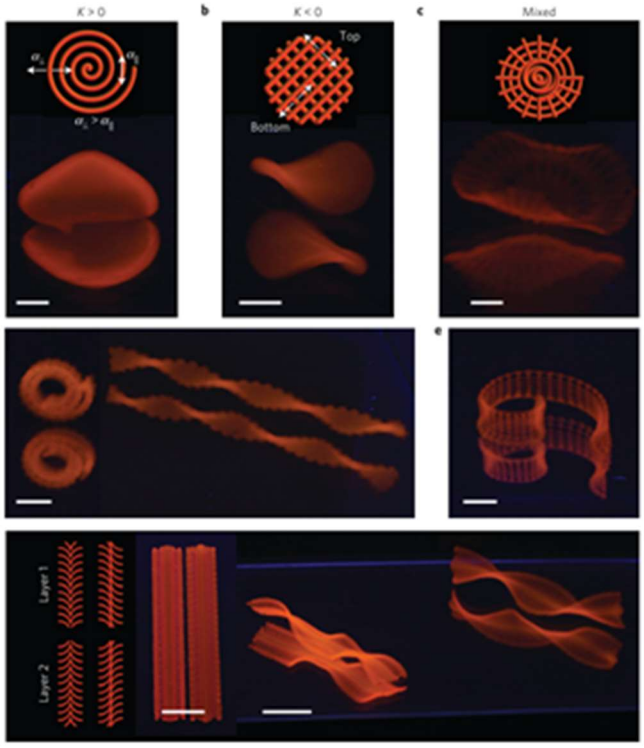

Figure 0.3 Swelling induced deformation of the 3D printed hydrogel. Reprinted with permission from ref [17].

1.3.2 **Inhomogeneous distributions of swelling strain**

Harnessing buckling instability, many fabrication techniques applicable to the formation of microscale gel actuators have been developed. Buckling instability (a transition from in-plane stretch to out-of-plane bending) occurs preferentially in thin objects because of the different scaling dependences of the elastic energy (U_{el}) of a deformed structure on the thickness ($U_{stretch} \sim h$, $U_{bending} \sim h^3$, where h is thickness) [18]. Typically, the buckling instability is introduced by imposing external confinements on

slender elastic objects [19]. Whereas, for the formation of free-standing gels, internal swelling strain mismatch is utilized for the generation buckling stresses [20].

Many scientists aim to develop effective fabrication methods to gain precise control over the internal swelling strain distribution of hydrogels, including Sharon and co-workers who utilized flow cells to generate an azimuthal gradient in the polymer composition [21]. Recently, a more effective method was demonstrated by the Hayward group. They utilized photo-patterning for the inscribing of the in-plane crosslinking density "patterns" on solid-state-curable polymers with high spatial resolution. Through the approach, programming of various non-Euclidean metric (Figure 1.4) was enabled in a single-step including buckling [22, 23] and even creasing [24].

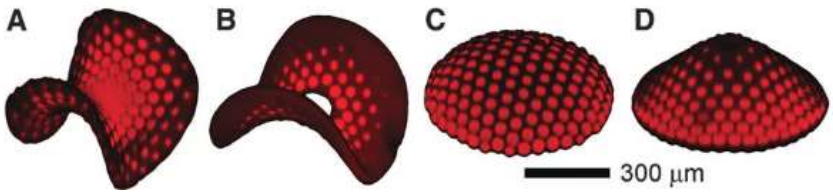

Figure 0.4 Swelling-induced deformation of photo-patterned 'metric' gels. Reprinted with permission from ref [22].

1.4 Thermodynamics of swelling of crosslinked polymer networks

In the fabrication method mentioned above, the programmed deformation of a gel was introduced by altering equilibrium swelling ratio (defined as the mass of the absorbed solvent divided by the mass of dried polymer) of a gel locally by applying chemical modifications (i.e., crosslinking density, material composition change). To understand the role of the chemical modification or the addition of rigid fillers on the equilibrium swelling ratio, understanding of the thermodynamics is required.

Flory and Rehner [25] first presented theoretical interpretations of the phenomena through the studies on the solvent absorption phenomena of vulcanized rubber. They developed a model that describes isotropic volume expansion of crosslinked polymer networks under the assumption that the free energy of swelling is determined by the combination of the elastic energy (F_{el}) and the mixing energy (F_{mix}) contribution. The elastic free energy was approximated to the entropic effect of the conformational change of the network. The contribution of the energy of mixing was assumed to be determined by the enthalpic and entropic contributions. The relations were rewritten by Hu and coworkers as [26]:

$$F_{el} = \frac{\mathrm{N k_B T}}{2} \cdot [\lambda_1^2+\lambda_2^2+\lambda_3^2-3-2\,ln(\lambda_1\lambda_2\lambda_3)] \quad (1.1)$$

$$F_{mix} = -\mathrm{k_B T} \cdot [\mathrm{C}\ln(1+\frac{1}{\Omega \mathrm{C}}) + \frac{\chi}{1+\Omega \mathrm{C}}] \quad (1.2)$$

Where N is the effective number of polymer chains in the gel per unit volume of the dry polymer, λi is the stretch in the principal direction, Ω is the volume of solvent molecule, C is the concentration of solvent, $\mathrm{k_B}$ is the Boltzmann constant, and χ is the dimensionless parameter known as the Flory-Huggins interaction parameter accounts the enthalpic contribution of mixing.

This relation can be further developed to relate experimentally achievable materials properties (λ_0 (isotropic equilibrium swelling strain), G (shear modulus), ν (Poisson's ratio)) with a structural parameter (N) and a thermodynamic parameter (χ) in the assumption of infinitesimal changes near the vicinity of equilibrium swelling state (linear theory).

$$\frac{Nk_BT}{\lambda_0} = G \tag{1.3}$$

$$\frac{\lambda_0}{N\Omega}\left(\frac{1}{\lambda_0^3 - 1} - \log\frac{\lambda_0^3}{\lambda_0^3 - 1} - \frac{\chi}{\lambda_0^6}\right) = \frac{2\nu}{1 - 2\nu} \tag{1.4}$$

$$\mathrm{N}\Omega\left(\frac{1}{\lambda_0} - \frac{1}{\lambda_0^3}\right) - \left(log\frac{\lambda_0^3}{\lambda_0^3 - 1} - \frac{1}{\lambda_0^3} - \frac{\chi}{\lambda_0^6}\right) = 0 \tag{1.5}$$

With this approach, not only information on the equilibrium states but also the dynamics of the swelling process are predictable. Under the assumption of incompressibility of polymer chains and solvent molecules, the concentration of solvent can be related to the stretching of the network ($\Omega C = \lambda_1\lambda_2\lambda_3 - 1 = \lambda_0^3 - 1$). Adopting a diffusion model (Darcy's law), the flux of solvent is then related to the migration of solvent driven by the chemical potential gradient. Finally, the concentration change is obtained as linear diffusion equations (Eq. 1.6 – 1.8) regarding a solvent concentration and an effective poroelastic diffusion coefficient, where M_0 is mobility, k is the permeability of the polymer network, and η is the viscosity of the solvent.

$$\frac{\partial \mathrm{C}}{\partial \mathrm{t}} = D^* \frac{\partial^2 C}{\partial x_i \partial x_j} \tag{1.6}$$

$$D^* = \frac{2(1 - \nu)\Omega^2 G M_o}{1 - 2\nu} \tag{1.7}$$

$$M_0 = \frac{k}{\eta\Omega^2} \tag{1.8}$$

The theory of linear poroelasticity, originally developed by Biot [27], has been widely utilized to delineate the mechanical and transport properties of polymer gels in

combination with experimental results [26, 28, 29]. However, the linear theory is limited to small deformation near the equilibrium state [30]. To overcome the limitation, Hong and co-workers developed a finite element model (FEM) on the basis of non-linear theory by Gibbs [31], by mapping the reference frame X_i to the current frame x_i [32, 33].

1.5 Overcoming of slow dynamics of hydrogel-based actuators

In both theoretical approaches, the dynamics of a swelling gel was assumed to follow diffusion equations. Therefore, the characteristic time for the swelling-induced deformation scales inversely with the poroelastic diffusion coefficient (D) of solvent in the network, and quadratically with the diffusion length (d ~ 1/2 of the thickness (h)) of the network. The characteristic time is referred to as the poroelastic time ($\tau_p = (h/2)^2/D$) [34]. This trend also corresponds to the scaling found in plants and fungal systems [35]. Using the poroelastic diffusion coefficient of water ($D = 1.5 \times 10^{-11}$ m^2 s^{-1}) obtained by Yoon and coworkers [28], the time required for the swelling of a millimeter-thick hydrogel is expected to be in the range of hours or days. Unless slow actuation speed is required, improvement in the actuation speed is necessary for wider practical usage.

Two representative strategies for improving the energy release rate are introduced in Figure 1.5. The first strategy is a thermo-responsive bi-stable buckled shell [36]. In this case, the speed of buckling transition between the convex and concave structure is not governed by diffusion kinetics but by the speed of sound in the material ($r \sim (E/\rho)^{1/2}$, where E is the elastic modulus and ρ is the density of the material). Reduction of the diffusion length can be another way of improving the power performance of a system. For example, Jiang and coworkers could induce superfast (< 1s) coiling of hydrogel sheet

(thickness~ 150 μm) by depositing electrospun fibers on to a non-swelling polyurethane fibrous sheet [37]. In the study, the reduced diffusion length (dried fiber diameter ~ 1.6 μm) was associated with the reason for the fast actuation.

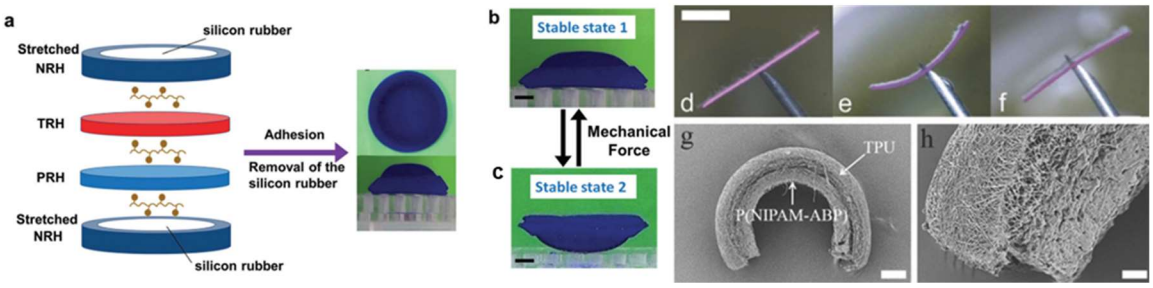

Figure 0.5 Strategies for driving fast motion of hydrogel-based actuator. (a~c) The fabrication method for stimuli-responsive snapping shell. Reprinted with permission from ref [38]. (d~h) The electrospun composite film made of thermoplastic polyurethane (TPU) and PNIPAm for high-speed actuation. Reprinted with permission from ref [37].

The ability to form complex geometries can be useful for improving actuation speed via a displacement amplifying mechanism. For example, Haines and coworkers developed an actuator that generates reversible and high system strain change (max ~ 34%) from an anisotropic strain change of mechanically elongated polymer chains (nylon 6.6 ~ 4% or polyethylene ~ 0.3%) [39, 40] across the glass transition temperature. By coiling fibers in a helical conformation and bundling them together, a great enhancement in the speed and displacement change was achieved (Figure 1.6a). Another example is found in nature. An aquatic unicellular organism, Vorticella, undergo high speed contraction (< 3 ms) at high system strain change (> 1000%) by harnessing helical contraction [41]. While a motor for the motion, called spasmoneme, can contract only about 40% of its original length [42], the helical conformation of the spansmoneme in the stalk amplifies the displacement change.

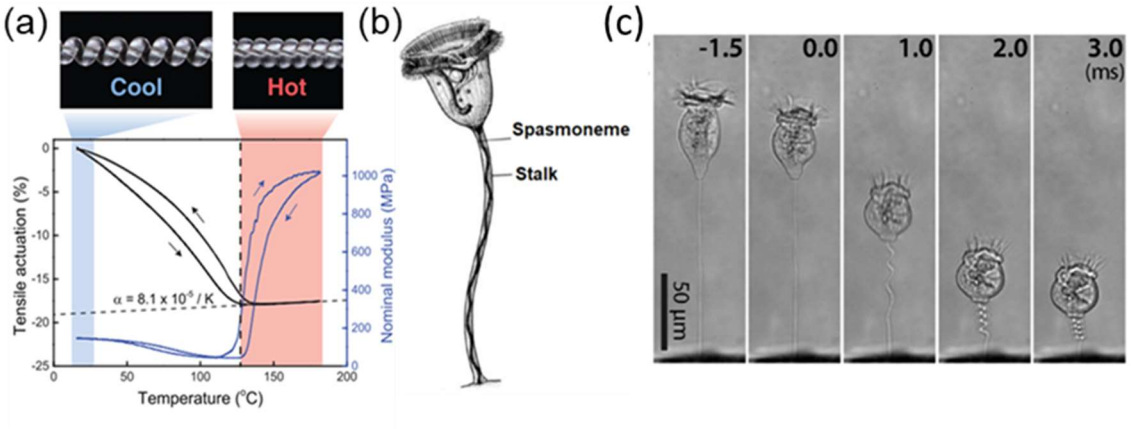

Figure 0.6 Actuation by helical contraction. (a) Tensile actuation of coiled nylon fibers by thermal relaxation mechanism. Reprinted with permission from ref [40]. (b) Schematics of *Vorticella* and its helical contraction in water [43] (c) Sequential images of stalk contraction of V. convallaria. Reprinted with permission from ref [44].

CHAPTER 2

4D TRANSFORMATION INDUCED BY TRANSIENT SWELLING OF ASYMMETRIC POLYMER GELS

2.1 Conceptual insights

In this chapter, we answer the fundamental question of how geometries and materials properties are related quantitively to the dynamic shape transformations of asymmetric gels under transient swelling/deswelling process.

2.2 Project summary

Novel design principles for polymeric gel devices that undergo time-dependent three-dimensional shape change (4D transformation) in a short period of time (max deformation occurs at 1/10 of the time for equilibrium swelling), but still at large curvature change ($\kappa h \sim 0.2$, where κ is curvature, h is thickness) constructed by straightforward fabrication methods (molding or cutting) are presented. The deformation does not require any specific swelling conditions or hierarchical assembly of heterogeneous components, which limit the minimum accessible size-scale or cause incompatibility issues (i.e. delamination). Instead, we take advantages of the asymmetric distribution of surfaces across the neutral bending axis of a homogeneous object to break symmetry in the dynamics of swelling. We precisely describe the dynamic swelling-induced transient deformation of asymmetric gels as a function of time, initial geometries, and materials' poroelastic properties. Finally, we discuss novel aspects of the transient deformation mechanism regarding the dynamic nature of deformation that affected by surface and bulk diffusion kinetics.

2.3 Introduction

In general, polymeric gel actuators are designed to generate bending deformation in order to convert slow and small swelling strain to a large and fast response of the actuator. Holmes and coworkers first demonstrated global bending of homogeneous polydimethylsiloxane (PDMS) gels by applying a non-homogeneous swelling condition of bringing solvents into contact with a specific region of an object [34]. The mechanism could induce much faster bending and buckling transition than the equilibrium swelling-based deformation mechanism arising from the generation of non-homogeneous strain distribution in homogeneous gel under a specific boundary condition.

Besides the swelling induced deformation, the Crosby group reported global bending of a homogeneous object in the presence of uniform solid-liquid interfacial tension [45–47]. Due to their small size scale (nanometers thick, micrometers wide, and arbitrary length), initially flat ribbons with asymmetric triagonal cross-sectional geometry were transformed into helices after being introduced to the water. The mechanism of transformation was explained by the unbalanced interfacial tension developed at the asymmetric surface areas across its neutral bending axis (a line connecting the center of mass of cross-sections) [45, 48]. Bending curvature (κ) of the transformed helix was determined by the properties of the materials (tensile modulus (E) and interfacial tension(γ) and the geometrical parameters (height (h) and width (w)) as:

$$\frac{1}{R} = \frac{\gamma \frac{1}{3} hw \left(\sqrt{\frac{1}{4} + \frac{h^2}{w^2}} - 1 \right)}{E \frac{wh^3}{36}} = 12 \frac{\gamma}{Eh^2} \left(\sqrt{\frac{1}{4} + \frac{h^2}{w^2}} - 1 \right) \tag{2.1}$$

The above two mechanisms are advantageous in terms of the simplicity of the fabrication process and robustness related to incompatibility issues between heterogeneous components (i.e., delamination). However, each mechanism still has limitations on its applicability. One main reason for the limited applicability of the interfacial tension-driven mechanism is its small driving force ($\gamma < 70$ mN m^{-1}) that defines either the size of a system or modulus of the material [34]. On the other hand, the main drawback of the transient swelling-induced deformation model by Holmes et al. is the necessity of specific swelling conditions which limit the development of a stand-alone system that would not require additional controlling units (i.e., partial solvent injection unit).

In the present work, we built upon the above ideas and proposed a new 4D transformation mechanism that can drive fast and large-scale transient bending of a homogeneous polymeric gel without requiring specific swelling conditions or hierarchical assembly. The transient deformation was precisely described as a function of time, initial geometries, and poroelastic properties. Finally, we introduced novel aspects of the transient deformation mechanism regarding the important role of surface and bulk diffusion dynamics.

2.4 Background

2.4.1 Generation of dynamic deformation under non-homogeneous swelling conditions

Apart from the widely-adopted design principles discussed in chapter 1, which harness the equilibrium shape of gels under a prescribed state of stress, a new type of

deformation mechanism has been developed based on the dynamic shape change of gel under continuously evolving states of stresses during transient swelling.

Transient swelling induced dynamic deformation is a ubiquitous phenomenon found in everyday life. For example, Douezan and coworkers studied curling of tracing paper placed on water surface [49]. The paper coiled up due to the asymmetric volume expansion of two surfaces. The asymmetric swelling temporally induced shear stresses causing out-of-plane bending but eventually relaxed after full wetting.

A similar approach was adopted by Holmes and coworkers to introduce large and fast deformations in slender polymer gels [34]. By placing a droplet of solvent (hexane or toluene) on one side of slender objects (a beam or disk made of polydimethylsiloxane (PDMS)), they could generate various transient deformations (bending, buckling, or twisting). In the case of bending deformation shown in Figure 2.1, bending curvature (κ_1) was generated by the introduction of solvent at one surface ($x_3 = h/2$). They related the bending curvature with a moment formed by swelling strain along the x_1 axis as Eq. 2.2. For a simple derivation, dominant diffusion of solvent through the transverse direction of the beam (x_3) was assumed.

$$\kappa_1 = \frac{12}{h^3}\int_{-h/2}^{h/2} \varepsilon_1(x_3) x_3 dx_3 \tag{2.2}$$

To describe the dynamics of strain (ε_1) through the transverse direction, a thermal diffusion equation ($D\frac{\partial^2 \mathrm{T}}{\partial x_3^2} = \frac{\partial T}{\partial x_3}$) and a thermal strain change ($\varepsilon_1 = \alpha\Delta T$, where α is a thermal expansion coefficient) was adapted based on an analogy between the heat transfer and mass diffusion. Through the approach, qualitative descriptions on the time-

dependent deformation became available; though the model predicts much faster kinetics (t_{max} = 0.1 τ_p, t_{eq} ~ 2 τ_p) than the observation (t_{max} = 1~2 τ_p, t_{eq} ~ 20 τ_p).

The deformation mechanism could induce faster dynamics than the time required for reaching an equilibrium state. It is, however, hard to be applied to remote systems due to the requirement of specific swelling conditions.

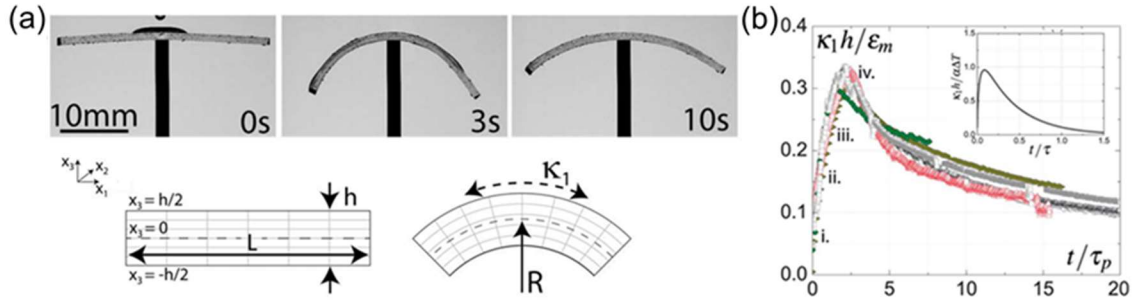

Figure 0.7 Inhomogeneous swelling-induced transient deformation of a gel. (a) Bending of PDMS beam by introduction of solvent droplet on the top surface (inhomogeneous swelling), (b) Normalized curvature ($\kappa h/\varepsilon$, h = thickness, ε = swelling ratio) vs. normalized time (t/τ_P). Reprinted with permission from ref [34].

2.4.2 **Numerical modeling of a swelling gel**

The transient-deformation mechanism mentioned above, infers that a global curvature would be generated by breaking symmetry in the dynamics of swelling. Instead of applying specific solvent conditions or altering materials composition, we imposed an asymmetric swelling condition by controlling the surface area distribution asymmetrically in a homogeneous object. This new approach will be beneficial for fabricating small-scale actuators due to the simple material compositions.

To maximize the applicability of the new deformation mechanism, a precise description of the dynamics and the shape-change was required. However, the prediction of the status of fluid distribution and the on-going deformations of swelling gels was not

a trivial problem. So far, several numerical frameworks [50–54] have been proposed to accomplish the task.

During swelling, a gel is not in thermodynamic equilibrium, so the chemical potential of the solvent in the gel is not homogeneous. The field of displacement of the network (x_i) is evolving as well. To depict the coevolution process, FEM has been used. However, due to the non-trivial challenges in relating the constitutive equations for thermodynamics and diffusion kinetics of chemical swelling, many proposed modeling techniques have been exclusively conducted on simple cases such as symmetric geometries (cubic gels, spheres) or highly restricted swelling conditions (1-dimensional transport of solvent) shown in Figure 2.2. Nonetheless, many efforts have ended up failing to capture the experimental observations.

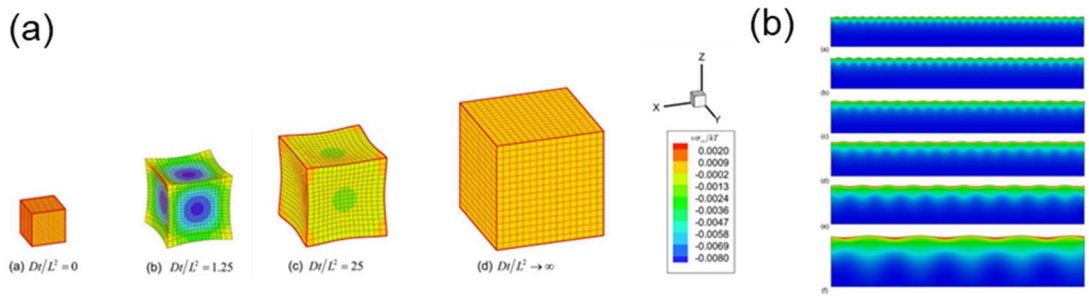

Figure 0.8 FEM of transient deformation of a swelling gel. (a) A free-swelling cubic gel, contours denote the stress state. Reprinted with permission from ref [54]. (b) Evolution of wrinkling pattern during one dimensional swelling of a gel. Reprinted with permission from ref [55].

One of the reasons for this discrepancy originated from the handling of instabilities generated at the early stage of swelling. Under the assumption of a chemical-potential-driven diffusion of solvent, the surface of gel reaches equilibrium swelling instantaneously [54]. This condition causes numerical instabilities in the modeling and

physically impossible as well. A unified way of handling the instability has not been developed yet.

2.4.3 **Non-Fickian diffusion in real matter**

The above approaches were developed on the assumption of Fickian diffusion, where the mass uptake by polymer gel is proportional to the square-root of time (n = 2 in Eq. 2.3). This condition is satisfied when the conformation changes of the polymer structure occur quickly compared to the diffusion of penetrants molecules.

$$\frac{M_t}{M_\infty} = kt^n \tag{2.3}$$

On the other hand, if molecules move into a polymer that relaxes slowly, a sharp diffusion front is formed and progresses proportional to time (n = 1 in the Eq. 2.3). The former case is called Fickian diffusion while the latter case is referred to as Case II diffusion, which often occurs in a polymer below its glass transition temperature (T_g) [56]. In most real cases, Case II diffusion phenomena are still observable at temperatures well above T_g, such as a PDMS swelling with dichloromethane (DCM) [56]. Therefore, a more generalized formulation is required to address the combined effects of diffusion and interface phenomena on mass transport.

In the case of heat transfer, Biot number (*Bi*) plays a key role in interpreting transient heat transfer. *Bi* is the ratio between conductive resistance within the body and the convective resistance outside the body. When *Bi* is very small (i.e., $Bi < 0.1$), conduction is much faster than the heat transfer by convection. The temperature change of the solid then becomes proportional to the elapsed time, termed Lumped parameter

model, which shows similar time-dependence as Case II diffusion. In general cases, the two heat transfer models are considered simultaneously to model heat transfer dynamics [57].

2.5 Experimental details

2.5.1 Materials

PDMS (Sylgard 184, Dow chemical) was selected for its low glass transition temperature (Tg ~ 150 K) and a wide selection of compatible solvents [58]. The mixing ratio of PDMS prepolymers was fixed at 1:10 (curing agent to base polymer ratio by weight) with a trace amount (0.14%) of titanium dioxide nanoparticles (< 100 nm, Sigma Aldrich) that served as a dye for the observation of the PDMS in the solvent.

2.5.2 Fabrication methods

The mixture was cured in an oven at 333 K for 48 hours in the shape of a sheet or a triangular prismatic beam. For the fabrication of the PDMS sheet, the prepolymer mixture was cured in between two glass plates and a spacer. Prismatic beams with isosceles triangular cross-sectional geometries (x_2-axisymmetric) at various aspect ratios ($AR = w / h$ = 0.66 to 9.2) and scales (d_{eff} = 0.29 to 3.6 mm) were prepared by curing the mixture in a 3D-printed (Uprint SE, Stratasys Inc.) mould made of acrylonitrile butadiene styrene (ABS). The mould was covered with a polyester film (McMaster-Carr) for the easy release of the PDMS beam and the formation of smooth surfaces (Figure 2.3).

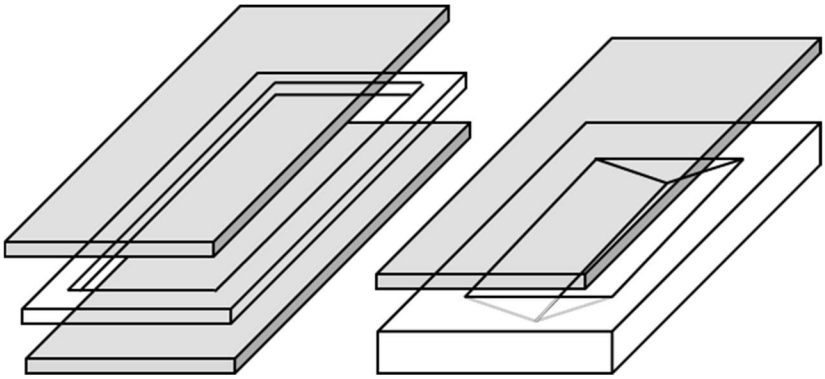

Figure 0.9 Schematics of mold design for fabricating a PDMS sheet (left) and a triangular prismatic beam (right)

2.5.3 **Characterization of poroelastic properties**

Equilibrium swelling strain ($\varepsilon_{eq} = (L_{eq} / L_0) - 1$, where L_{eq} is the length of a gel at its equilibrium swelling state and L_0 is the dried length) of PDMS was measured at room temperature by swelling a PDMS cube ($1 \times 1 \times 1$ cm^3) in a solvent bath for 48 hrs. Poroelastic properties of the PDMS and solvents were analyzed by the indentation method developed by Hu et al [26]. The poroelastic diffusion coefficient (D), shear modulus ($G \sim E/3$ for swollen PDMS gel), Poisson's ratio(ν), and the polymer-solvent interaction parameter(χ) were analyzed based on the time-dependent stress change of a swollen PDMS sheet ($h_0 \sim 2$ mm, $t_{swell} > 48$ hrs.) while it was compressed by a hemispherical glass probe ($R_{probe} = 5$ mm, Edmund optics) to prescribed depths ($h_{ind} = 60 \sim 270$ μm) on a glass substrate (Figure 2.4). The indentation force change was analyzed by measuring displacement change of a pre-characterized cantilever beam (cantilever compliance ~ 0.15 μm mN^{-1}, system compliance ~ 0.08 μm mN^{-1}) using a capacitive displacement sensor. The tensile modulus (E) of the PDMS sheet was measured by a universal testing machine (Instron TM 5564).

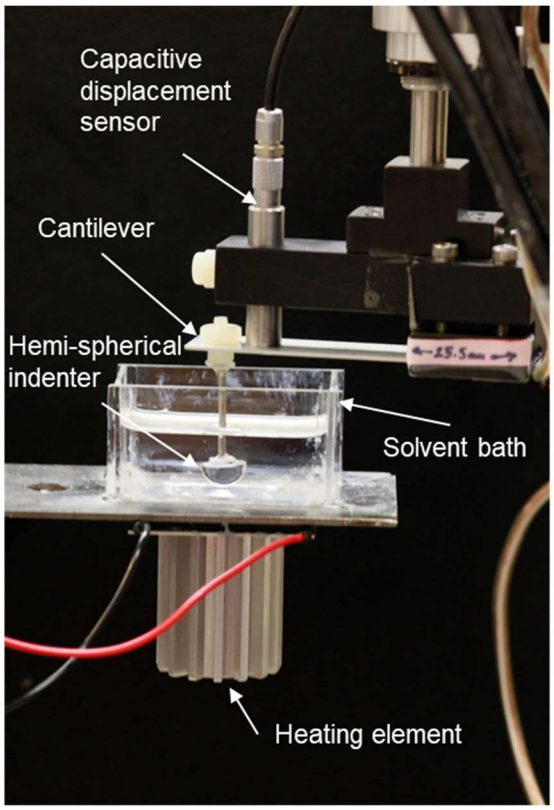

Figure 0.10 Image of indentation test setup for analyzing poroelastic properties of polymer gels

2.5.4 **Transient global bending of triangular prismatic PDMS beams**

The time-dependent deformation process of swelling PDMS gel was analyzed based on videos taken by a digital imaging camera (Canon t2i, focal length = 50mm, 30 fps). A beam cross-section geometry with 1-fold rotational symmetry was selected to aid straightforward analysis of the bending curvature by capturing two dimensional (parallel to x_2x_3 plane) images. Image analysis was performed with a custom Matlab code that fits a circle into the middle part (1/3 of the total length) of a deformed beam based on Pratt method [59]. To ensure homogeneous swelling, PDMS beams were immersed in a solvent bath for a short introduction time ($t_{intro} < 3$ sec).

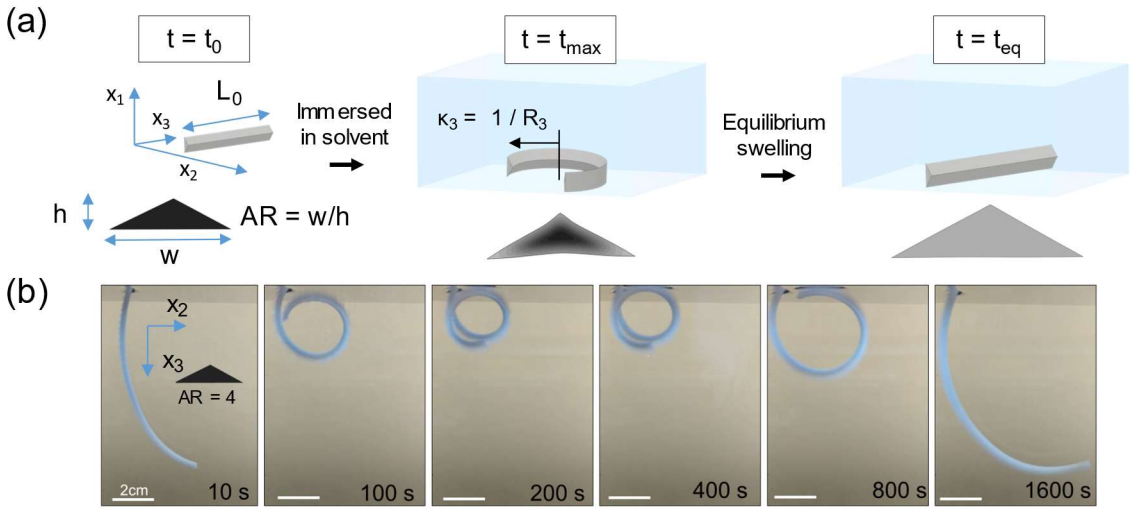

Figure 0.11 Swelling-induced transient deformation of a PDMS triagonal beam. (a) Schematics of dynamic bending curvature change during the free swelling process of a triangular prismatic PDMS beam and the corresponding cross-sectional geometry change during the procedures. (b) Time-lapse images of the swelling process of a vertically hanging isosceles triangular prismatic PDMS beam ($w \approx 9$ mm, $h \approx 4.2$ mm $L \approx 120$ mm) in the bath of n-hexane. The curvature (κ_3) reached the maximum value about 200 seconds (t_{max}) after the introduction. Meanwhile, the strip, guided by gravity without chiral preferences, transformed into a helix to avoid self-intersection. The gravitational force arises from the density difference between the PDMS beam ($\rho \sim 0.98$ g/cm^3) and the solvent (n-hexane, $\rho \sim 0.66$ g/cm^3). As the swelling continues, the curvature relaxes close to its initial value ($\kappa_3 \approx 0$).

The diffusion length of the beam was set to be larger than 0.3 mm so that tintro is sufficiently shorter than its characteristic diffusion time ($\tau_p > 20$ s >> t_{intro}, where τ_p is the defined as D / d_{eff}^2). To minimize the effect of gravity on the curvature change, triangular prismatic beams were immersed in the solvent bath with one end pinned to a weight in order to align the longitudinal direction of a beam perpendicular to the gravity (Figure 2.5a). The demonstrative experiment shown in Figure 2.5b was conducted with one end hanging vertically.

2.5.5 **Effect of surface diffusion dynamics on the transient bending**

The effect of surface diffusion dynamics on the extent of transient bending curvature was evaluated by comparing the deformation of a triangular prismatic PDMS beam (AR = 8.5, d_{eff} = 0.136 mm) in different solvent conditions. One test condition was immersing the triangular prismatic beam in the pure solvent (n-hexane, 99.9%) in the same manner as the above experiments. The other condition involved immersing the beam initially in a bath of non-solvent (ethanol, V_0 = 25 ml, > 99% Sigma Aldrich) and solvent-exchanged with n-hexane at a prescribed flow rate (0.035 ml min^{-1}) by a peristaltic pump (Ismatec ISM936D). The concentration change of n-hexane is calculated as $C(t)= 1 - e^{-\alpha t}$, where α = 714 sec.

2.6 Results and discussion

2.6.1 **Material properties**

The equilibrium swelling strain of PDMS in n-hexane was measured as 0.43 ± 0.02 and was isotropic for all directions ($\varepsilon_{eq} = \varepsilon_{11} = \varepsilon_{22} = \varepsilon_{33}$). In the case of toluene, the swelling strain was slightly lower (0.40 ± 0.02).

The modulus of cured PDMS was measured in different states (dried and swollen in n-hexane) at different deformation conditions (compression and tensile) (Figure 2.6). Compression test results showed that the effect of solvent swelling on the modulus of PDMS gel agrees with the Gaussian network model [60] where modulus of a gel changes proportional to the swelling ratio ($G_{swell} = G_{dry} \times \varphi^{1/3} = G_{dry} \times (1 + \varepsilon_{eq})^{-1}$, for isotropic expansion, where φ is polymer volume fraction). In the rest of analysis, the average modulus value of dried PDMS ($E_{\text{dry, PDMS}}$ = 1.4 MPa) measured by compression and

tensile tests was used. The Gaussian network model was accounted for estimating the modulus of swelling gels.

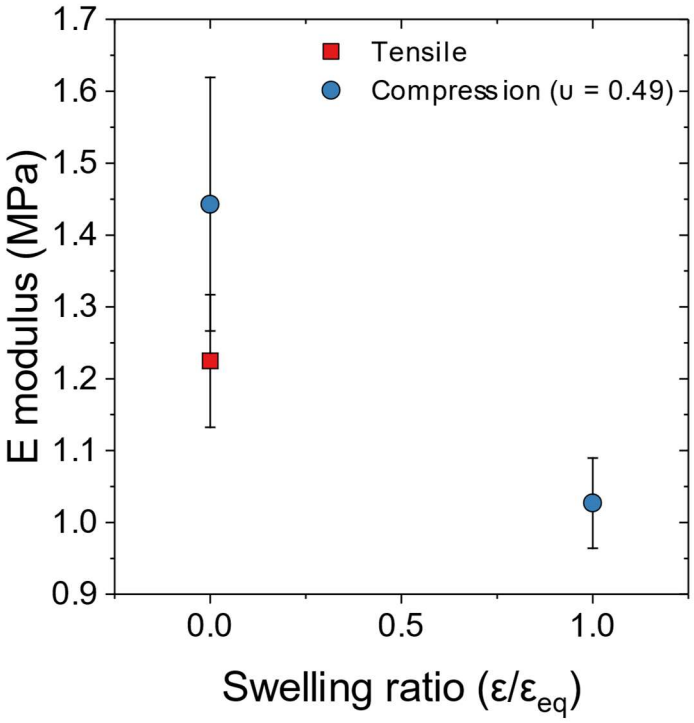

Figure 0.12 Elastic moduli of PDMS at different states and at different deformation modes

The polymer-solvent interaction parameter (χ) was calculated by the relation of Eqs. 1.3 - 1.5 and the literature value of the molecular volume of n-hexane (2.2×10^{-28} m^3). The value for PDMS-n-hexane system was 0.58 close to the theta solvent condition ($\chi = 0.5$ [61, 62]). This supports the approximation of Gaussian network model for the estimation of modulus during swelling of PDMS in n-hexane.

The poroelastic diffusion coefficient of each solvent was analyzed by fitting the stress relaxation curve to the numerical model proposed by Hu et al [63]. For a spherical indenter with radius R, the normalized time takes the form $\tau = Dt/a^2$, where $a = (Rh)^{1/2}$. The relaxation of normalized stress ($g(\tau) = (P(t)-P_f)/(P_i-P_f)$, where P_i is the stress

measured right after the gel was indented and P_f is the stress measured after relaxation) was modeled as:

$$g(\tau) = 0.491\ exp\left(-0.908\sqrt{\tau}\right) + 0.509\ exp\left(-1.679\sqrt{\tau}\right) \quad (2.4)$$

Using the relation, the poroelastic diffusion coefficient of n-hexane in PDMS was analyzed as $3.6 \times 10^{-9} \pm 3.5 \times 10^{-10}$ m^2 s^{-1} and the value for toluene was analyzed as $1.3 \times 10^{-9} \pm 5.0 \times 10^{-10}$ m^2 s^{-1} (Figure 2.7). The values are within the range of reported values of other solvents with similar molecular structures ($D_{heptane} \sim 2.3 \times 10^{-9}$ m^2 s^{-1} and $D_{Pentane} \sim 5.9 \times 10^{-9}$ m^2 s^{-1}) in the literature [26].

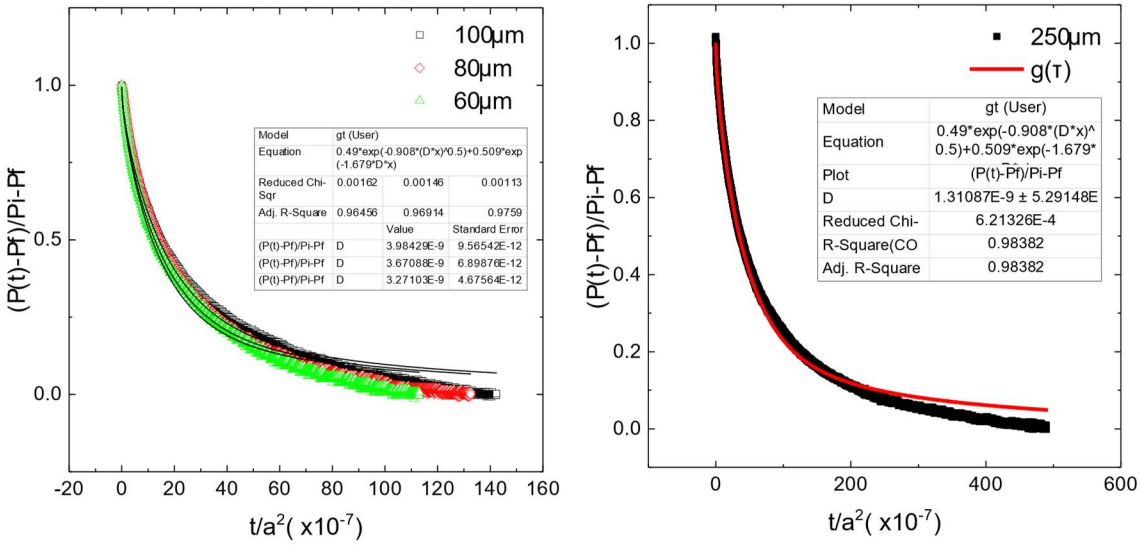

Figure 0.13 Analysis on the poroelastic diffusion coefficient poroelastic diffusion coefficient of n-hexane (left) and toluene (right) in the swollen PDMS gels

2.6.2 **Effect of cross-sectional geometries on the global bending of triangular prismatic PDMS beams**

When a polymer gel is introduced into the solvent, swelling strain starts to build up from the solid-liquid interfaces through the thickness (surface normal) direction of the free swelling object due to the limited diffusion speed of solvents. Consequently, swelling stresses are generated between the more swollen near-interface region and the less swollen inner region. These swelling stresses are not permanent but are dynamically changing until all volume elements reach the equilibrium swelling state [64]. Due to the surface-dominant and dynamic character of this phenomena, the consequences of transient swelling stresses were often observed in the form of surface and bulk instabilities, such as wrinkles [65], and buckling edges [66] that change their shape (i.e., wavenumber and wavelength) over time. However, utilization of the deformation mechanism to induce global bending in free-swelling objects was seldom performed [67].

We focused on the analogy between interfacial tension and the surface-mediated swelling stresses. Since both mechanisms are predominantly formed at the vicinity of the solid-liquid interfaces, it was expected that the transient swelling stress would induce global bending deformation similar to the interfacial tension-driven helical transformations of mesoscale ribbons. We took advantage of the large extent of swelling stresses [68] for the generation of large global bending curvature in macroscopic PDMS objects (h = 3 ~ 30 mm).

Four different ARs were selected (AR = 0.66, 1.15, 4, and 9.2) to confirm the validity of our hypothesis. In the case of the prismatic beam with an equilateral triangular cross-section (AR = 1.15, C_n = 3, where C_n is rotational symmetry), no significant curvature generation was observed as expected by Eq. 2.1, (gray hexagon in Figure 2.8). While, prismatic beams with isosceles triangular cross-sections (C_n = 1) underwent

transient bending along the x_2x_3-plane. However, the sign of bending was opposite to what was expected from the interfacial tension driven mechanism. The opposite sign of bending is physically plausible considering the tendency to increase surface areas as the surface region imbibes more solvent; by contrast, the positive interfacial tension acts to minimize the solid-solvent interfacial area.

Another difference observed from the swelling induced deformation was the 'transient' generation of bending. The maximum curvature was generated at about 1/20 ~ 1/10 of the time required for equilibrium swelling, then slowly bending back to zero curvature. The rapid dynamics of transient bending were similar to what was observed in the non-homogeneous swelling-induced bending of a polymer gel [34].

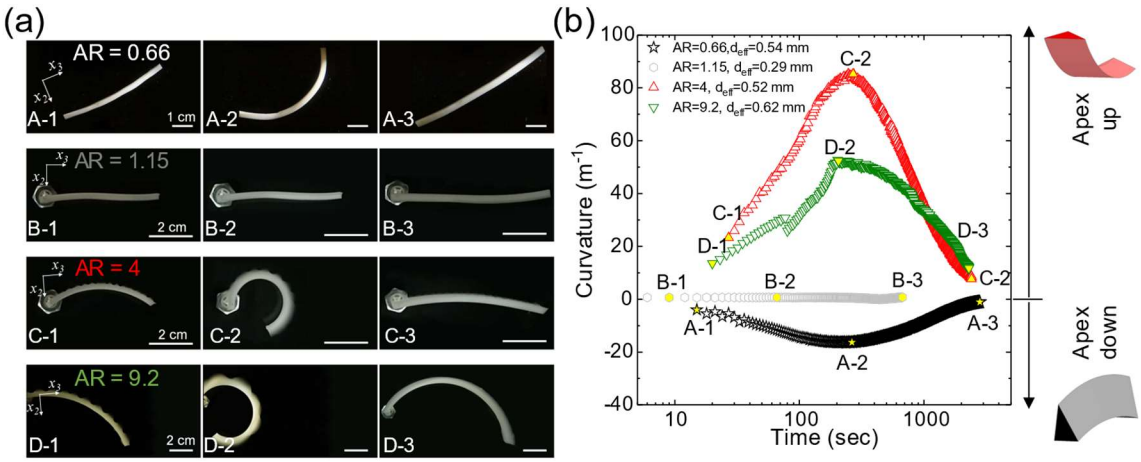

Figure 0.14 Effect of aspect ratio ($AR = w / h$) on the transient curvature generation. (a) Comparison of the deformed shapes of isosceles triangular prismatic beams with various aspect ratio cross-sections during transient swelling. (b) The bending curvature dependence on the swelling time for different geometries.

2.6.3 **Development of a simplified scaling model for the transient global bending**

The transient bending curvatures of samples shown in Figure 2.8 were replotted in terms of the normalized time and normalized curvature. The swelling time was divided by the poroelastic time (τ_P) where the measured poroelastic diffusion coefficient value of n-hexane ($D_{n\text{-}hexane}$) was used for calculating τ_p. The curvature of each sample with different AR and size was normalized by the experimentally measured maximum curvature of each sample (Figure 2.9). Except for the small differences in the dynamic curvature change during the initial stage of swelling, all the plots coincided with each other.

Figure 0.15 Plots of normalized variables. The curvature of each plot was normalized by the experimentally measured maximum curvature.

Based on the observed curvature change, we derived a simplified scaling relation between the geometries of triangular prismatic beams and the extent of bending curvature. The interfacial tension in the Eq. 2.1 was substituted with the surface swelling

compression: the amount of work per unit area done by the swelling near-surface region to elastically stretch confined by the unswollen inner region. The transversal portion of swelling strain ($\varepsilon_{33} = \varepsilon$ for isotropic swelling) and the resulting surface stress (γ_{33}) account for the bending of the axisymmetric beams along the x_2x_3-plane. We approximated that the triangular prismatic beam consists of three rectangular side walls (W = side length of the triangular cross-section and $h = d_{\text{eff}}$) and the maximum surface swelling compression at each wall is formed when the swelling front propagates across half of the diffusion length as Eq. 2.5 (Figure 2.10).

$$\varepsilon_{33}(x_2) = \begin{cases} 0, & \frac{-d_{eff}}{2} < x_2 < 0 \\ \varepsilon, & 0 < x_2 < \frac{d_{eff}}{2} \end{cases} \tag{2.5}$$

The maximum surface swelling compression applied to the wall was derived as:

$$\begin{aligned} \gamma_{33,max} &\approx \frac{E_s}{W d_{eff}} \int_{-\frac{w}{2}}^{\frac{w}{2}} \int_{0}^{\frac{d_{eff}}{2}} \varepsilon_{33}(x_2) \cdot x_n dx_n \; dx_w \\ &\approx \frac{E_s \varepsilon_{eq} d_{eff}}{8} \end{aligned} \tag{2.6}$$

where x_n is the surface normal vector, x_w is the vector for the lateral direction of the rectangular walls and E_s is the modulus of the swollen region. E_s can be approximated as E / ε since the χ value (~ 0.58, measured) is close to the theta solvent condition of the Gaussian network model [60]. The ε_{eq} was measured experimentally as 0.43 ± 0.02.

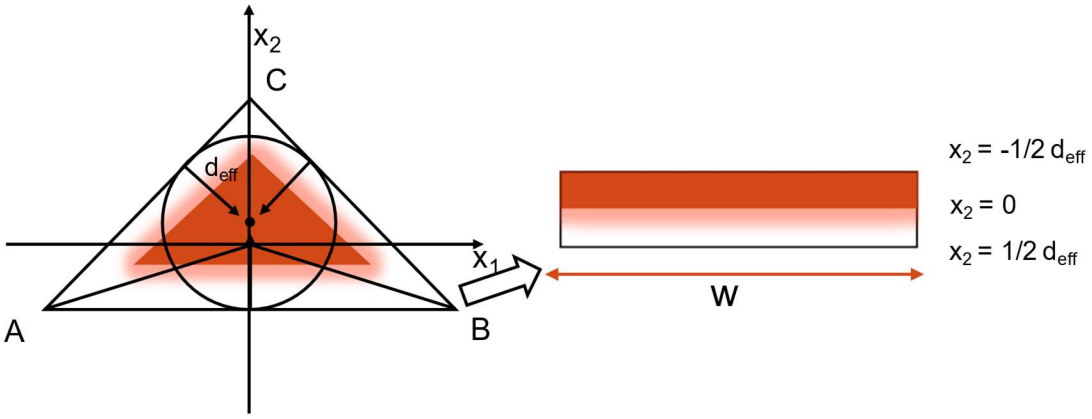

Figure 0.16 Schematics of the swelling state of a triangular prismatic beam at $t = t_{max}$

The d_{eff} can be written in the form of geometrical parameters as:

$$d_{eff} = \frac{w^2}{4h}\left(-\frac{1}{2} + \sqrt{\frac{1}{4} + \frac{h^2}{w^2}}\right) \tag{2.7}$$

The scaling predicts that the transient stress changes proportionally with the diffusion length, which scales with the size of a gel. This implies that the deformation mechanism can be applied to large scale objects, unlike the interfacial tension-driven deformation where the applicability is limited by the elastocapillary length (γ / E).

By combining Eq. 2.1 and 2.6, the theoretical maximum curvature is derived as Eq. 2.8. Notably, the sign of curvature is opposite to the Eq. 2.1 since the swelling compression tends to expand the surface area of a solid as opposed to the positive interfacial tension that reduces the surface area of a solid.

$$\kappa_{3,max,theory} \approx \frac{3\varepsilon_{eq} d_{eff}\left(1 - \sqrt{\frac{1}{4} + \frac{h^2}{w^2}}\right)}{2Eh^2} \tag{2.8}$$

In Fig. 2.11, the normalized value of curvature (κ_3 / $\kappa_{3,max,theory}$) was plotted as a function of normalized swelling time (t / τ_p). In addition to the four samples in Fig. 2.10,

a different-sized sample (d_{eff} ~ 3.6 mm, w ~ 20mm, h ~ 30 mm) was tested to check the validity of scaling.

The simplified scaling successfully predicted the direction of bending and the extent of curvature with good agreement with the experimental measurements. However, the scaling generally overestimated the experimental values and deviated more for the beams with more acute angles (i.e., AR = 9.2 or 0.66). We presumed that the discrepancy might be related to the oversimplification of complex diffusion phenomena and the negligence of the local buckling effect. Indeed, the effect of local buckling on the global bending curvature was observed in AR = 9.2 (Fig. 2.11b). Though the trend of the curvature was still increasing ($t < t_{max}$), a sudden drop in κ_3 was observed due to the merging of two buckling waves.

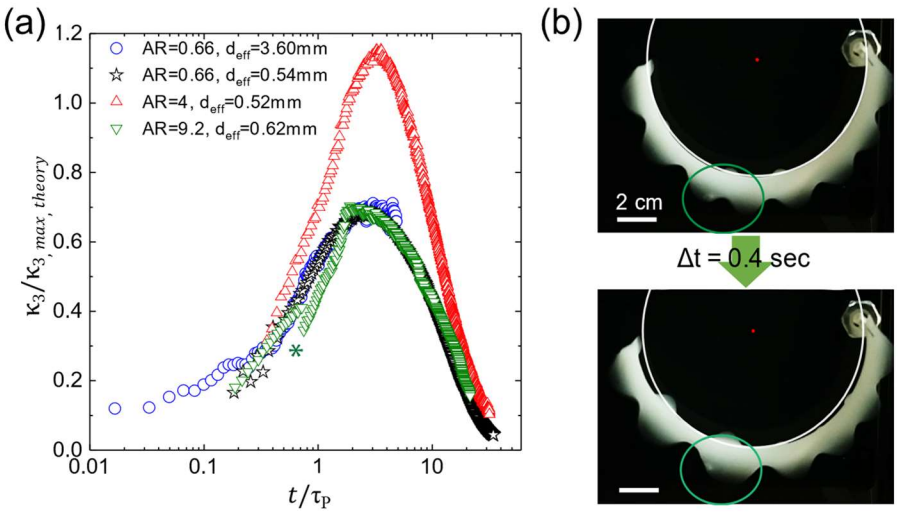

Figure 0.17 Plots of normalized variables and images showing the effect of local buckling wave on the global curvature. (a) A plot of normalized bending curvature versus normalized time for isosceles triangular prismatic beams with different aspect ratios and sizes. (b) Images of the bending beam (AR = 9.2) with local buckling edges at τ_p ~ 1 (green star in (a)). Merging of two local buckling waves (green circle) decreased the global bending curvature (white circles are drawn to guide the eye).

2.6.4 **Finite element model (FEM) for the analysis of the diffusion dynamics and the local buckling effect**

In order to maximize the applicability of the new deformation mechanism, a more precise description of the dynamics and the shape change is required. However, the prediction of the status of fluid distribution and the ongoing deformations of swelling gels is not a trivial problem. So far, several numerical frameworks [50–54] have been proposed to accomplish this task. During swelling, a gel is not in thermodynamic equilibrium so the chemical potential of the solvent in the gel is not homogeneous. The field of displacement of the network (x_i) is evolving as well. To depict the coevolution process, FEM has been used. However, due to the non-trivial challenges in relating the constitutive equations for thermodynamics and diffusion kinetics of chemical swelling, many proposed modeling techniques have been exclusively conducted on simple cases such as symmetric geometries [69] (i.e., cubic gels, spheres) or highly restricted swelling conditions [70] (i.e., 1-dimensional transport of solvent). Nonetheless, many efforts have ended up failing to capture the experimental observations.

One of the reasons for this discrepancy originated from the interpretation of instabilities generated at the early stage of swelling. Under the assumption of chemical potential-driven diffusion of solvent, the surface of the gel reaches the equilibrium swelling state instantaneously after being introduced into the solvent [54]. This condition causes numerical instabilities in the modeling, and is physically impossible as well. A systematic way of handling the swelling condition has not been thoroughly elaborated yet.

We developed a simple but robust numerical modeling method applicable to a variety of geometries and general swelling conditions by adopting a built-in

thermomechanical element (C3D6T) into the commercial FEM package with modifications to the material properties. Using an analogy between heat transfer and mass transfer phenomena, we implemented experimentally obtained poroelastic properties into the modeling parameters. In the case of poroelastic diffusion coefficient (D, $m^2\ s^{-1}$) converted to thermal conductivity (H) based on scaling relations shown in Eq. 2.9

$$D\ (\frac{\mathrm{m}^2}{\mathrm{s}}) \equiv \frac{thermal\ conductivity\ (\mathrm{J \cdot s^{-1} \cdot m^{-1} \cdot K^{-1}})}{specific\ heat\ (\mathrm{J \cdot kg^{-1} \cdot K^{-1}}) \times density\ (\mathrm{kg\ m^{-3}})} \tag{2.9}$$

Importantly, a mass transfer Biot number [57] ($Bi = k_c \times d_{\mathrm{eff}} / D$, where k_c is the convective mass transfer coefficient ($m\ s^{-1}$)) was introduced to model the dynamics of a real matter (PDMS) during transient swelling and deswelling process. In heat transfer problems, Biot number is used for evaluating the relative importance of convective heat transfer (medium to the surface of a body) to conduction in the solid body as Eq. 2.10.

$$Bi \equiv \frac{f(\mathrm{J \cdot s^{-1} \cdot m^{-2} \cdot K^{-1}})\ L_{conv}\ (m)}{H\ (\mathrm{J \cdot s^{-1} \cdot m^{-1} \cdot K^{-1}})} \tag{2.10}$$

Where L_{conv} is characteristic length defined as the volume of the body divided by the surface area of the body (= d_{eff}). We defined a mass transfer Biot number analogous to a heat transfer Biot number (Bi) to systematically account the mass transfer dynamics of solvent to the surface of a gel during swelling as well as the evaporative flux of solvent from the surface of a gel during deswelling.

In Figure 2.12, results of various Biot number were compared. When $Bi >> 1$, time scales to reach the maximum curvature and an equilibrium state approached the solution (Eq. 2.11 [34]) of ideal diffusion equation ($D\frac{\partial^2 c}{\partial x^2} = \frac{\partial c}{\partial t}$), where $\lambda_n = \frac{\pi(2n+1)}{2}$.

$$\frac{C}{\Delta C} = 1 - \sum_{n=0}^{\infty} \frac{2}{\lambda_n} sin\left[\lambda_n \left(\frac{1}{2} - \frac{x}{h}\right)\right] e^{-\lambda_n^2 t/\tau} \qquad (2.11)$$

We determined a Biot number of n-hexane in PDMS ($Bi_{\text{n-hexane}} \sim 0.3$) based on the deformation of a PDMS beam ($AR = 4$) and used for modeling of other geometries (Figure 2.12).

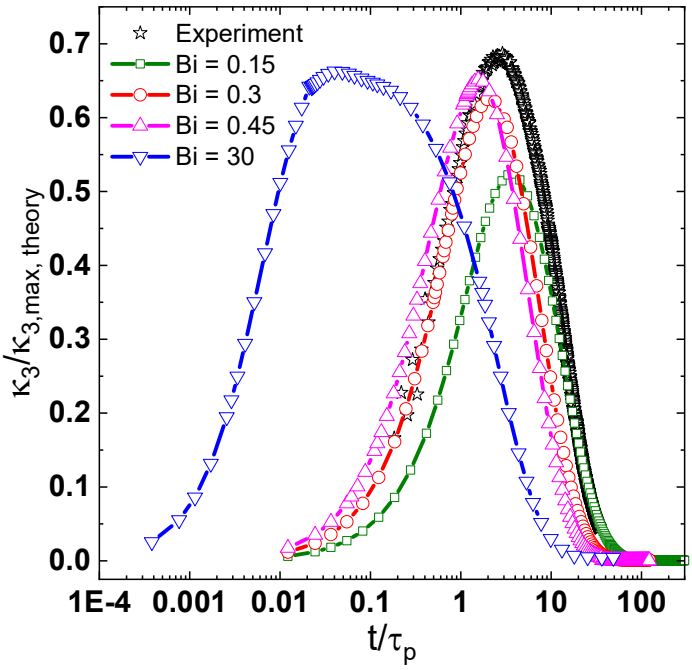

Figure 0.18 Determination of a mass transfer Biot number for PDMS-n-hexane system ($AR = 0.66$, $d_{eff} = 0.541$ mm)

A Biot number could be changed by altering the surface properties of a PDMS gel. For example, by treating the surface of the PDMS gel (Bi = 0.3) with oxygen plasma, the surface dynamics were slowed down (Bi = 0.22) due to the formation of less solvent-compatible surface layers (Figure 2.13).

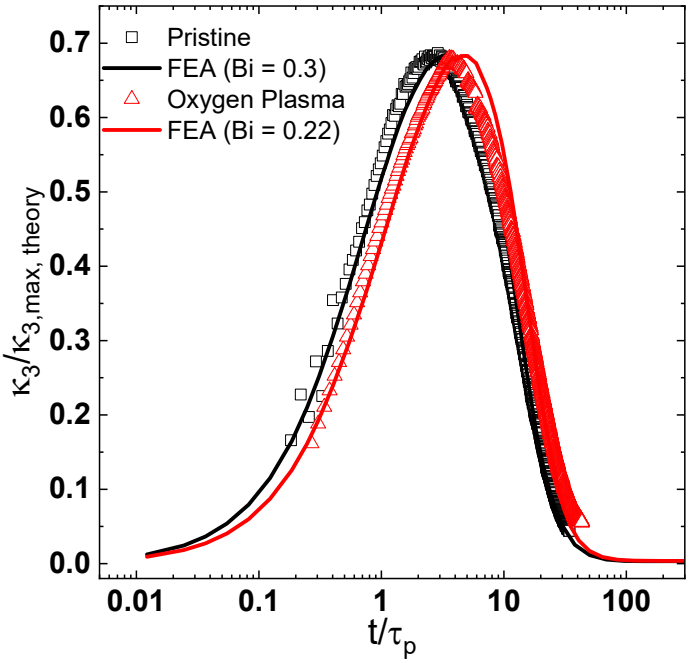

Figure 0.19 Effect of surface chemistry change on the surface diffusion dynamics and *Bi* of PDMS (*AR* = 0.66, d_{eff} = 0.541 mm) in n-hexane

In addition to the consideration on the surface diffusion dynamics, an additional non-ideal characteristic of solvent diffusion phenomena was considered: poroelastic diffusion coefficient dependence on the concentration of solvent in gels. For a polymer gel, the solvent poroelastic diffusion coefficient increases as the solvent fraction increases in the gel [71]. The change was explained by the free-volume increase of swollen polymer networks. We adapted a numerical model ($D = D_o\exp(\xi\cdot\varepsilon/\varepsilon_{eq})$, $\xi = 3$ for n-hexane) to account the effect. The results were compared to the results of a constant poroelastic diffusion coefficient or a linear relation in Figure 2.14.

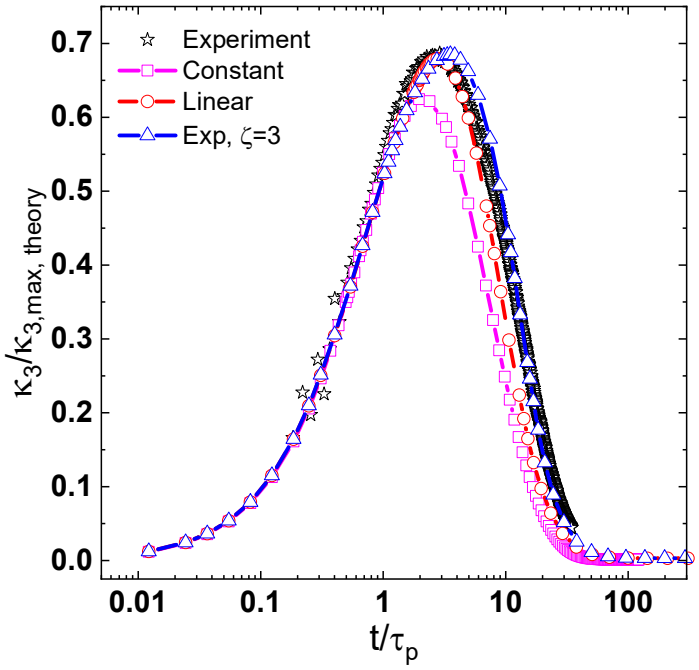

Figure 0.20 Effect of solvent-concentration-dependence of poroelastic diffusion coefficient on the prediction of transient deformation

The developed modeling method allowed us to simulate the dynamic coevolution process of internal stress and strain, and the resulting global deformation and local buckling instabilities with high precision (Figure 2.15). For example, the fast merging process of buckling waves shown in Figure 2.11b, was also simulated by FEM (a small kink in the graph of AR = 9.2). The model provided experimentally-inaccessible (or hardly accessible) information, such as the cross-sectional area change (~147% at $t = 3\tau_p$) and the swelling strain distribution inside of a gel (Figure 2.15b) or the stress distribution (Figure 2.15c). The information on the cross-sectional area change provided a basis for validation of the hypothesis made for the derivation of the simplified scaling relation. The

hypothesis suggests the propagation of swelling front is about half of the diffusion length at $t = t_{max}$, where the cross-sectional area change is expected to be $(1+0.5\varepsilon_{eq})^2$.

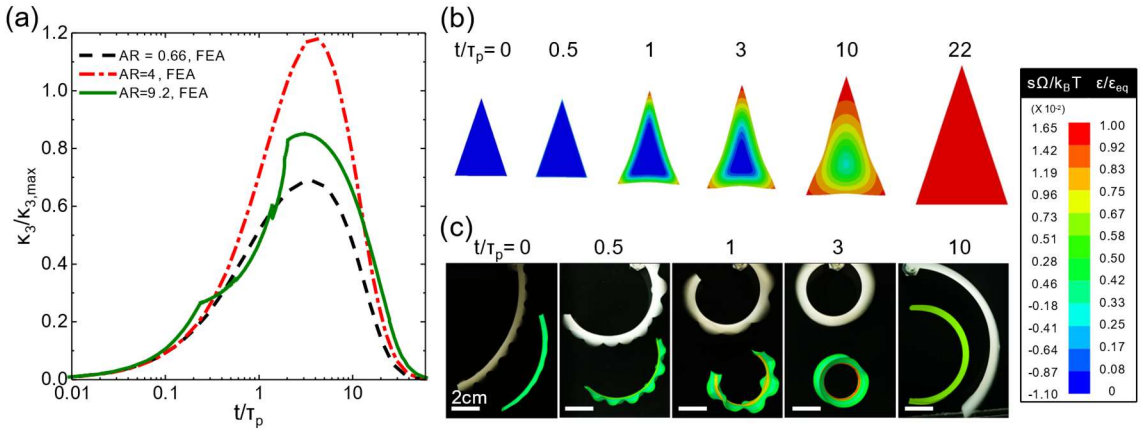

Figure 0.21 FEM of transient bending of isosceles triangular prismatic beams with different aspect ratios. (a) A plot of normalized bending curvature as a function of normalized time (b) Contour plots of normalized swelling strain inside of a modeled triangular prismatic beam (AR = 0.66) at different swelling times. (c) Contour plots of normalized stress of a modeled triangular prismatic beam (AR = 9.2) at different swelling times. Shapes of experimental results (white, scale bar = 2 cm) and FEM (green, not to scale) were compared at different times.

2.6.5 **Effect of surface diffusion dynamics on the transient bending deformation**

The extent of stress is affected by the surface and bulk diffusion dynamics since the stress for the transient bending is originated from the non-homogeneous swelling strain distribution between the near solid-solvent interface region and the inner region of polymer gel. If the rate of solvent diffusion at the interfaces is much slower than that in the bulk, then the inhomogeneity of swelling strain becomes negligible as well as the stress and resulting deformation.

An analogy between mass transfer and heat transfer is also found here. In the case of the transient heat transfer problem, when $Bi << 1$, the conduction of heat inside of a

solid is much faster than the convective heat transfer from the medium to solid surfaces. Thus the temperature of the solid can be approximated as uniform and gradually changing. This is the so-called lumped parameter model (LPM) [57]. The LPM is applicable to highly conductive materials or in the presence of very slow convective heat flow.

The effect of surface diffusion dynamics on the transient bending mechanism was evaluated by comparing the deformation of a triangular prismatic PDMS beam (AR = 8.5, d_{eff} = 0.136 mm) under different solvent conditions: pure solvent (Figure 2.16a) and solvent exchanged from non-solvent (Figure 2.16b). The triangular prismatic beam deformed less (κ_3 / $\kappa_{3,max}$ = 0.9 (99% n-hexane), 0.25 (gradual, α = 714 sec)), and the local buckling also diminished under the limited supply of solvent at the interface. This result demonstrated the importance of surface-bulk diffusion dynamics on the transient deformation phenomena as well as the importance of asymmetric geometries.

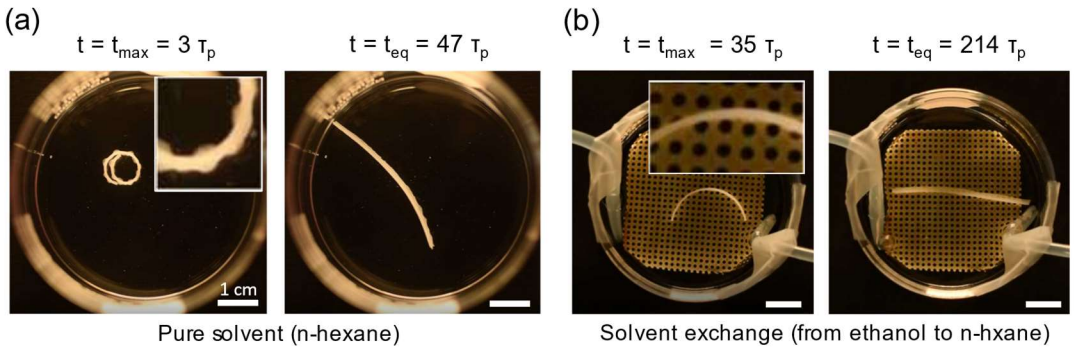

Figure 0.22 Transient deformation of a triangular prismatic PDMS beam (AR = 8.5, d_{eff} = 0.136 mm) under different solvent conditions. (a) image of the PDMS beam immersed in the bath of pure n-hexane. Images at $t = t_{max}$ and t_{eq} are shown. (Inset is a magnified image of the local buckling). (b) The same PDMS beam was immersed in a non-solvent (ethanol, V_0 = 25 ml) then solvent-exchanged with n-hexane by injecting n-hexane and ejecting the mixture at the same flow rate (Q = 0.35 ml min^{-1}). Images at $t = t_{max}$ and t_{eq} are shown. (inset: no buckling was observed)

2.7 Conclusions

In summary, we developed a novel 4D deformation mechanism based on the transient generation of the inhomogeneous swelling strain distribution in asymmetric gels. We depict the role of geometries, material properties, and diffusion dynamics on the transient evolution of bending curvature. An easily accessible modeling method was introduced as well, which will expand the applicability of the novel deformation mechanism for the development of polymer gel-based devices with novel functionalities.

CHAPTER 3

HIGH-RATE AND LARGE-DISPLACEMENT ACTUATION OF MESOSCALE HELICES

3.1 Conceptual insights

In this chapter, we answer the fundamental question of how two different surface-mediated phenomena, interfacial-tension-driven deformation and surface diffusion, be balanced with elasticity to control shape transformation of a small-scale or soft object.

3.2 Project summary

Here, we demonstrated Vorticella-like underwater actuation of mesoscale polymeric actuator that exhibited high-rate (~ 1300% s^{-1}) and large contractions (~ 1500%) in response to a change in temperature or pH, similar to the [Ca^{2+}] response in spasmoneme, which is an actuator muscle of Vorticella. We used a convective self-assembly process to form mesoscale ribbon-like precursor structures (mesoribbons), consisting of a phase-switchable polymer. The unique shape of mesoribbons, inherent to convective assembly structure, was utilized to induce a 3D helical transformation and to achieve coiling response. We harnessed the advantage of an analogy between two surface-mediated phenomena: interfacial tension and surface diffusion. The helical geometries (radius and axial extension) were quantified as a function of mesoribbon geometries and material properties (interfacial tension, modulus, swelling ratio) with respect to flow condition. The effect of each surface-mediated phenomena was

deconvoluted by analyzing the kinetic response of mesohelices at different stimuli changing rate. We found that the interfacial tension change of asymmetric object controls the equilibrium geometries and the surface diffusion

3.3 Introduction

The recognition of the advantages of life-like locomotion exhibited by fish [9], birds [72], or insects [73, 74] has increased the demand for artificial muscles that emulate the function of natural ones [75]. However, emulating these muscles at a life-size scale is significantly challenging due to a large number of hierarchical microstructures [76, 77].

For this reason, unicellular organisms like ciliate, flagellate, and amoeboids have been studied as model systems for locomotion in engineering [78] and biomimetics [79]. Among many species in unicellular eukaryotes, Vorticella convallaria (Vorticella) has been particularly interesting to scientists due to its unique method of motility. Surprisingly, Vorticella has one of the largest values for specific velocity (v_s = body length s^{-1}) among living creatures [41]. By evolving a helical contraction mechanism in its stalk that tethers its body (zooid) to a substrate in its environment, Vorticella can contract at a maximum rate of 1200 times its body length per second (~ 6 cm s^{-1}) at a contraction ratio of 500 % (= $\Delta H / H_1$, where H_1 is the axial length of a contracted helical stalk and ΔH is the axial length change)(Figure 1.6b and 6c) [79]. Such fast motility is not common for other aquatic microorganisms since the viscous drag of water dominates the inertia of movement at the microscale (Renolds number << 1) [80]. Under such conditions, this asymmetry of motion is critical for the motility of microswimmers [80, 81]. The helical transformation of the stalk not only allows Vorticella to move fast, but also acts as a geometric amplification for the previously reported small length change

(40% [42]) of the contractile spasmoneme in the stalk, to large-contraction of the stalk (500%).

Many researchers have focused on elucidating the mechanism for fast contraction in the spasmoneme [82, 83], as well as utilizing the spasmoneme as microscale actuators [79, 84]. However, Vorticella-like tethered helical coiling has not been explored despite the known advantages that the fast and large-displacement underwater motions give Vorticella over many artificial microswimmers [84, 85].

While, helical deformation of growing tissues of plant systems, such as climbing stems of bines and vines [10] have inspired many demonstrations of hydrogel-based devices that form helical shapes by uptaking water [16, 17, 86]. Swelling stress (osmotic pressure) of hydrogel was utilized to drive the transformation of the devices against the elastic restoration forces [32]. In general, the helical transformations were induced by breaking two plane symmetries (e.g. lateral plane and longitudinal plane) in the swelling strain distribution of hydrogel being constrained by non-swelling, rigid component in the structure [16, 17, 86]. However, the axial length changes occurring during the helical transformation are small (~ 200%) because the swelling strain is not amplified geometrically: helical transition, which reduces the axial length of a device, which occurred when a hydrogel component swelled. The design principle is also practically limited in the fabrication of vorticella-scale devices due to the resolution limits in the current manufacturing techniques (~ 20 μm [87]).

3.4 Background

3.4.1 Surface energy driven deformation of a solid

It is widely appreciated that surface tension dominates shaping of liquids at small scales: a droplet of water tends to form a sphere to minimize the surface area. On the other hand, it was only recently that surface tension became known to deform a solid. Mora and coworkers demonstrated a surface tension-induced deformation of a solid body by immersing a long cylindrical rod made of ultra-soft agar gel (μ: shear modulus ~ 200 Pa) into toluene. The gel shortened its length about 4.5% to minimize the surface area (Figure 3.1) [48]. In the Crosby group, Pham and coworkers also observed a surface tension-induced deformation of mesoscale ribbons (thickness: 15 ~ 200 nm) made of rigid solid (μ: 0.1 ~ 0.3 GPa) in water [45].

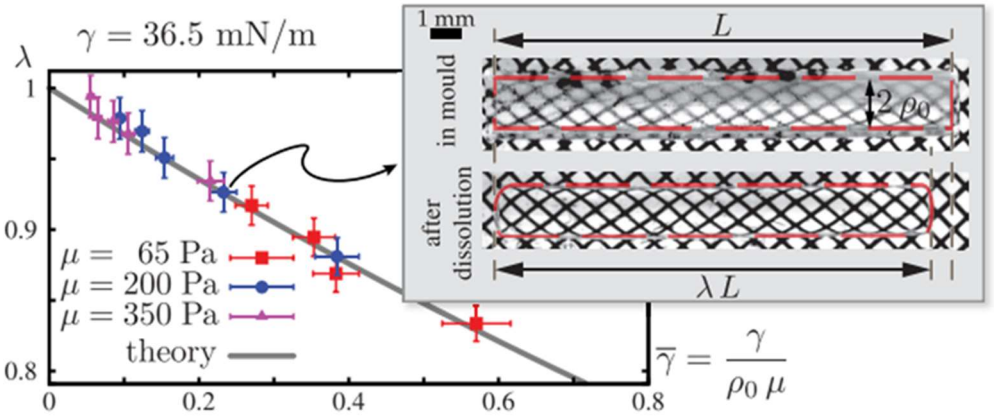

Figure 0.23 Shortening of cylinder made of agar gel when immersed in toluene. Reprinted from ref [48].

To generate a deformation in solid, surface tension must do work against elastic restoring forces. The effect of surface tension becomes prominent when the size of an object is comparable to the electrocapillary length ($l = \gamma / \mu$, γ is the surface tension). For an agar gel (γ ~ 40 mN m^{-1} [48]), the characteristic length is about 200 μm. In the case of

rigid solid, like polymethylmethacrylate (PMMA, $\gamma \sim 40$ mN m^{-1}, $\mu \sim 0.3$ GPa [45]), the characteristic length is as short as atomic length (~ 0.1 nm) thus virtually undetectable.

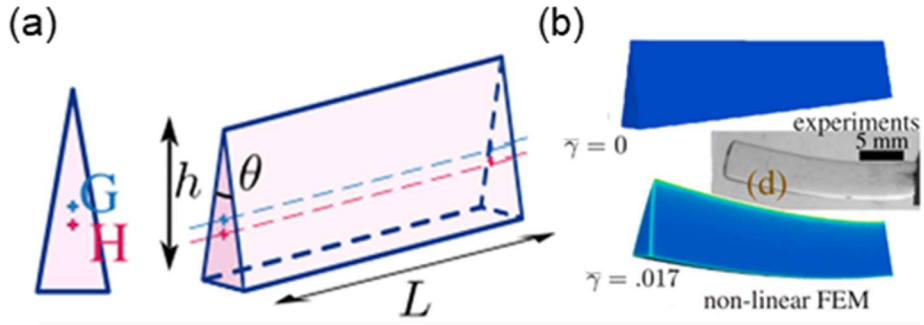

Figure 0.24 (a) Initial geometry of triangular gel, G: Spieker center, H: centroid, (b) Surface tension driven bending of PDMS (experiment and FEM results). Reprinted from ref [48].

Mora and coworkers also discovered that surface tension could cause global bending of the solid beam when the object is formed in the shape of a triangular beam with isosceles cross-sectional geometry. They observed the deformation with an agar gel submerged in PDMS (Figure 3.2). The bending curvature (κ, positive: bending up, negative: bending-down) was derived regarding the geometries and material properties as Eq 3.1[49].

$$\kappa = \frac{\bar{\gamma}}{h}\left(\frac{1}{\sin\frac{\theta}{2}} - 2\right) \tag{3.1}$$

Where, $\bar{\gamma} = \frac{\gamma}{\mu h}$, θ is the acute angle of the cross-section, h is the height of the cross-section.

The physical meaning of Eq. (11) can be explained by rewriting it with geometrical variables [45]. A line connecting the center of the area of cross-sections (***H*** and red line in Figure 12) determines the neutral bending axis that doesn't change length

while bending. If the neutral bending axis coincides with the line connecting the center of the perimeter (known as Spieker center, $\boldsymbol{G}$, the blue line in Figure 13), then the sum of surface area change around the bending axis is zero. Otherwise, the surface area change(ΔA) per unit ribbon length (L) is determined by the distance between $\boldsymbol{G}$ and $\boldsymbol{H}$:

$$\frac{\Delta A}{L} = -\kappa \boldsymbol{n} \cdot P(\boldsymbol{G} - \boldsymbol{H}) \tag{3.2}$$

Where **n** is normal to the neutral bending axis, P is the the perimeter length.

3.4.2 **Helical deformation of mesoscale ribbons**

In the Crosby group, we observed similar phenomena in the mesoscale ribbons (h: 15 ~ 200 nm, θ ~ 175°) made of polymers (PMMA) or nanoparticles (Cd-Se quantum dots, μ ~ 0.1 GPa) [45]. In the study, Meso-scale ribbons with asymmetric cross-sectional geometry were formed by flow coating [88] based on controlled pining-depinning of the liquid-substrate contact line and the deposition of solutes at the confined meniscus driven by evaporation flux [89]. The ribbons were deposited on a silicon wafer coated with water-dissolvable polymers (polyacrylic acid). When submerged in water, the ribbons were released from the substrate and deformed to helical shape with a specific bending curvature depending on the thickness, modulus, and interfacial tension of the ribbons (Figure 3.3). Pham and coworkers confirmed the role of interfacial tension on the helical deformation of ribbons by observing relaxation of bending curvature as a surfactant was dispersed in the water bath [45].

The observation not only validates the proposed mechanism but also infers a potential actuation mechanism that can induce reversible transformation between a helix

and a ribbon. We hypothesized that active changes in the interfacial tension between solid and liquid would result in a reversible helical transformation like as the motion of *Vorticella* discussed previously (chapter 1.3).

To realize the unprecedented actuation mechanism, we tested several materials known for undergoing active surface change, including thermal-responsive hydrogels, and pH responsive hydrogels.

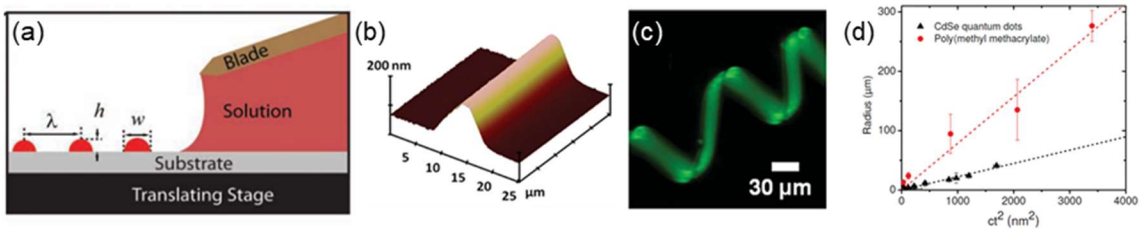

Figure 0.25 Helical transformation of mesoribbons (a) Schematics for flow coating of meso-ribbons on a substrate [88], (b) Surface thickness profile of flow-coated Cd-Se QDs (t ~ 200nm, w ~ 12µm) (c) Helical transition of mesoribbons released in water (d) Thickness-radius relation of mesoribbons made of PMMA (red) and CdSe QDs (black). Reprinted with permission from ref [45].

3.4.3 **Thermal-responsive hydrogels**

Temperature-dependent coil to globule transition [90, 91] of Poly(N-isopropylacrylamide) (PNIPAm) is the most comprehensively studied stimuli-responsive mechanism and a material system known for the ability to change interaction with water (hydrophilicity). Based on the responsiveness to temperature change, the thermo-responsiveness is classified into two groups: LCST (lower critical solution temperature) and UCST (upper critical solution temperature). A polymer exhibiting LCST solvates and becomes miscible at normal temperature, but the solubility decreases as the temperature

rise. Eventually, it precipitates beyond a critical temperature [92]. The opposite case is called UCST which dissolved above a certain temperature.

According to recent studies [93, 94], the solubility change of PNIPAm caused by the competition between the solvation of polymer by water molecules and the formation of intramolecular bonding between hydrophilic moieties (amine (N-H) and carbonyl (C=O)) in the polymer. In this explanation, the free energy of the system is affected by entropy decrease due to the loss of randomness of solvating water molecules and the enthalpy change due to the formation of intermolecular hydrogen bonding. The combined effect results the collapsing of polymers at above LCST (~ 303 K) where the entropy effect dominates (Figure 3.4).

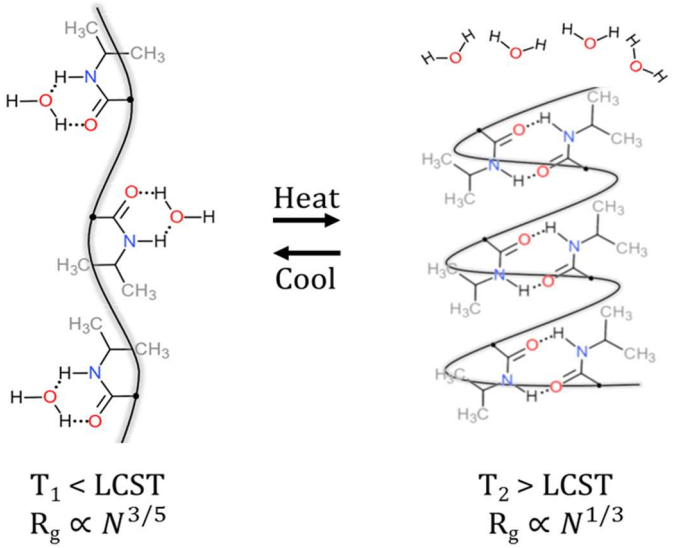

Figure 0.26 Schematic of Temperature responsive coil to globule transition of PNIPAm Crosslinked PNIPAm forms a hydrogel that can reversibly change the swelling ratio across the LCST.

Although there have been numerous studies on the mechanism [92–94], and lots of devices that have demonstrated practical applications of the hydrophilicity change [95, 96], there are still on-going debates on whether there is a change in the interfacial tension between hydrogels made of PNIPAm and water across the two phases. At above LCST, it is widely accepted that the intermolecular hydrogen bonding causes conformation change of PNIPAm that exposes more hydrophobic moieties (propyl groups) to surrounding water molecules. This change is expected to cause a change in the interfacial tension between the polymer and water. Many experimental results that support the reversible change of surface energy were published as temperature dependence of advancing contact angle [97] (measured by Sessile Drop method), oil-wettability [95], and protein-adhesion [96].

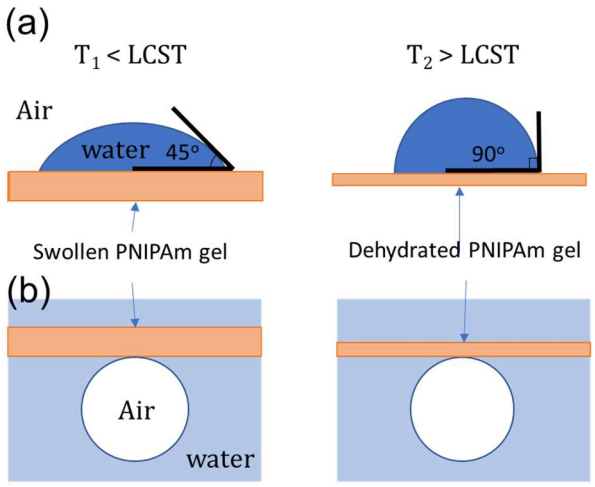

Figure 0.27 Contact angle measurement by (a) Sessile drop method, (b) Captive bubble method

However, a receding contact angle measured in the presence of surrounding water (captive bubble method, Figure 3.5) did not coincide with the prediction. Only negligible change in the contact angle (~ 90°, meaning complete wetting) across the LCST was

observed instead [98–100]. The authors explained that the discrepancy would be related to the rearrangement of surface molecular composition depending on the energy state of the opposing phase. The large mass fraction of water remained in the PNIPAm gel (~ 20% at T > LCST and ~ 85% at T < LCST [101]) also regarded as the reason of low contact angle of PNIPAm submerged in water at above LCST. We addressed the issue for the realization of interfacial tension change driven actuation.

3.4.4 **Chemical modification of PNIPAm-based hydrogels**

The sensitivity to the neighboring chemical environments has been harnessed for the development of multi-stimulus-responsive hydrogels based on PNIPAm. For example, copolymerization with acrylic acid (AAc) resulted in dual stimuli-responsiveness to the temperature or pH change [102]. Substitution of propyl group with spiropyran-containing moieties realized a light-sensitive reversible swelling-shrinkage behavior [103]. It was also reported that the substitution of acrylic acid to butyl acrylic acid could improve the dynamics of phase transition behavior [104].

3.5 Experimental details

A well-known phase-switchable material, poly(N-isoporpylacrylamide) (PNIPAm) was chosen as a model material for demonstrating a Vorticella inspired underwater actuation. We selected an evaporation induced convective self-assembly technique termed flow coating [45, 47, 88, 105, 106] to prepare millimeters long, nanometers-thick, ribbon-like structures (mesoribbons) with asymmetric cross-sections as depicted schematically in Figure 3.6.

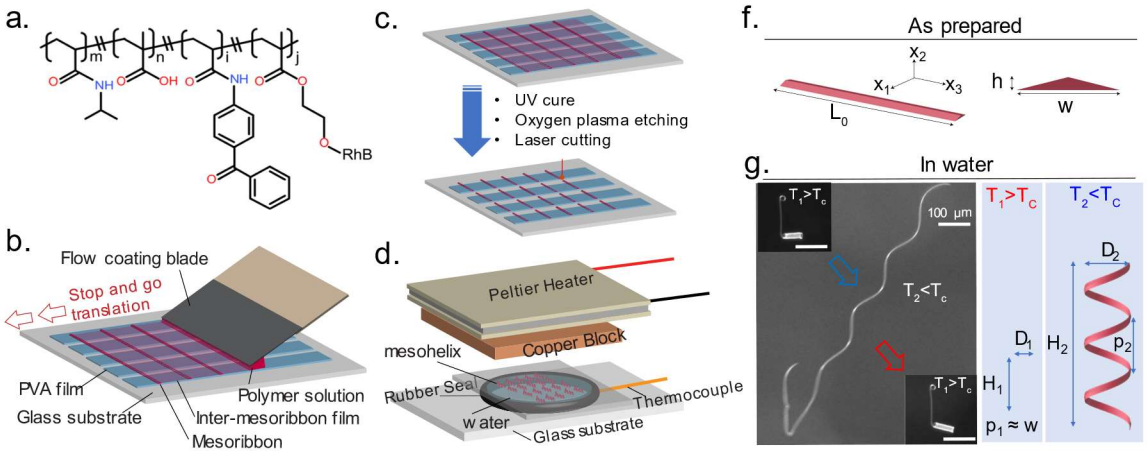

Figure 0.28 Experimental detail for the fabrication and the thermal actuation of mesoribbons in water (a) Chemical structures of (NIPAm(m)-AAc(n)-BP(i)-RhB(j) copolymer. (b) Schematic of flow coating process (c) Post-processing of mesoribbons to yield discrete mesoribbons with defined length. (d) Schematic of the thermal actuation setup used for the observation of temperature response of mesoribbons in water. (e) Coordinate system and geometrical parameters of mesoribbons. (g) FLM images of helical mesoribbons in the water at different temperatures (T_1 > LCST > T_2) (left); schematics of the helical geometries at different temperatures (right).

3.5.1 **Materials**

To fabricate PNIPAm mesoribbons by flow coating [107, 108], benzophenone acrylamide (BPAm) was introduced as a comonomer to induce a solid-state crosslinking reaction of PNIPAm after flow coating [109]. It allowed the assembly of water-soluble polymers to remain intact after released into the water. To observe mesoribbons, fluorescence microscopy (FLM, Axio observer, Carl Zeiss Microscopy GmbH) was utilized by using a trace amount of rhodamine B methacrylate (RhBMA) as a comonomer. In addition, acrylic acid (AAc) was introduced to specific samples for the implementation of pH responsiveness in its phase transition behavior. Polymers with various compositions were obtained based on the synthesis scheme previously described by Kim et al. [110].

All Materials were purchased from Sigma Aldrich and used without purification except for the initiator, azobisbutyroynitrile (AIBN). The AIBN was recrystallized in methanol before use. To prepared BPAm, 1.00g of 4-aminobenzophenone and 0.85 ml of triethylamine (TEA) were mixed with 10ml anhydrous dichloromethane (DCM) in 25 ml flask. The flask was then placed into an ice bath at 268 K for 10 min, followed by addition of 0.45 ml of acryloyl chloride in dropwise for 5 min. The solution was kept in the ice bath overnight (> 5 hr), followed by extraction two times each with 1M HCl, saturated $NaHCO_3$, and RO water. The solution was then dried with sodium sulfate (2 g) and filtered. After being dried under reduced pressure, an orange-colored solid was obtained (yield ≈ 90%). To synthesize RhBMA, rhodamine B isothiocyanurate (100 mg), 2-aminoethyl methacrylate hydrochloride (19.6 mg) and TEA (62.4 μl) were mixed in 24 ml of DCM and kept at room temperature overnight. The solution was treated with the same extraction process to give a red-colored oily product, which was mixed with 1,4-dioxane (2.9×10^{-4} M). The polymerization of thermal-responsive PNIPAm based copolymer was synthesized by dissolving NIPAm (1.5 g), BPAm (120 mg), RhBMa (20 ml) and AIBN (10 mg) in 60 ml of 1,4-dioxane. After a nitrogen purge for 10 minutes, the solution was kept at 348 K overnight. The copolymer was precipitated in cold diethyl ether and followed by drying under reduced pressure (yield 80%). In the case of a pH-responsive copolymer, NIPAm (1.5g), BPAm (60 mg), RhBMA (20 ml), and AAc (60 μL) were mixed in 60 ml of 1,4-dioxane and polymerized in the same procedure.

Chemical structures of PNIPAm-based copolymers were shown in Figure 3.6a. The molecular composition of the resultant polymers was characterized by ^{1}H-NMR (Burker Avancell 400) in deuterated chloroform ($CDCL_3$) as shown in Figure 3.7. Based

on the chemical composition of BPAm (i, mol %) and the input ratio (n, mol%) of AAC, the resultant polymers were named as BP(i) or BP(i)-AAc(n).

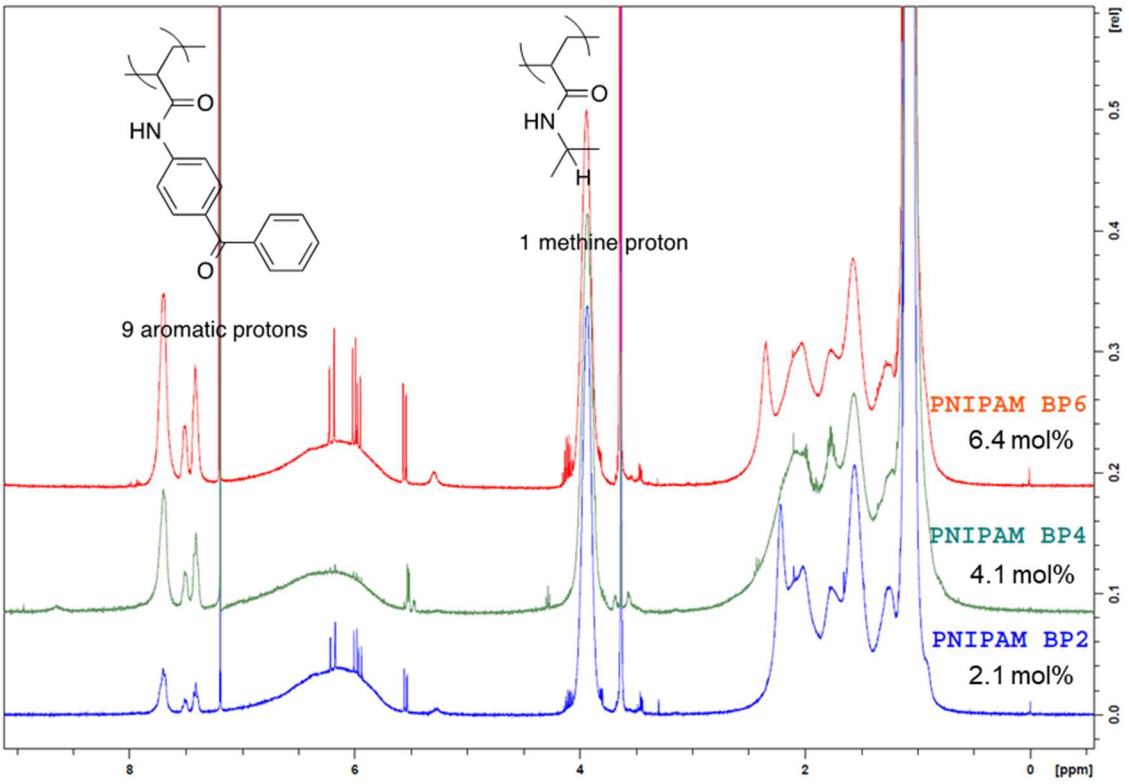

Figure 0.29 ^{1}H-NMR spectra of synthesized PNIPAm-based copolymer with different benzophenone acrylamide (BP) content

3.5.2 **Characterization of the mechanical properties of PNIPAm-based copolymers**

The temperature-responsive phase behavior of each polymers was analyzed by measuring the clouding point of 0.2% aqueous solution at a temperature change rate of 1 K min^{-1} from 293 K to 333 K. The lower critical solution temperature (LCST) of BP4 and BP2-AAc6 was ~ 300 K at pH 6, while the LCST of BP2-AAc6 was higher than 333K at pH 8.

The modulus of crosslinked BP4 hydrogel was analyzed by an indentation method using experimental setup shown in Figure 2.4. A disk of BP4 with uniform thickness (~ 1mm) was prepared by drying 20 wt % solution of BP4 in ethanol (99.5% Fisher scientific). The solution was dried at 343 K for 48 hours and annealed at 463 K for 5 minutes to relax residual drying stress. The disk was then UV-cured (360 nm, 20 mW cm^{-2}, 10 min. for each side) and submerged in water for 48 hours at 293 K to form a hydrogel. The disk was then equilibrated at a predetermined temperature for six hours. Using a spherical glass probe (R = 5 mm, Edmund optics), the gel was indented to predetermined depths (δ ~ 100 μm) while it was submerged in water at the specific temperature (Figure 3.8). The stress response was analyzed with respect to the indentation depth accounting the finite thickness of gel [111].

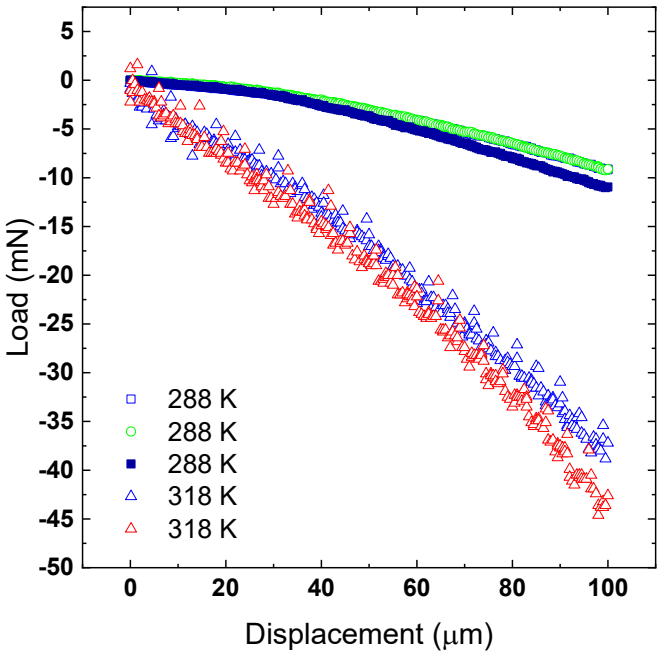

Figure 0.30 Plots of the relation between indentation depth and load of BP4 hydrogel with respect to the temperature condition

3.5.3 **Fabrication methods**

Before flow coating, glass substrates were cleaned by sonication using soap water, pure water, then isopropyl alcohol, and treated by UV-ozone (at 150 mTorr for 2 min). Then, a 200 mg ml^{-1} aqueous solution of poly(vinylalcohol) (PVA, 88% hydrolyzed, M_W = 78 kDa, Polysciences) was spun-coated on the substrate, generating a water-soluble sacrificial film (thickness ~ 100 nm). The film was engraved using a 30W CO_2 laser (Universal laser systems) to expose bare glass stripes (spacing ~ 2 mm, width ~ 200 μm) for the mesoribbons to be anchored to (Figure 3.6b). The glass substrate was then transferred onto a translating stage equipped with a Peltier heater.

To create mesoribbons onto the substrate by flow coating, 5 mg mL^{-1} solution of BP4 in 2-propanol (99.5%, anhydrous, Sigma Aldrich) were injected (20 μL) in between the glass substrate and the flow coating blade (a silicon wafer cleaved along the (100) crystal plane to form linear edge)(Figure 3.6b) [47]. The minimum distance between the flow coating blade and the substrate was set to ~ 200 μm. The mesoribbons were assembled perpendicular to the bare glass stripes. The dimensions of the mesoribbon were controlled by varying the stopping time of the translational stage (t_{stop} = 0.7 ~ 2.0 s at a translation speed of 1 mm s^{-1}). The temperature of the substrate was controlled to 312 K to yield fast evaporation of the solvent.

After flow coating, mesoribbons were cured under UV exposure (360 nm, 20 mW cm^{-2}, 8 min.) at the dried state, followed by oxygen plasma etching for the removal of thin-polymer film residue in between mesoribbons (Figure 3.6c). After cutting the mesoribbons with the CO_2 laser to allow them to move freely, the sample was introduced in between a rubber-sealed water bath (diameter ~ 30 mm, height ~ 2 mm) and a

conductive copper block (Figure 3.6d). The temperature of the bath was controlled by a Peltier heater. The temperature change was monitored by a T-type thermocouple placed in the water bath.

3.6 Results and discussion

3.6.1 Characterization of the geometries of as prepared BP4 mesoribbons

The geometries of as prepared BP4 mesoribbons were analyzed with an optical profilometer (OP, Zygo New View 7300) before released in water. Well-defined ribbons with uniform thickness profiles were prepared (Figure 3.9a). The thickness profiles of mesoribbons prepared at different t_{stop} (= 0.7, 1.0, 1.5, 2.0 s) were plotted in Figure 3.9b. The average height of ribbons depended on the stopping time but the aspect ratio for all ribbons was similar (w / $h \approx 29 \pm 2$).

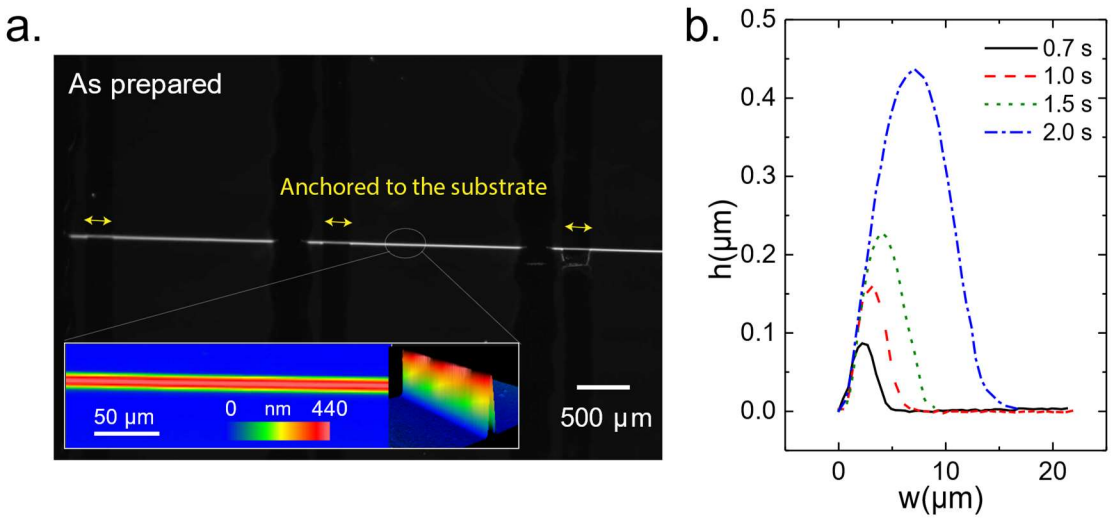

Figure 0.31 As-prepared mesoribbons on the substrate. (a) FLM image of mesorribons. Yellow arrows are showing the part of mesoribbon attached to the substrate (inset: OP images and its 3D reconstructed image). (b) Thickness profiles of mesoribbons prepared at different t_{stop}.

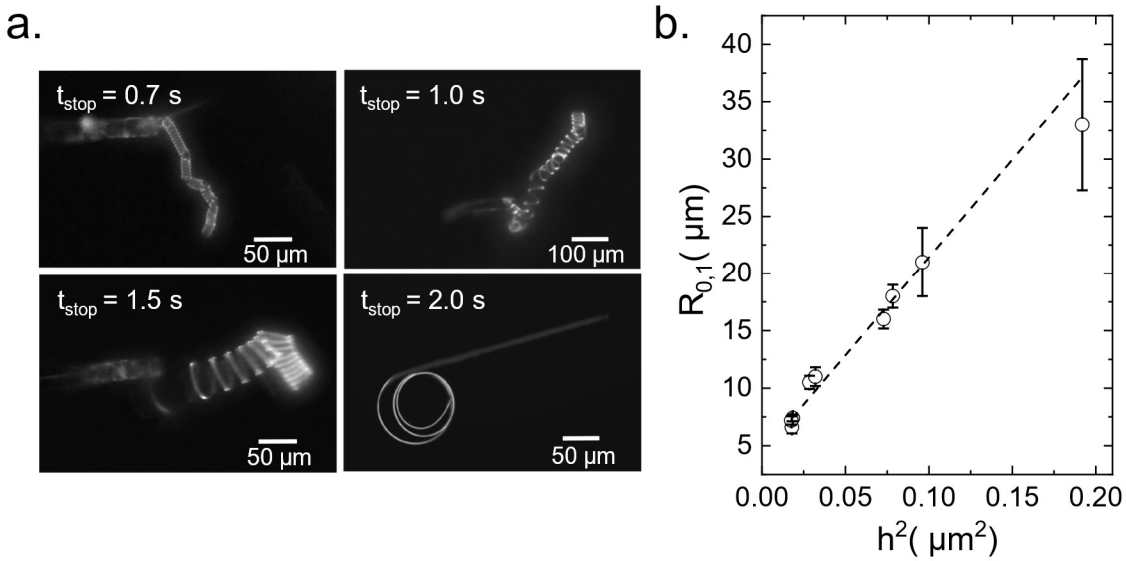

Figure 0.32 Helical mesoribbons in water at $T = T_1$. (a) FLM images of the helical mesoribbons flow coated at different stopping time (t_{stop}). (b) A plot of equilibrium helical radius as a function of (thickness)^2.

3.6.2 **Helical transformation of mesoribbons in the water at T > LCST**

After being introduced to water at a temperature ($T_1 \approx 318$ K) above the polymer's lower critical solution temperature, the mesoribbons spontaneously transformed to a helical geometry as shown in Figure 3.10a. The helical geometry is described by an axial helix length (H_1), pitch (p_1), and helical diameter (D_1), as illustrated in Figure 3.6g. Among the longest ones ($L > 1$ mm), several perversions, similar to those observed from asymmetrically tensioned elastic bilayer strips [112, 113], were observed (Figure 3.9a), thus suggesting that no preferred chirality exists.

In previous studies on the spontaneous helical transformation of mesoribbons [45, 46], the helical transformation phenomena have been explained with the solid-liquid interfacial tension (γ): isotropic surface stress associated with the deformation of solid [114]. Due to the asymmetric shape of the mesoribbons, which can be simplified as an isosceles triangular prismatic beam, the net-effect of interfacial tension acting on each

surface of the mesoribbonis sufficient to generate an out-of-plane bending force (torque) in directions determined by the mesoribbon's geometry. The bending force is balanced with the elastic restoration force of the solid. In this process, the bending direction is determined by the strength of the interfacial tension, the geometry of the beam, and the elastic modulus of the beam as modeled in Eq. 3.3 [45, 48].

$$\frac{1}{R} = 12\frac{\gamma}{Eh^2}\left(\sqrt{\frac{1}{4}+\frac{h^2}{w^2}}-1\right) \tag{3.3}$$

Where w is the width, h is the height, E is the modulus and γ is the interfacial tension between the ribbon (solid) and liquid media.

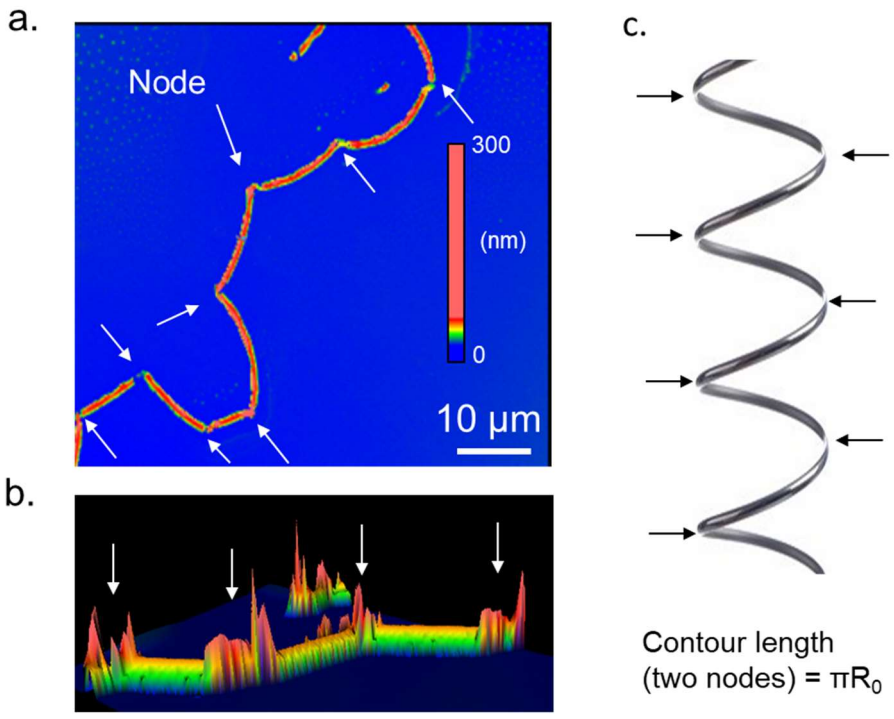

Figure 0.33 Geometric analysis of dried helices at T_1, (a) OP images, (b) 3D reconstructed image of (a) showing the thickness is doubled at kinks (=nodes), (not scaled). (c) Schematics of a helical geometry and positions of nodes. The contour length between two nodes is πR_0 ((arrows are showing nodes)

Since the helical diameter and the pitch were affected by flow condition of the liquid medium, such as thermal convective flows or Marangoni flows, an equilibrium helix radius (R_0) under no-flow condition was estimated based on the calculation of helix length using the helical diameter (D) and the pitch (p) observed from microscope image.

$$Helix\ length = 2\pi R_0 = \sqrt{\left(\frac{D}{\pi}\right)^2 + p^2} \tag{3.4}$$

To confirm the validity of the calculation, we estimated the actual helix length by measuring the contour length between nodes after the helix was dried at the same temperature condition (T_1) on the glass substrate (Figure 3.11). The difference between the calculated helix length by Eq. 2 and the measured contour length of dried mesoribbon was less than 10%.

3.6.3 **Thermal actuation of BP4 mesoribbons**

The thermal actuation of BP4 mesoribbon was induced by cycling the temperature of water between 318 K (T_1 > LCST) and 288 K (T_2 < LCST) at a rate of ± 0.8 K s^{-1} (Figure 3.12a). Reversible coiling and uncoiling transitions were observed during cycling (Figure 3.12b). The equilibrium helix radius was measured for T_1 ($R_{0,1}$) and T_2 ($R_{0,2}$) about 400 seconds later the temperature of bath reached the target temperature. For two different samples (h = 150 nm and 440 nm), the equilibrium helix radius change ratio (R_2 / R_1) was 406 ± 5% (Figure 3.12c).

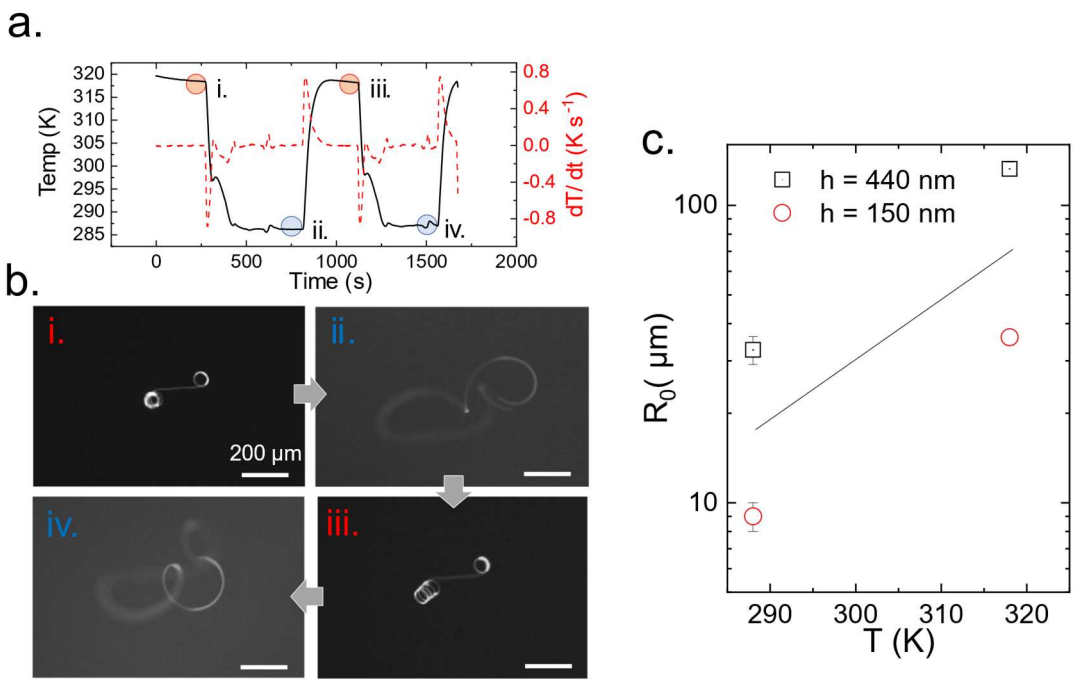

Figure 0.34 Thermal actuation of the helical mesoribbon in the rubber-sealed water bath. (a) Water temperature and temperature change speed as a function of time. (b) Time-lapse FLM images of the helical mesorribbon captured at the time denoted (a). (c) Equilibrium helical radius of mesoribbons at different temperatures.

3.6.4 **Estimation of the effect of interfacial tension on helical geometry change**

The equilibrium helix radius (R_0) was analyzed to estimate the extent which interfacial tension drove the curvature change. As shown in Figure 3.9b, $R_{0,1}$ scaled quadratically with the thickness of mesoribbons, in accordance with the Eq. 3.3. The elastocapillary length ($\beta = \gamma E^{-1}$) of BP4 was estimated ($\beta_1 = 9.7 \times 10^{-10}$ m, at $T = T_1$) by fitting to the experimental data.

We used the modulus value of BP4 hydrogel, $E_1 = 316$ kPa ($\pm$ 20) at $T = T_1$, to estimate the interfacial tension (γ_1) of the BP4 at the temperature condition. The estimated solid-liquid interfacial tension ($\gamma_1 = 0.31 \pm 0.02$ mN m^{-1}) was near zero, suggesting high hydrophilicity even at above LCST [100].

The interfacial tension of BP4 at $T = T_2$, γ_2, was calculated based on the assumption of isotropic swelling as Eq. 3.5.

$$\frac{R_1}{R_2} = \frac{\gamma_2}{E_2 h_2^2}\frac{E_1 h_1^2}{\gamma_1} = \frac{E_2}{E_2 \lambda^2}\frac{\gamma_2}{\gamma_1} \tag{3.5}$$

Where, E_2 (= 76 ± 9 kPa) is the modulus of BP4 hydrogel measured at T_2, λ is the swelling induced dimension change (L_2 / L_1 = 1.4 ± 0.1) determined by measuring contour length of short BP4 mesoribbon (L ~ 30 μm) at T_2 and T_1.

The calculated value of γ_2 is 0.036 mN m^{-1}, suggesting that such an insignificant change of interfacial tension could result big changes in helical coiling phenomena. In previous studies [99, 100, 115], the effect of phase transition upon the interfacial tension change of PNIPAm gel was often debated because of the negligible contact angle change within the error range of measurements and a large portion of water which remains at T > LCST. The helical coiling of mesoribbons, on the other hand, provided clear evidence and quantitative understanding.

3.6.5 **Dynamics of helical coiling actuation in viscous flow**

The dynamics of helical coiling was analyzed by measuring the contraction ratio (H_2 / H_1) and the specific speed ($v_s = \Delta H / H_1 s^{-1}$) of a helix in the presence of water flow. An experimental flow cell (10 mm × 20 mm × 2 mm, inner volume) made of polydimethylsiloxane (PDMS, Sylgard 184, Dow chemical) was used. The water inside of the cell was circulated by a peristaltic pump (Ismatec ISM936D) through two channels (inner diameter = 1 mm) connected to each side of the flow cell (Figure 3.13a). The temperature of inlet water was controlled by a custom-built, in-line heat exchanger and a

Peltier heater. The flow rate of water was set to 0.05 ml s^{-1}. However, it does not represent the actual flow condition experienced by mesoribbons since the helices were located near the boundary layer. Furthermore, convective flows, formed by the temperature change of supplied water, influenced the flow condition significantly.

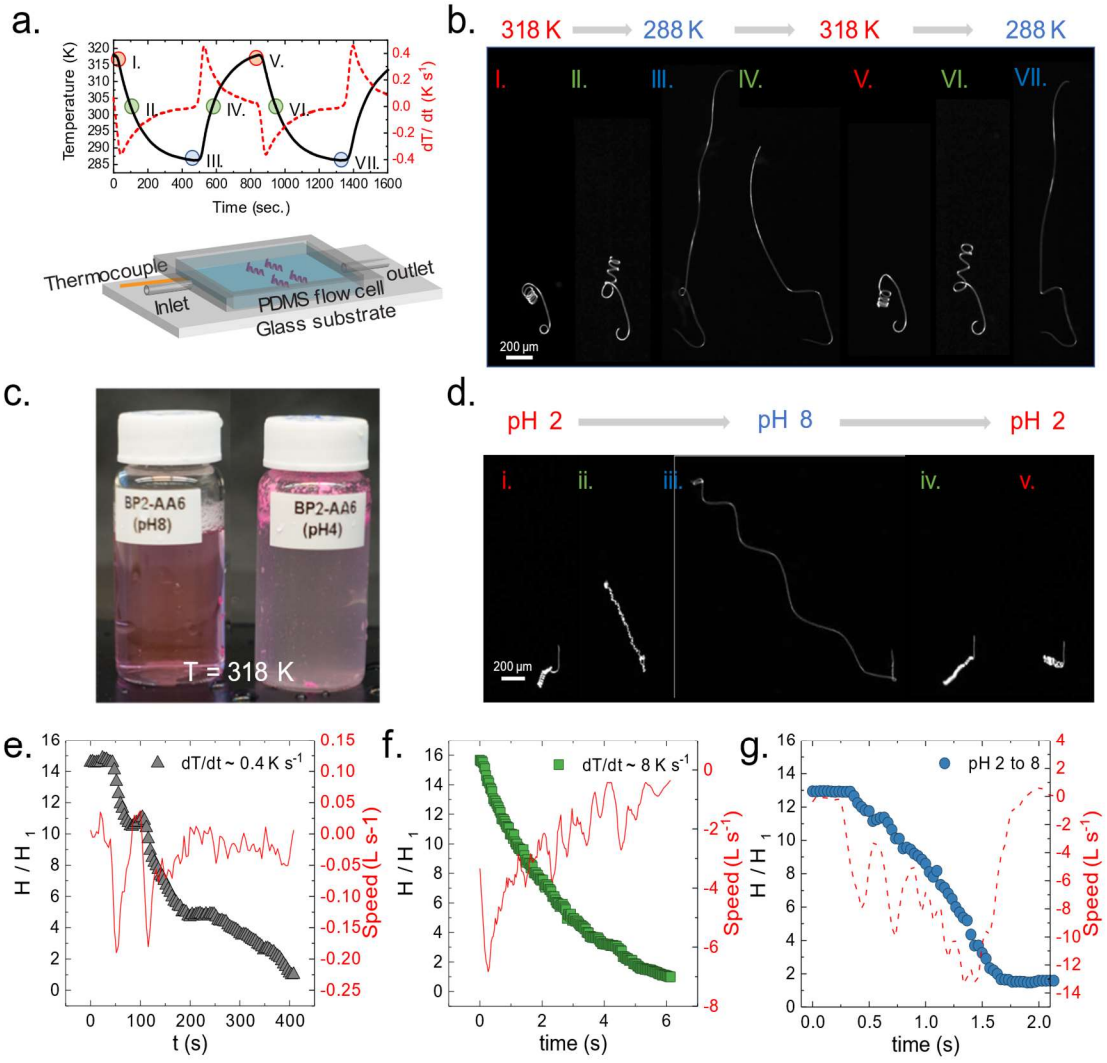

Figure 0.35 Helical coiling of mesoribbons in viscous flow. (a) Top: Plots of the water temperature and temperature change speed as a function of time; bottom: Schematics of the flow cell setup for the observation of helical coiling in viscous flow. (c) pH-responsive solubility change of uncured BP4-AAc6. (d) pH-responsive actuation of BP4-AAc6 mesoribbons at $T = 318$ K. (e-g) Normalized axial length (H / H_1) and specific speed of helical ribbons as a function of time

When the temperature was increased to T_1, a stretched helix coiled to a helix with a smaller radius and pitch. The measured contraction ratio reached up to 1600% (Fig 3.13e and f) and the speed of contraction was $v_{s,\,max} \approx 0.2\ s^{-1}$ (= 0.02 mm s^{-1}) at $dT / dt \approx 0.4\ K\ s^{-1}$) (Figure 3.13e). Notably, the contraction speed was improved at a faster temperature change rate ($v_{s,\,max} \approx 7\ s^{-1}$ (=1.4 mm s^{-1}) at $dT / dt \approx 8\ K\ s^{-1}$) (Figure 3.13f).

In previous studies [46, 116] on deformation of a helix in viscous flow, the axial extension ($\Delta H = H / H_0$, where H_0 is the axial length of helix in the absence of flow) of helix was modeled as a function of the helix geometry, material properties, tangential frictional drag coefficient ($\zeta_{||}$), and a flow velocity(v) as Eq. 3.6.

$$\frac{\Delta H}{L} = \frac{\zeta_{||} v R^2 L}{EI} \sim \frac{\zeta_{||} v R^2 L}{E w h^3} \tag{3.6}$$

The large extension of helical ribbons at T_2 is explained with the relation accounting the equilibrium helical radius change ($R_2 \approx 4.06\ R_1$), dimension change ($L_2 / L_1 = w_2 / w_1 = h_2 / h_1 = \lambda \approx 1.4$ for isotropic swelling), and the modulus change ($E_2 \approx 0.24\ E_1$) of BP4 mesoribbon, along with the assumption of no changes in frictional drag. The axial extension (ΔH) of the helix at T_2 is expected to increase to 25 times higher than that at T_1 under given flow conditions. Considering the finite extensibility of helix, a maximum compression ratio is expected to happen under a mild flow condition.

On the other hand, the speed of contraction could not be interpreted only considering the interfacial tension effect. Since the interfacial tension is constant at a given temperature, the same extent of force is applied when mesoribbons were initially released in water. The speed of initial helical contraction, however, did not exceed 0.1

mm s^{-1} in the experiments (Figure 3.14), while the maximum speed of contraction of the mesoribbon shown in Figure 3.13f was 1.4 mm s^{-1}.

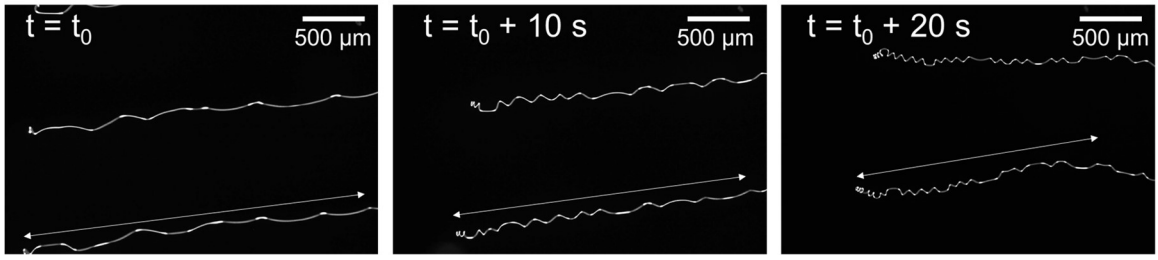

Figure 0.36 Time-lapse FLM images of the initial helical transformation the BP4 mesoribbons (h ~ 330nm) after being introduced in water at T_1, No external flow was applied

We hypothesized two possible mechanisms as the source of the additional coiling force: 1. inhomogeneous swelling induced bending; 2. transient swelling stress formation. To determine the presence of unintended inhomogeneous swelling strain distributions, which has been widely utilized for inducing the bending deformation of a PINPAm-based devices [23, 110, 117], we minimized the interfacial tension of solid-liquid but controlled the swelling ability by harnessing a unique phase behavior of PNIPAm in binary mixtures of water and alcohol, called cononsolvency [118–120].

In the mixture of water and 1-propanol, the LCST of PNIPAm decreases (less soluble) until the concentration of 1-propanol reaches to 15 mol%. On the other hand, at above 50 mol%, PNIPAm solubilizes even higher than 333 K [120]. We applied the same condition to identify the influence of swelling and interfacial tension on the helical transformation of BP4 mesoribbons. First, we released BP4 mesoribbons (h ≈ 440 nm) in the water at T_1. 1-propanol was then mixed to 15 mol%. Due to the cononsolvent condition, the swelling was minimized (L/L_1 -1 ≈ 10%), while the addition of 1-propanol

lowered the surface energy of medium [121], thus causing the helical radius increase (R_0 ~ 40 to 135 μm). As more 1-propanol was mixed (50 mol%), the mesoribbons swelled significantly (L/L_1 -1 ≈ 55%) and the curvature was reduced significantly (not measurable, Fig 3.15). This experiment confirmed that the helix was not formed by inhomogeneous swelling strain but by interfacial tension.

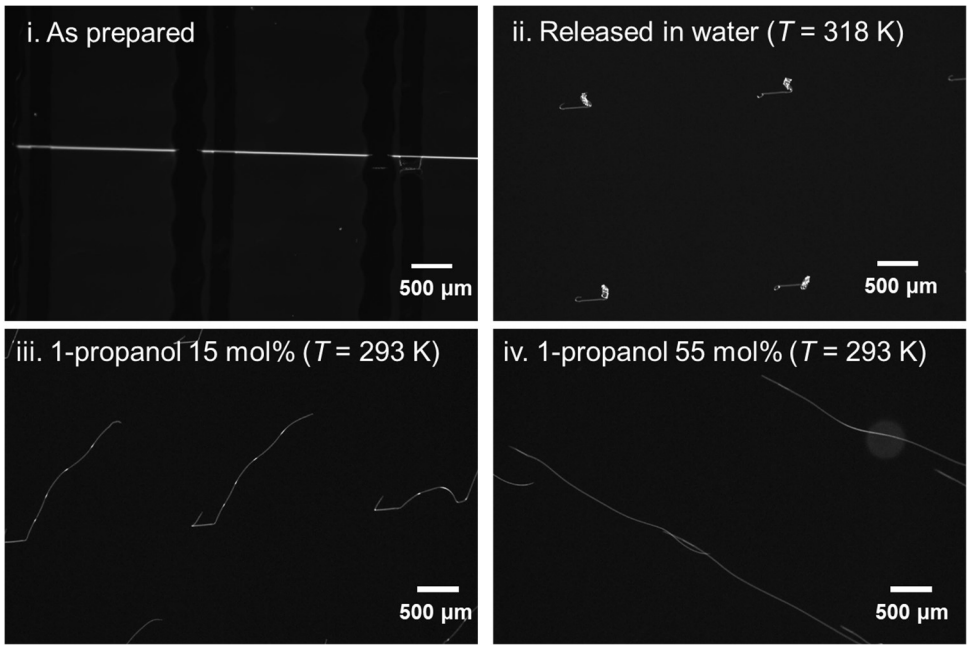

Figure 0.37 FLM images of the BP4 mesoribbons (h ~ 440 nm) at different compositions of 1-propanol in water

3.6.6 **pH change driven helical coiling of BP2-AAc6 mesoribbons**

The additional source of energy for the fast contractional motion was identified by an experiment conducted on BP2-AAc6 mesoribbons. Copolymerization of PNIAPAm with acrylic acid (6 mol%) has altered the phase behavior to be responsive to pH change at $T = T_1$ (Figure 3.13c). We used the pH responsiveness to drive helical coiling, instead of altering the temperature of the water bath. The pH of the medium was controlled by adding a basic solution (NaOH 0.01 mol %) or acidic solution (HCl 0.01 mol %) while

keeping the temperature at T_1. In the experiment shown in Figure 3.13d, BP2-AAc6 mesoribbons (h ≈ 550 nm) were released in the water at pH 2 at T_1. The pH of the solution was then cycled between 2 and 8. Similar to previous experiments, a transition between a tightly coiled helix ($R_1 \approx 23$ μm) and a loose ribbon ($R_2 \approx 115$ μm) was observed at the end of the transition, but the intermediate state was notably different from the temperature-controlled actuation of BP4. During the transition states (pH 2 to pH 8 or pH 8 to pH 2), helices with significantly small helical radius ($R_0 \approx 11$ μm) were observed transiently. The speed of contraction was significantly faster ($v_{s,\,max} \approx 13$ s^{-1} (= 3.2 mm s^{-1})) than the thermally driven actuation of mesoribbons.

Because the tight coiling was only observed during the transient swelling and deswelling process, the relevant mechanism differs from that based on a prescribed inhomogeneous swelling distribution [23, 110, 117]. We hypothesized that the asymmetric geometry of mesoribbons leads to coiling during the transient approach to and from swelling and deswelling states. To confirm this hypothesis, we made a macroscopic triangular prismatic beam ($h \approx 2.2$ mm, $w \approx 7.8$ mm, $L \approx 70$mm) from crosslinked PDMS. The size of the beam was significantly larger than its capillary length ($\gamma / E \approx 20$ mN m^{-1} / 10^6 Pa = 20 nm) so that interfacial tension effect was negligible. The beam was then submerged in a bath of good solvent (n-hexane, 99.9% Fisher scientific) to simulate the swelling behavior of PNIPAm mesoribbon at $T <$ LCST (Fig 3.16a). The swollen beam was then introduced in a bath of nonsolvent (ethanol) to simulate the deswelling process (Fig 3.16b). During the transient process of swelling and deswelling, the triangular prismatic beam underwent helical transitions. Noteworthily, the sign of the direction of bending was the opposite of each other: positive for swelling and negative for

deswelling. The negative curvature, generated by transient deswelling, coincides with the direction of bending expected from the interfacial tension-driven bending (Eq. 3.3).

With these results, it was proven that the helical contraction of hydrogel mesohelices was energized by a combination of interfacial tension and surface diffusion induced swelling stresses.

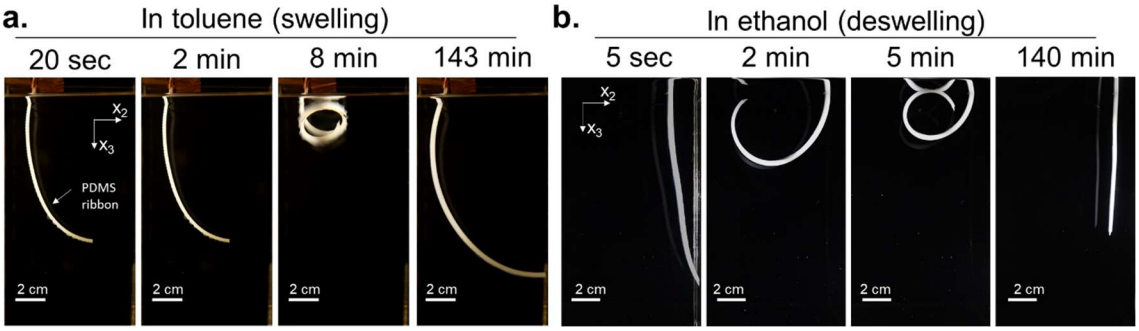

Figure 0.38 Surface diffusion induced transient helical deformation of macroscopic PDMS ribbons. (a) Time-lapse images of the PDMS ribbon during swelling in toluene. (b) Time-lapse images of the PDMS ribbon during deswelling in non-solvent (ethanol).

3.7 Conclusions

Through a combination of two surface-mediated phenomena: interfacial energy and surface diffusion, related to small, soft, and swellable materials, we have provided the first synthetic demonstration of Vorticella-like motion to realize fast and large helical contractional motion of mesoscale actuators underwater.

This simple and novel design principle, where the geometry of a gel controls the extent of and direction of bending, illustrates the applicability of the universal mechanisms to a wide range of polymer gels. This new deformation mechanism and actuation mode are promising for fast underwater actuators breaking through the difficulties of swimming locomotion.

3.8 Acknowlegement

This material is based upon work supported by, or in part by, the U. S. Army Research Laboratory and the U. S. Army Research Office under contract/grant number W911NF-15-1-0358.

CHAPTER 4

AUTONOMOUS SELF-REGENERATIVE SNAPPING MOTION OF NON-EQUILIBRIUM POLYMER GELS

4.1 Conceptual insights

We present a new design concept for creating a self-contained polymer system that can undergo regenerative autonomous snapping motions by utilizing non-equilibrium swelling state of gels.

4.2 Project summary

Novel design principles for creating regenerative, autonomous snap-jumping motion in a self-contained polymer system are developed. Transient metastable deformations observed during the drying of a polymer gel are exploited to generate mechanical bi-stability and realize multiple self-regulated snap-through transitions. Conditions needed to produce autonomous buckling transitions are detailed by considering the random buckling transitions of a rectangular strip. These lessons are then translated to a flat disk where autonomous buckling is harnessed to drive motion in a given direction. Novel fabrication strategies are utilized to tune device performance and highlight trade-offs in the design process when optimizing jumping kinetics ($t \sim 2$ ms, specific power ~ 310 W/kg) or specific energy output ($E_{out} \sim 2.2$ J/kg). A numerical model, validated experimentally, was used to confirm differential drying as the driving mechanism for autonomous buckling. These devices, and the broader underlying design principles, provide the first demonstration of an autonomous, self-regenerating high-

speed movement, marking a significant advance in the development of energy-efficient, high speed motion important for microscale robots and actuated devices.

4.3 Introduction

Power-amplified systems consist of springs and latches that enhance and mediate power output of motors. With the help of a latching mechanism, even a quasi-static development of force (Force x Velocity = Power ~ 0) from the motor can be converted to a high rate elastic energy release rate [122] (Energy/duration time). Buckling instabilities constitute a class of power-amplification mechanisms that harness the internal constraints of snap-through transitions as a geometric latch. Natural systems, such as plants and fungi, often use osmotic pressure development in cells as a primary actuation mechanism [13, 16, 123] limiting their dynamics and power by the transport kinetics of water. However, some carnivorous plant species, such as Utricularia [124] and Dionea muscipula [35] have overcome these limitations by adopting snap-through buckling in advantageously shaped trap-like leaves. These organisms actively regulate the spatial distribution of turgor pressure in their bi-stable leaves to initiate impulsive buckling transitions as well as to reset the structures for the next predatory snap [125].

While swelling-induced snap-through buckling of plant systems have inspired many recent demonstrations of snap-based polymer gel devices [38, 126, 127], most devices are limited to a single snapping event in the absence of external intervention. A life-like snapping motion, which is described as autonomous and self-regenerative, has not been attained in gel systems due to the lack of internal

self-regulating mechanisms. Autonomous swelling/deswelling was realized only recently by self-oscillation chemistry (B-Z reaction) [128, 129]; however, this process has not been capable of generating autonomous, high-speed motion. Repeatable jumping locomotion is seldom realized in engineered systems [130] due to difficulties in integrating multiple components (i.e., motor, spring, energy storage, and control) in an energetically and spatially efficient way.

In this work, these challenges are overcome by designing devices that harness the often overlooked processes of transient deswelling. This represents a shift from previous approaches where devices were designed solely around the equilibrium swollen and deswollen states. Such deformations have previously been accomplished by designing spatial gradients in the distribution of swelling response (i.e., hierarchical assemblies of materials with different crosslinking density or non-uniform chemical affinity between polymer and solvent) [15, 22]. However, this work demonstrates that exploiting transient deformations enables the generation of such motion in a system that is initially homogeneous in structure.

We constructed a simple model system composed of a homogeneous material subjected to minimal constraints during deswelling to determine both the mechanism of motion and the required conditions for repeatable jumping locomotion. Additional constraints were then imposed on the system in order to elucidate the role of confinement on the development of self-regulating forces and snapping dynamics. Understanding the mechanism of snap-through buckling dynamics enabled the fabrication of a snap-jumping device capable of generating

efficient, self-repeating locomotion. The richness of the design space is demonstrated by showing that simple modifications readily tune jumping performance (e.g., maximum jumping height, total vertical jumping height).

4.4 Background

4.4.1 Snap through buckling in nature

In nature, some plant species, such as *Utricularia* [124] (bladderworts) and *Dionaea muscipula* [12] (Venus flytrap) have evolved a snap-buckling mechanism to convert low power output of hydromorphic motors (Force × Velocity = Power ~ 0) to high powered motion of trap doors (Energy/duration time = Power >> 0). These organisms actively regulate the spatial distribution of turgor pressure in their bi-stable leaves to initiate impulsive buckling transitions as well as to reset the structures for the next predatory snap.

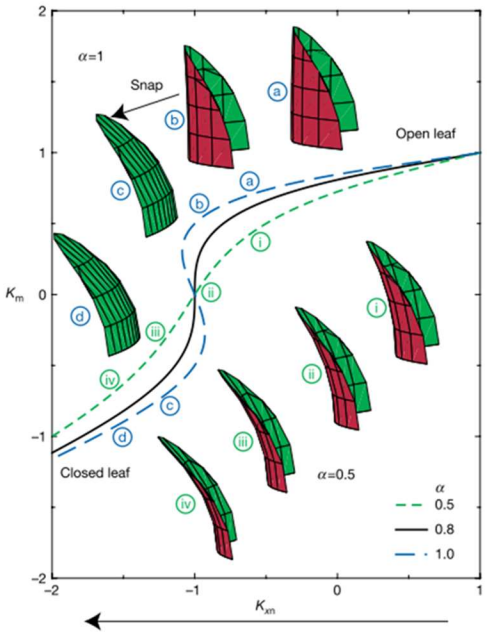

Figure 0.39 Curvature change of Venus flytrap leaves. Reprinted with permission from ref [12].

Forterre and coworkers discovered that the shape of leaves is determined by minimizing the elastic energy ($U_{el} = U_{bending} + \alpha U_{stretching}$) [12]. Where α is a dimensionless geometric parameter ($\alpha = L^4\kappa^2/h^2$), which determines the contribution between bending and stretching deformations regarding the leaf thickness h, the leaf size L, and the observed curvature of the open leaf κ. A snap closing of leaf was observed when α is larger than a certain value ($\alpha_c \sim 0.8$). Otherwise, the leaves do not snap or reach the closed state [12] (Figure 4.1).

4.4.2 **Prerequisite conditions for snap buckling transition**

The similar geometrical parameter that determines the transition between bi-stable states was derived by Pandey and coworkers [19]. Based on classic dynamic beam equations, they derived an expression of "stretchability" that measures the relative influence of bending and stretching energies ($S = \frac{h^2}{12L^2}$, where L is the length of the beam, h is the thickness). When the beam is compressed axially by ΔL, snapping transition happened when $\frac{d}{S} > 4\pi^2$, where d is ΔL/L (Figure 4.2).

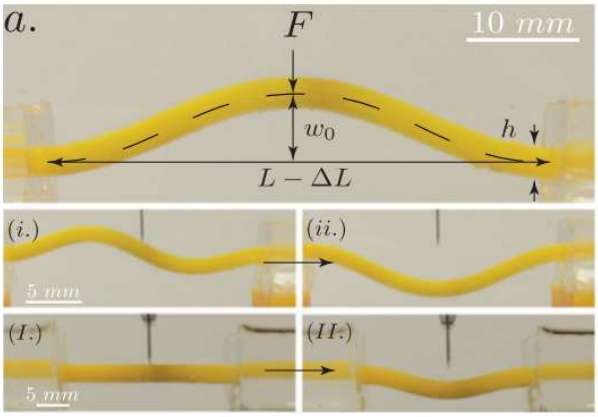

Figure 0.40 Snap-buckling of confined beam. Reprinted with permission from ref [19]

In the study, the snapping was induced by applying external force (F) at the middle point of the beam. They could also relate the indentation force with the geometrical and mechanical parameters of the beam. Noteworthily, the indentation force reached maxima and reduced during indentation (negative stiffness).

4.4.3 **Autonomous motions in swelling or deswelling objects**

In engineered systems, autonomous motion has been scarcely reported. The "self-walking" gel actuator developed by Maeda and coworkers [128], first showed a biomimetic motion by harnessing self-oscillating swelling-deswelling transition of a hydrogel-based on Belouzov-Zhabotinsky (BZ) reaction [131].

Another example of autonomous motion was found by Holmes and coworkers. During the non-homogeneous swelling-induced buckling of disk-shaped gel, an arbitrary rotation of buckle wave was found (Figure 4.3b). However, the mechanism for the dynamic buckling was not explained.

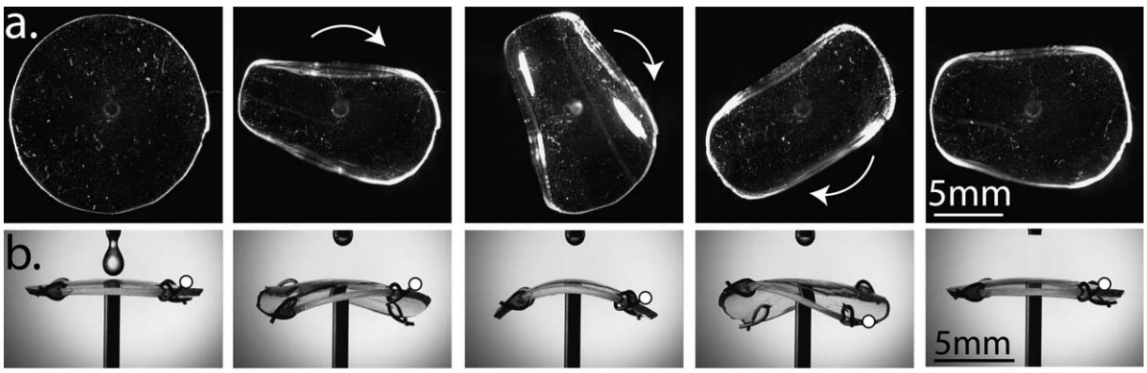

Figure 0.41 Dynamic rotation of buckling wave during transient swelling of a disk. Reprinted with permission from ref [34]

4.5 Experimental details

4.5.1 Materials

Crosslinked poly(dimethylsiloxane) (Sylgard 184, Dow chemical) (PDMS) and n-hexane were selected as a model material system for the identification of the mechanism of the spontaneous motions due to their well-characterized poroelastic properties [26]. N-hexane (> 99%, Fisher chemical) was selected as a solvent because of its high affinity to the polymer equilibrium swelling ratio, $\varepsilon_{eq} = (V_{swell} / V_0)^{1/3} - 1 = 0.43 \pm 0.02$, determined experimentally at equilibrium state of PDMS in n-hexane), fast diffusion kinetics ($D \sim 3.6 \times 10^{-9}$ m^2 s^{-1}, determined by an indentation method described in 2.5.3) and its fast evaporation speed (relative evaporation time = 8.4 [132], when n-butyl acetate = 1).

4.5.2 Preparation of PDMS sheets

PDMS sheets were fabricated by curing a degassed mixture (10 : 1 : 0.015 w/w) of prepolymer, curing agent (Sylgard 184, Dow Corning) and titanium(IV) dioxide nanoparticles (~21 nm, Sigma Aldrich), in between two glass substrates and an inserted spacer with various thicknesses ($h_0 \sim 0.3 \sim 0.6$ mm). The curing step was performed at 333 K oven for > 9 hours.

4.5.3 Preparation of PDMS discs

Cured PDMS sheets were cut and engraved by a laser cutter (Universal laser systems, resolution ~ 20μm) by controlling power and speed properly to ensure the uniform groove depth for entire samples.

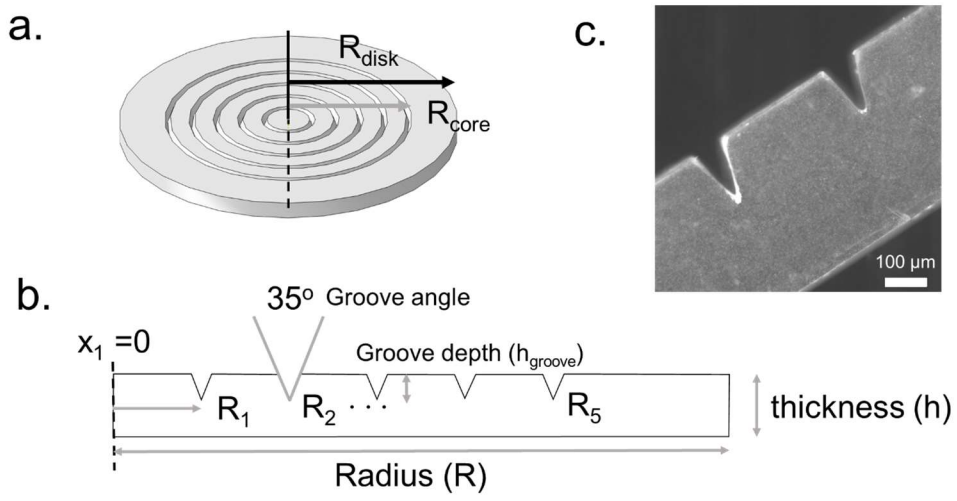

Figure 0.42 Design of grooved jumping shell (a, b) Schematics of grooved jumping shell showing geometric parameters. Concentric circular groove patterns (n = 5) was engraved (R_1 = 0.14 R_{disk}, R_2 = 0.28 R_{disk}, R_3 = 0.42 R_{disk}, R_4 = 0.56 R_{disk}, R_5 = 0.7 R_{disk}) on the one face of a PDSM disk. The groove depth and angle were set to ~ 35% of total thickness and ~ 35 degrees. (c) An optical image of the cross-section of a PDMS sheet (h ~ 0.4 mm) engraved by a laser cutter

4.5.4 **Solvent swelling of PDMS**

In this research, PDMS samples were fully swollen with solvent before analyzing deswelling phenomena. Time required for the swelling of a PDMS sample was determined based on a calculated value of $20\boldsymbol{\tau_p}$.

4.6 Results and discussion

4.6.1 **Continuous snap-through transitions of deswelling polymer beams**

We made a thin strip (thickness (h_0) ~ 0.2 mm, width (b_0) ~ 5 mm, length (L_0) ~ 60 mm) of PDMS by cutting a molded sheet. The strip was fully swollen with n-hexane, then placed on a sheet of black poly(tetrafluoroethylene) (PTFE) (Figure 1). PTFE was chosen to minimize the effect of friction on the dynamics of the strip, as well as to

prevent absorption of the solvent into the substrate. During the initial 90 seconds of the deswelling process, the strip deformed into buckled geometries (mode: 1, 2, or 3, κ_1, κ_2 $\neq$ 0) and continuously transformed into different shapes in a random manner. The complex buckling transitions consisted of smooth deformations and impulsive buckling transitions (Figure 4.5a) and quasi-static deformations.

To analyze the impact of local snap-through buckling transitions on the dynamics of the system. The change in the position of the apparent center of the mass (C.M, the average position of the captured optical image, Figure 4.5b. middle) and the one end-point (tip, Figure 4.5b. right) were tracked. The average speed of the C.M was ~0.007 m s^{-1}, and its maximum speed reached ~0.2 m s^{-1}. Meanwhile, the average speed of the tip was 0.018 m s^{-1}, and its maximum speed reached ~1.1 m s^{-1}. No regularity was found in the frequency of occurrence and the extent of the snap-through motion (Figure 4.5c).

In the case of isotropic volume contraction of a gel, the time required for de-swelling can be approximated as the same scale with the poroelastic time for the swelling process. With this approximation, the tip speed (V_{cont}) of contracting gel with one fixed end can be estimated as Eq. 4.2 by accounting initial dry length (L_0), equilibrium swelling ratio (ε_{eq}), the poroelastic time (τ_p), and the poroelastic diffusion coefficient of n-hexane (D_{hex} ~ 3.6 x 10^{-9} m^2 s^{-1}) in the PDMS. The poroelastic time of PDMS gel in Figure 4.5 was calculated as ~ 6.3 seconds. With that, the speed of moving end (tip) in a strip with one fixed end was estimated as ~ 1 mm/s.

$$V_{cont} = \Delta L / h \approx 0.9 \times L_0 \times \varepsilon_{eq} / 3\tau_p \quad (4.1)$$

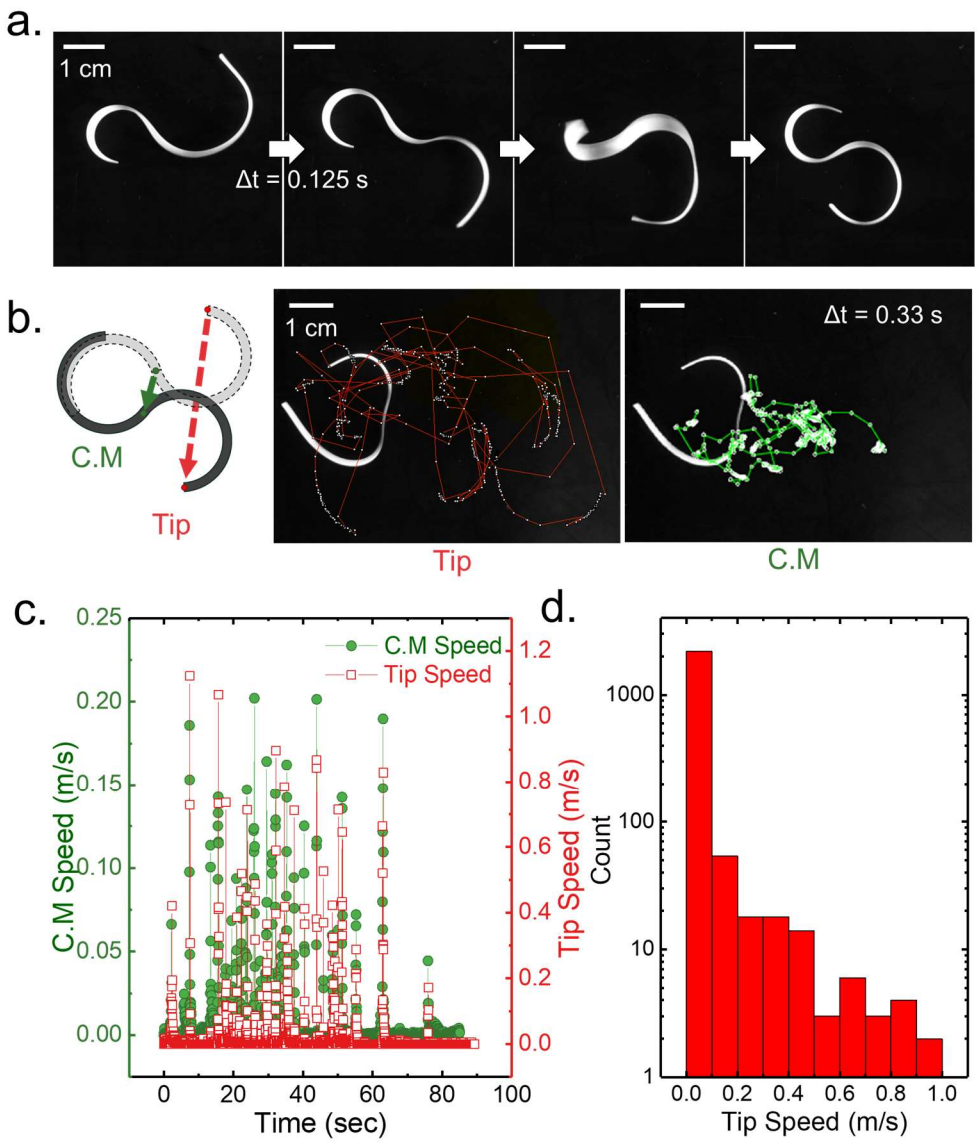

Figure 0.43 Continuous snap-through buckling transitions of a swollen PDMS strip (h_0 ~ 0.2 mm, b_0 ~ 5 mm, L_0 ~ 60 mm, as prepared). (a) Time-lapse images (interval = 0.125 s) showing buckling mode change (2 → 3 → 2) during two consequent snapping process. (b) (left) Scheme of the position change of the center of mass (C.M) and one endpoint (tip); Sequential position changes of the tip (middle) and the center of mass of the projected image (left) was captured every 0.33 seconds (lines were shown to guide the sequences). (c) Mean linear speed changes of the tip and C.M calculated by dividing the linear distance between two trajectories by the interval time. (d) Frequency distribution of the mean linear speed of the tip grouped into 10 regions based on the maximum speed observed. The average speed of one endpoint was 21 mm/sec. About 20% of the total time, the tip speed exceeded more than 10 times of the average speed.

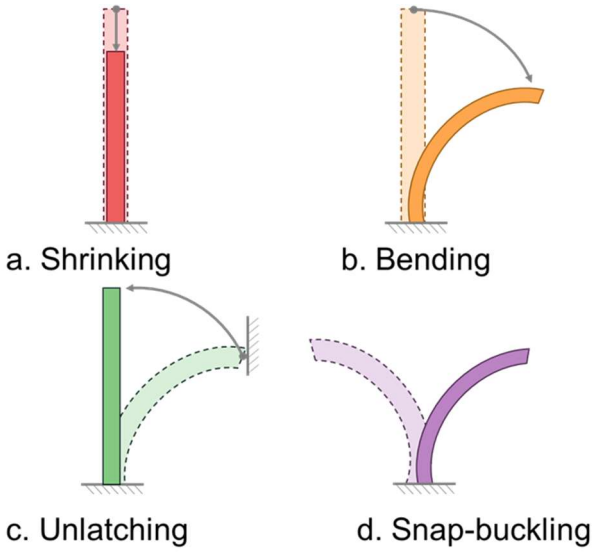

Figure 0.44 Four possible deformation modes of a deswelling PDMS strip.

The expected speed of a tip by a bending deformation was estimated based on the previous studies on the non-homogeneous swelling induced deformations [34]. According to the study, after the inhomogeneous swelling condition was applied by the localized application of n-hexane on PDMS beam, about two times of the poroelastic time of the beam was required for generating maximum bending curvature ($\kappa h/\varepsilon_{eq} \sim 0.35$) in the structure. Again, assuming similar dynamics between swelling and de-swelling process, the maximum speed of the tip was calculated as ~4.6 mm/s by Eq. 4.3.

$$V_{bend} = \frac{L_0 \times \left(1 + \varepsilon_{eq}\right) - \frac{1}{\kappa}}{2\tau_p} \tag{4.2}$$

Statistics on the occurrence of different speeds of a tip during the initial de-swelling process, showed (Figure 4.5d) that the tip moved within the same magnitude of the speed expected from the contraction or bending deformations. On the other hand,

about 20% of the duration, the tip speed exceeded more than two magnitudes higher than the expected speed of continuous deformations. Along with the changes in the sign of the curvature (Figure 4.5a), the extraordinary fast kinetics supports the idea that the motion was driven by snap-through buckling transitions.

We conducted a control experiment to check the effect of dye particles or non-uniform drying condition applied by the impermeable substrate by placing a fully swollen transparent PDMS strip in a glass desiccator (~ 100 x 100 x 200 mm), while hanging vertically with one end pinned to a thin wire connected to the lid of the desiccator. The lid was closed immediately upon placement in the desiccator to minimize the influence of external air flow on observed motions. The strip still underwent snap-through buckling transitions disproving the effect of non-homogeneous deswelling condition or heterogeneous material compositions on the generation of snap transitions (Figure 4.7).

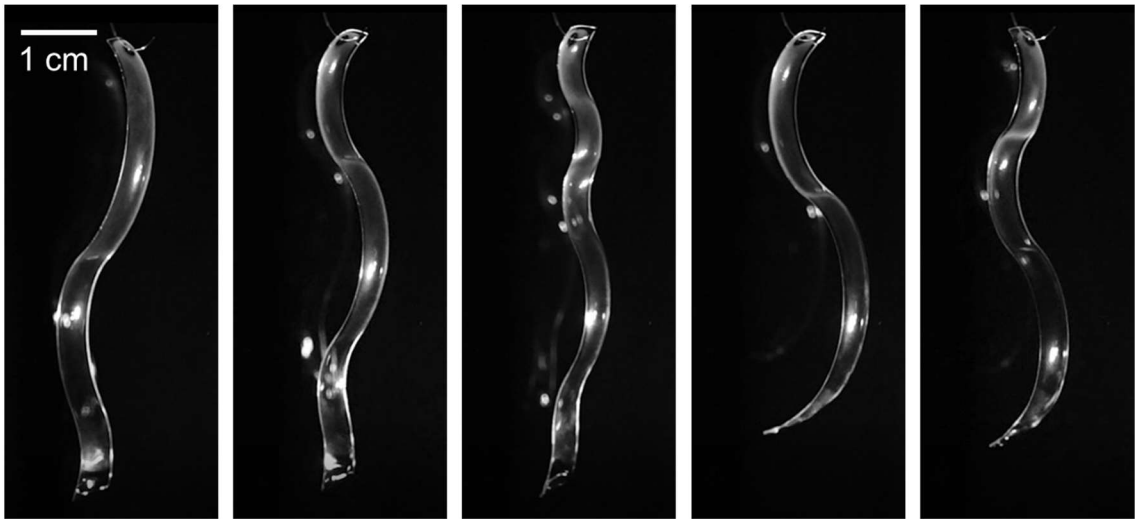

Figure 0.45 Various deformed shapes of a free-deswelling PDMS strip. A PDMS strip (h_0 ~ 0.2 mm w_0 ~ 5 mm, L_0 ~ 50 mm) initially swollen with n-hexane was placed in a desiccator with one end connected to the lid by wire

According to previous studies on the dynamics of snapping beams [19], three conditions must be satisfied to induce snap-through buckling transition: **1.** sufficiently large lateral constraints, **2.** a higher tendency for bending than compression (longitudinal deformation), and **3.** sufficient transition force for curvature sign change. In this experiment, the extent of lateral confinement is controlled by the non-uniform distribution of the evaporative flux of the solvent along the length of the beam. When the solvent evaporation is sufficiently faster than the internal diffusion rate (diffusion-limited), crosslinked PDMS networks contract (deswell) faster at the near-edge region than the mid-face region due to the large portion of surfaces exposed to air.

The proposed buckling mechanism was modeled as Figure 4.8 using a simple numerical model that we developed based on an analogy between diffusion and heat transfer phenomena [133]. We input modified thermomechanical parameters (heat expansion coefficient (α), heat transfer coefficients for bulk and surface heat transfer) to reflect the volume change of the PDMS strip by imbibition of n-hexane and the diffusion and evaporation kinetics of the solvent in/on the PDMS strip. Notably, experimentally measured equilibrium swelling ratio ($\varepsilon_{eq} = 0.43$) and poroelastic diffusion coefficient of n-hexane ($D = 3.6 \times 10^{-9}$ m^2 s^{-1}) was used as modeling parameters.

To model the deswelling induced buckling transition of the PDMS strip ($h_0 \sim 0.2$ mm, $w_0 \sim 5$ mm, $L_0 \sim 60$ mm), we set the equilibrium swollen state ($\varepsilon / \varepsilon_{eq} = 1$) as the initial condition of the analysis. As the loading condition, a homogeneous deswelling was then applied (at $t = 0$) by changing solvent concentration of the medium to zero. The transport of solvent from the bulk of strip to the medium was mediated by the interfaces, where the largest concentration gradient was applied, thus the deswelling rate (r) was

faster at the interfaces, termed as corners (the green region in Figure 4.8b), than the central region, termed as center (the red region in Figure 4.8b). The faster deswelling of corners exerted compressive stresses on the center (Figure 4.8c), causing buckling of the strip. The effective strain of the strip was modeled as:

$$\frac{r_{corner}t_{dry} - r_{center}t_{dry}}{r_{center}t_{dry}} = \left[\frac{\varepsilon_{corner}(t) - \varepsilon_{center}(t)}{\varepsilon_{center}(t)}\right] \tag{4.4}$$

It was compared with the critical buckling strain (ε_c) of the strip, which was derived as:

$$\varepsilon_c = \frac{Pc}{A \cdot E} \approx \frac{E \cdot I}{L^2} = \left(\frac{h}{L}\right)^2 \tag{4.5}$$

Where P_c is the Euler's critical buckling force, A is the cross-sectional area of strip, and I is the moment of inertia for bending.

The ε_c for the strip was in the order of 10^{-5}, therefore the strip could be buckled during the deswelling process.

If the thickness of a strip is sufficiently small, the stress applied by contracting edges is large enough to cause lateral buckling of the strip due to the scaling relation between the critical buckling strain and geometries of a strip ($\varepsilon_c \propto (h / L)^2$).

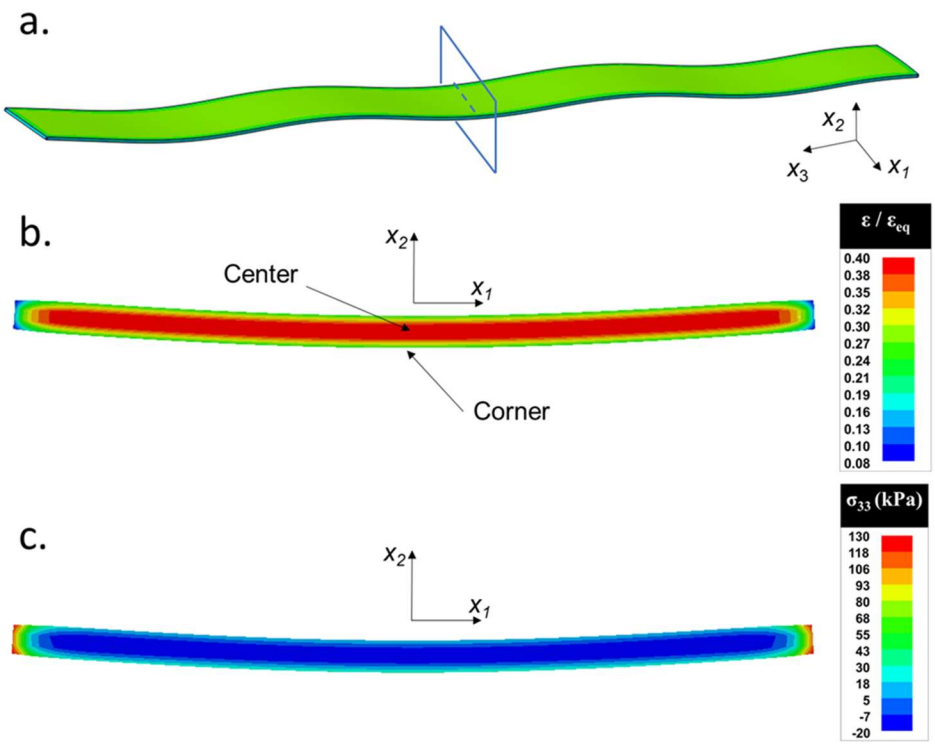

Figure 0.46 FEM of buckling phenomena expected in *the* deswelling PDMS strip ($h_0 \sim 0.2$ mm, $w_0 \sim 5$ mm, $L_0 \sim 60$ mm). (a) Contour plots of the normalized swelling ratio ($\varepsilon / \varepsilon_{eq}$) at t ~ 12 s. (b) The normalized swelling ratio distribution in the midplane of the PDMS strip (the blue box in (a)). (c) Longitudinal stress distribution in the midplane of the PDMS strip

A remaining question is then, what is the source of transition forces that regenerate in self-regulating manner. We hypothesized four possible mechanisms that could generate transition forces which changes the direction of forcing in a self-regulating manner. The four proposed mechanisms are: 1. Internal migration of solvent from compressed regions to stretched regions (stress-induced solvent redistribution); 2. Differential vapor pressure of solvents on curved surfaces (Kelvin effect); 3. Differences in the surface area across the neutral bending axis; 4. Slower de-swelling of concave region (negative average curvature) due to the stagnation of solvent vapor in the concave region.

Among these proposed mechanisms, the stress-induced solvents migration effect was disproved by an experiment conducted in the water. When a buckled strip, which will readily undergo snap transitions in the air, was submerged in water, no buckling transition was occurred due to the exclusion of the de-swelling condition.

The vapor pressure differences at the curved surfaces (Kelvin effect [134]) was also neglected, due to the negligible differences (< 0.01%) in the vapor pressure between the two surfaces as Eq 4.6.

$$\ln\frac{P}{P_0} = \frac{2\gamma V_m}{rRT} \tag{4.6}$$

Where, V_m is mothe lar volume of solvent, γ is the surface tension of liquid, r is the radius, R is the gas constant, and T is the temperature.

The surface area differences between the convex (mean curvature > 0) and concave (mean curvature < 0) surfaces in the buckled structure can significantly affect the volume change rate as the normalized surface area differences in the buckled structure can be as large as 7.5% for the strip in Fig. 1a (h = 0.3mm, $r_1 \sim r_2 \sim 8$ mm, measured) by Eq 4.7.

$$\frac{\Delta \mathrm{A}}{\mathrm{A}} = \mathrm{h}\left(\frac{1}{r_1} + \frac{1}{r_2}\right) \tag{3.7}$$

In the case of the fourth hypothesis, the effect couldn't be quantified due to the complexity of the swelling phenomena. However, the mechanism also impacts the formation of indentation force as the same direction as the differential surface area effect by applying counter forces to the buckled directions.

4.6.2 **Generation of internal, self-regulating transition forces in the buckled polymer gel strips**

In a free deswelling beam, the non-uniform evaporation of solvent along the beam, which controls lateral constraints, is controlled by the thickness, solvent, and interactions with the substrate. These factors couple to influence the speed and number of snapping events during deswelling; therefore, to understand their independent relationship to the snap-through characteristics rigid end grips were used to apply a specified degree of lateral confinement. In Fig 4.9a, Scheme of the process for generating self-repeating snap transitions in externally confined polymer gel strips and the coordinate-system were shown. The initial lateral confinement (d_0) was denoted as the rigidly applied displacement of the beam ends (ΔL) divided by the initial value of the length of the swollen strip ($L_{swell} = L_0 \times \varepsilon_{eq}$). The deswelling PDMS strips underwent snapping transitions with the sign of curvature (κ_1) alternating over short times (< 0.3 s) upon application of the lateral constraints. The transitions occurred in the form of antisymmetric, mode-2 Euler buckling, which is energetically favored over symmetric transitions [19].

The total number, frequency, and speed of snap transitions during de-swelling depended upon the extent of lateral confinement and thickness. The number of snap transitions had a complex dependence on beam thickness and lateral confinement. In Figure 4.9b, time-lapse of the snap-through transition process (modes 1 → 2 → 1) of a buckled strip (h_0 = 0.5 mm, w_0 = 5 mm, L_0 = 50 mm) constrained by moving a linear actuator (ΔL = 10 mm) were shown (top). The dependence of number of snap-transitions on the thickness and the extent of initial confinement were analyzed too (bottom). Lateral

constraints that were too small and too large limited, or even prevented, snap transitions, thus suggesting that the number of transitions for a beam of given dimensions can be maximized with an appropriate degree of lateral constraints (e.g. $h_0 \sim 0.5$ mm data in Figure 4.9b). In fact, the lateral confinement can be changed continuously to further enhance the number of transitions (more than 20 were observed for $h_0 \sim 0.5$ mm when the degree of confinement changed at a frequency of 0.0012 s^{-1}). Similarly, the number of transitions can also depend non-monotonically on thickness. This trend originates from the existence of the two time-scales: the time for the reduction of the confinement due to the volume contraction and the time for the development of the internal transition forces due to asymmetric evaporation. For thicker beams, longer development times for reaching the critical transition force are required, while for thinner beams, lateral confinement is reduced more quickly due to faster volume contraction rates. Both decrease the total number of snap transitions during the deswelling process. While the number of snap events has a complex dependence on lateral confinement, the maximum speed achieved depended directly on lateral confinement (Figure 4.9c,d), similar to the trend found for externally-induced snap transitions of buckled beams [19].

Additionally, we tested the effect of the loading condition on the dynamics of snap transition by changing the solvent from n-hexane to toluene (> 99 %, Fisher chemical) which has low poroelastic diffusion coefficient ($D_{tol} \sim 1.0 \times 10^{-9}$ m^2 s^{-1} in PDMS) and low evaporation rate (~ 2.24 relative to n-butyl acetate) but similar equilibrium swelling ratio ($\varepsilon_{0,tol} \sim 0.40$). While the maximum achievable speed was not dependent upon solvent properties (Figure 4.9d), the number of transitions did increase for toluene swollen systems due to the longer evaporation times. Importantly, the

independence of maximum speed on solvent choice emphasizes that the snap dynamics are dictated solely by the dimensions and degree of lateral constraint.

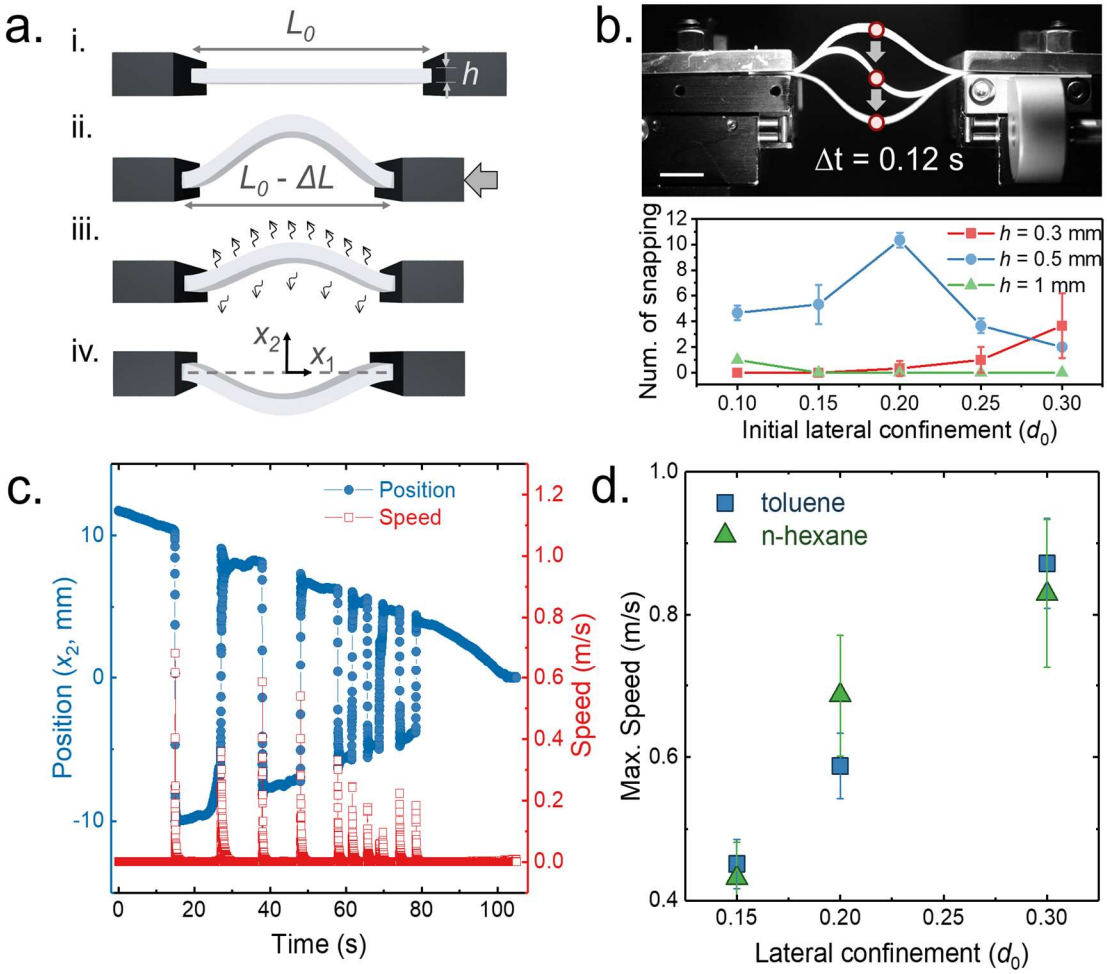

Figure 0.47 Autonomous snapping motions of externally buckled PDMS strips. (a) Scheme of the process for generating self-repeating snap transitions in externally confined polymer gel strips and the coordinate-system (b) (top) Time-lapse of the snap-through transition process (modes 1 → 2 → 1) of a buckled strip (h_{dry} = 0.5 mm, w_{dry} = 5 mm, L_0 = 50 mm) constrained by moving a linear actuator (ΔL = 10 mm); (bottom) number of snap-transition observed for different thicknesses and various extent of initial confinement. (c) A plot of the vertical displacement and the speed changes of middle point of the strip shown in the image of (b). (d) Maximum speed dependency on the solvent used at different initial lateral confinements (d_0).

4.6.3 Repeatable snap jumping motions of self-formed, self-contained jumping shells

The lessons provided by the repeated, fast snap transitions of the de-swelling strip suggested that an appropriately designed geometry could provide repeated, directed motion. As a demonstration of this concept, we fabricated an axisymmetric shell structure, which allowed for a predetermined buckling mode and location of maximum displacement. Furthermore, the shell structures were designed to have structures to provide integrated constraint and maximum transient swelling strain gradients through the thickness, thus enhancing the corresponding snap transition forces (Figure 4.10).

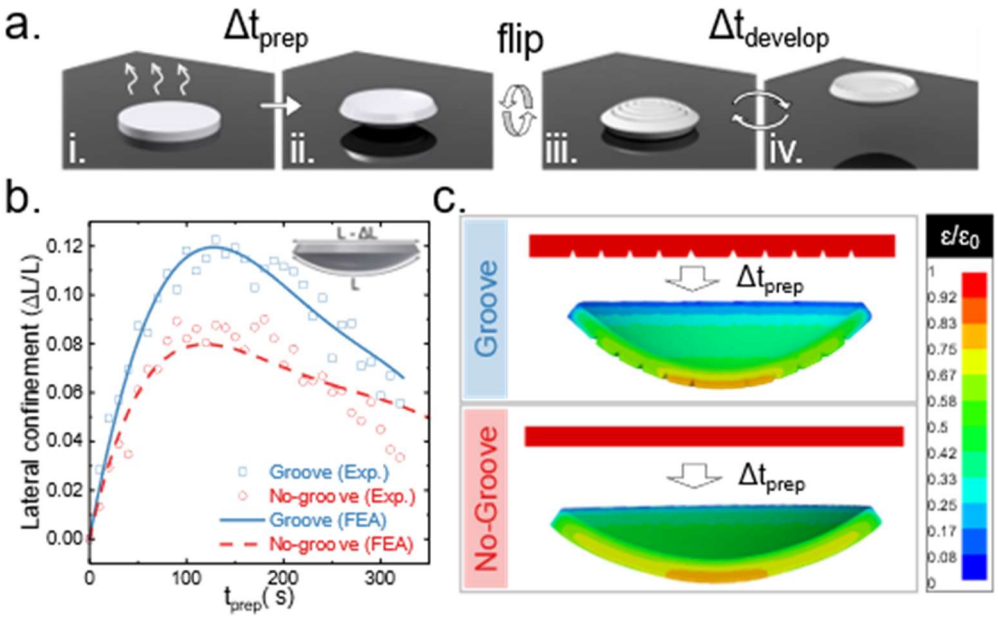

Figure 0.48 Transient formation of a hemispherical shell from a flat disk. (a) Scheme of the formation of a hemispherical shell under asymmetric deswelling condition (i, ii), and its jumping motion after a certain period of time ($t_{develop}$) after being flipped manually (iii, iv). (b) The progress of the extent of buckling evolved in a PDMS disk (R_0 = 5 mm, h_0 = 0.6 mm). The disk with circular groove patterns on one side of surfaces was deformed to more confined structures than the disks with no groove pattern. The similar definition for accounting lateral confinements ($d = \Delta L / L$) was used to draw an analogy to the previously discussed systems. (c) The time-dependent deformation of discs was modeled numerically. The contour plots represent the normalized swelling ratio ($\varepsilon/\varepsilon_{eq}$) distributions in the structure.

The repeated-jumping shell structures were developed from a homogeneous PDMS sheet. Circular discs were laser cut from the PDMS sheet, and circular groove patterns were laser engraved in the core region (R_{core} / R_{disk} = 0.7). The discs were swollen with a good solvent (n-hexane) to a fully equilibrated, flat geometry. The swollen discs were then dried for a specified time (Δt_{prep}) with the groove side facing a substrate. Upon drying, the discs deformed into a hemispherical cap due to the evolution of transient swelling strain mismatch in the thickness direction ($\varepsilon_{groove} > \varepsilon_{no\text{-}groove}$) as well as the radial direction ($\varepsilon_{core} > \varepsilon_{annulus}$). The reason for the strain mismatch in radial direction has already been explained above. The additional generation of the strain gradient through the thickness direction can be explained with the excess solvent trapped inside the grooved regions due to capillary effects.

To harness the snap transitions for jumping, the snapping shells were placed on a substrate. The impermeable substrate served two purposes. First, the de-swelling rate differences between the top and bottom surfaces were greatly amplified by the retardation of evaporation at the surface contacting the substrate. Due to this asymmetric drying, when a hemispherical shell was placed on a substrate in a concave down shape (Figure 4.10a), the time ($\Delta t_{develop}$) required for developing transition forces was much shorter than the time required for the free-standing condition. In addition, hemispherical shells with larger lateral confinement were formed by applying the asymmetric de-swelling condition. Depending upon how long the drying discs placed on the substrate (t_{prep}), the lateral confinement evolved from zero to a maximum value (at $t / \tau_p \sim 5$) then relaxed back to the flat geometries after a prolonged period of time (at $t / \tau_p > 15$)(Figure 4.10b).

The circular groove patterns helped to generate higher and more stable curvatures compared to discs without groove patterns (Figure 4.10b).

The occurrence of snap transition depended on the dimensions of the discs in these experimental conditions. Only certain hemispherical shells underwent limited snap-through transitions during the prolonged drying process in the air. In Figure 4.11, jump heights of disks with various aspect ratios ($2R_0$ / h_0) and thicknesses were plotted regardless of t_{develp} to provide rough ideas on the effect of geometries. AR = 16 was chosen for the rest of analysis due to the high performance it showed.

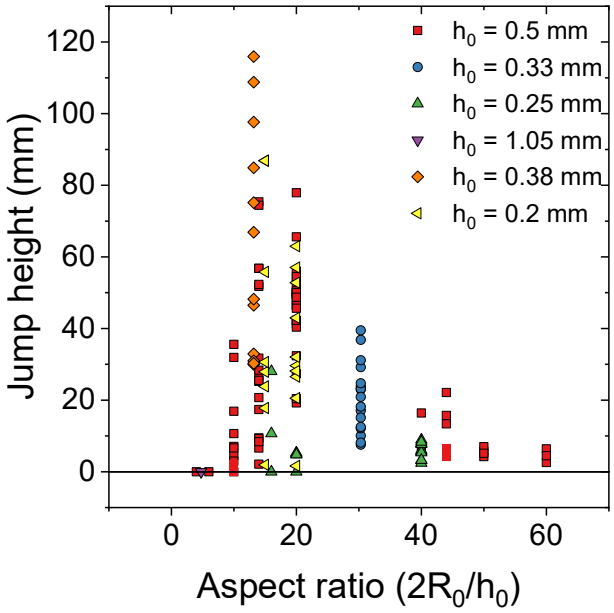

Figure 0.49 Snap-jumping heights of PDMS disks with various aspect ratios and thicknesses. Data were shown regardless of t_{develp} to provide rough ideas on the effect of geometries.

The dynamic jumping performance of the formed shells was analyzed by recording the first snap-through transition with a high-speed camera (Photron Fastcam SA3) at 20,000 fps. In Figure 4.12a, time-lapse images of snap-transition of a hemispherical shell (R_0 = 4 mm, h_0 = 0.6 mm, t_{prep} = 40 s) were shown. The buckling

transition finished within 2 milliseconds after a prescribed $\Delta t_{develop}$. The absolute timescale was not measured due to the variability in the deswelling caused by the high-intensity light required for video. Instead, the vertical speed of a tip, representing the speed of snapping motion, and the speed of the C.M were analyzed in Figure 4.12b. The maximum speed of the C.M (~ 1.5 m/s) reached about 50% of the tip speed (~ 3 m/s). The following peak shows that there were vibrations after a snapping event.

Not only did the deswelling-induced snap transitions produce a single high-speed jump event, but the self-formed shells also underwent multiple snap-transitions without additional swelling. In Figure 4.12c, Time-lapse images (interval = 0.33 s) of consecutive snap jumping motions of a hemispherical shell (R_0 = 5 mm, h_0 = 0.6 mm, t_{prep} = 180 s) were shown without re-swelling of solvent. For the analysis of autonomous, self-repeating jumps, we measured the vertical jumping heights and the weights of the shell with a balance underneath the substrate (Figure 4.12d) in order to understand the effect of the preparation time on the dynamic performance.

Based on the vertical jump height (ΔH) and the mass (m) of the system, the output energy by snapping ($\Delta E = mg\Delta H$, where g is the gravitational acceleration) at different conditions were calculated (Figure 4.13). The output energy of the initial jump was found to reach an upper limit (ΔE_{max} ~ 50 μJ, ΔH_{max} ~ 8.5 cm) at preparation times of approximately 180 s similar to the trend of lateral confinement change during the preparation step (Figure 4.13b). A peak specific power density (~ 280 W kg^{-1}) of the jumping shell was calculated based on the initial mass (m ~ 80 μg) and the duration of snap-through motion (2 ms). Surprisingly, it was comparable to the peak muscle power of high performance jumping animals (e.g. Cuban treefrog ~ 300 W/kg [135]).

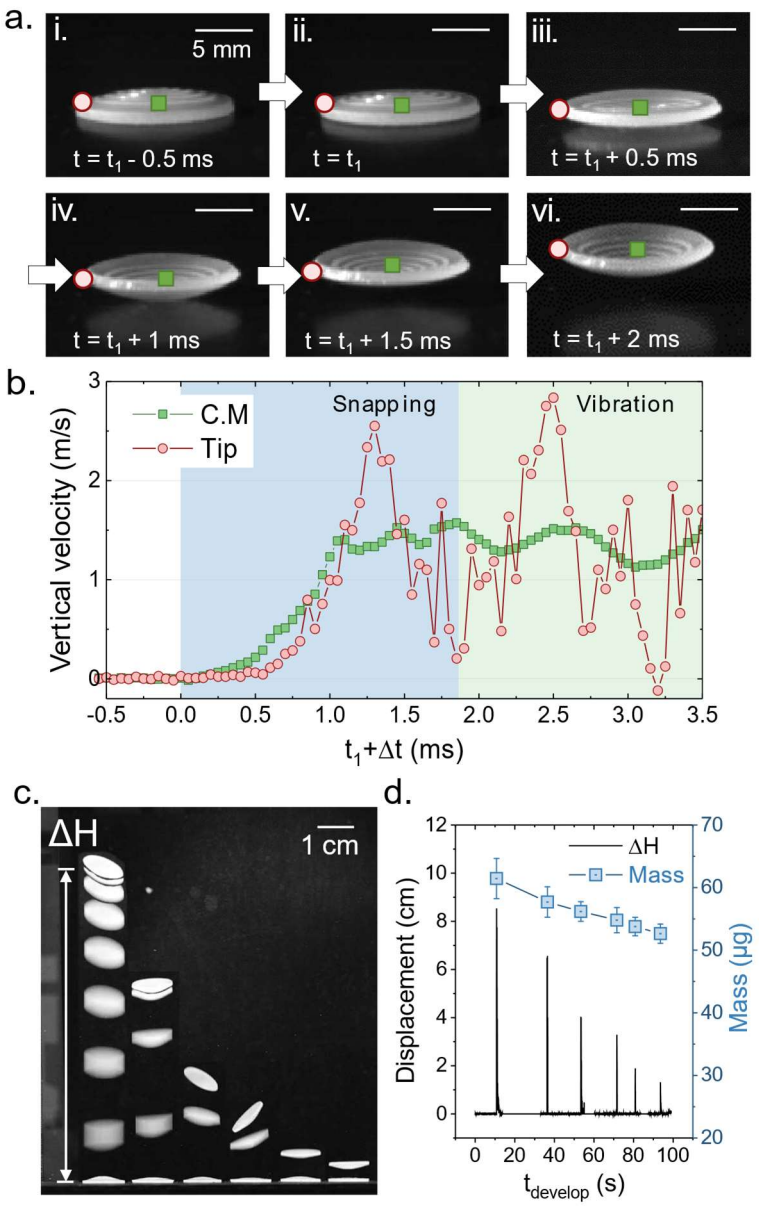

Figure 0.50 Details of the dynamic performances of hemispherical shell jumping on a substrate. (a) Time-lapse images of snap-transition of a hemispherical shell (R_0 = 4 mm, h_0 = 0.6 mm, t_{prep} = 40 s) taken with a high-speed camera (interval between frames = 0.5 ms). (b) Plot of the vertical speed changes of one endpoint (tip, square) and the center of mass (C.M, circle). (c) Time-lapse images (interval = 0.33 s) of consecutive snap jumping motions of a hemispherical shell (R_0 = 5 mm, h_0 = 0.6 mm, t_{prep} = 180 s) without re-swelling of solvent. (d) A plot of the vertical jumping height and the weight changes of the shell in (c) (the average of the measured weights for 5 runs of experiments on the same shell).

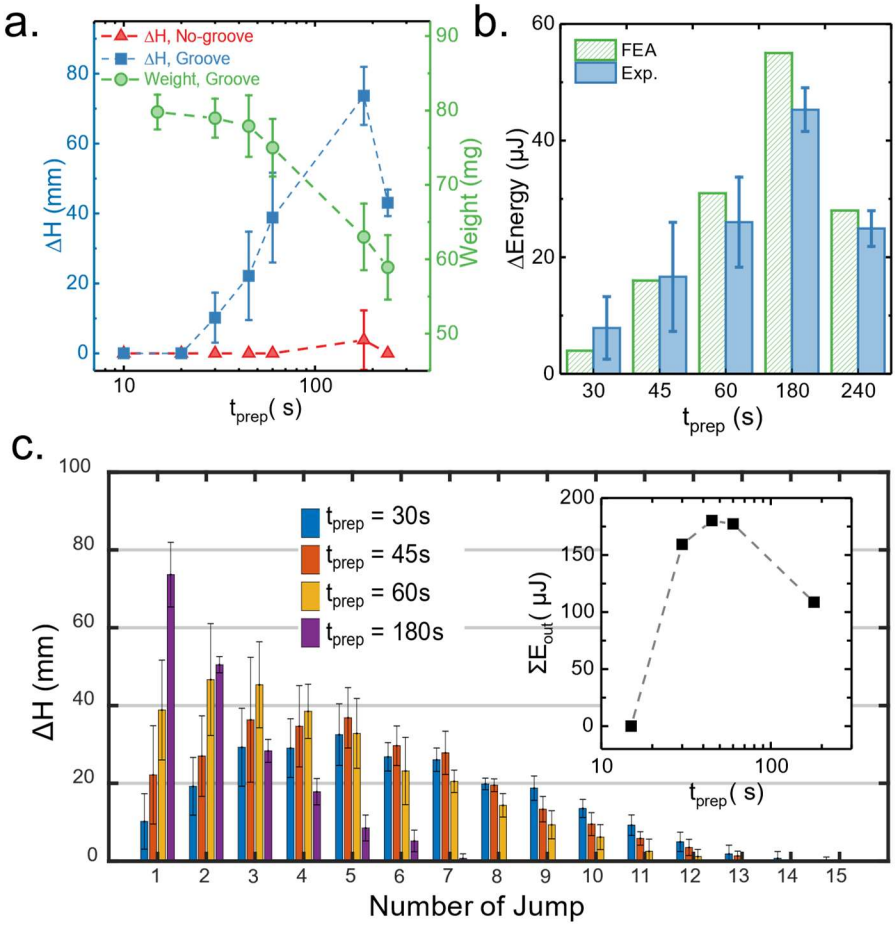

Figure 0.51 Dynamic performances of the first jumps of hemispherical shells (R_0 = 5 mm, h_0 = 0.6 mm) prepared at different initial de-swelling conditions. (a) A plot of the vertical jump heights (Square: groove, Triangle: no-groove) and the weight changes (circle) of the grooved shell prepared at different initial de-swelling times (n = 5 or 6) (b) The output energy of the real system (filled) calculated based on the potential energy change of the shells during jumping. (c) Plots of consecutive jumping heights and the output energy calculated based on the mass and jumping height.

Note that the shells with small lateral confinement due to the short de-swelling times ($t_{prep} \leqq 20$ s) only underwent smooth transitions, without snapping, to the inversely curved structure. Also, discs without grooves could not undergo snap-through transitions even after 60 seconds of preparation time supporting the effect of groove

patterns on increasing the ratio of in-plane stretching stiffness to out-of-plane bending stiffness (Figure 4.13a).

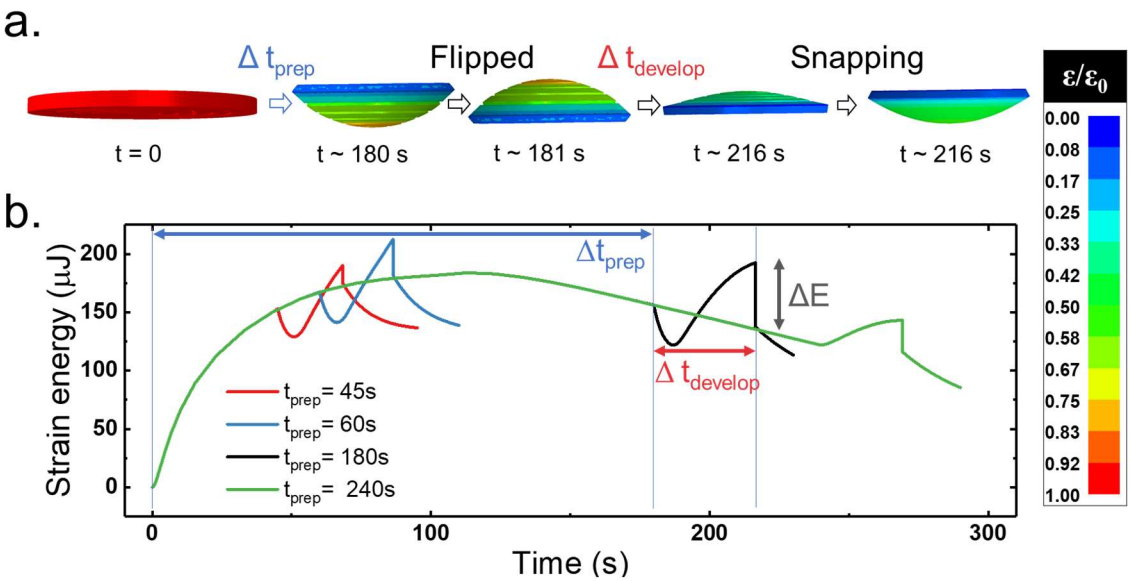

Figure 0.52 Snap-jumping phenomena of a PDMS disk (R_0 = 5 mm, h_0 = 0.6 mm, ε_{eq} = 0.43) analyzed by the finite element model. (a) The swelling ratio (ε) and shape change of the disk during asymmetric deswelling (t_{prep} = 180 s), and the consecutive snapping. (b) Plots of the strain energy in the function of different preparation conditions (t_{prep} = 45 ~ 240 s).

Snap-jumping phenomena of a PDMS disk (R_0 = 5 mm, h_0 = 0.6 mm, ε_{eq} = 0.43) were analyzed by the finite element model developed in section 4.6.1. The swelling ratio (ε) and shape change of the disk during asymmetric deswelling (t_{prep} = 180 s), and the consecutive snapping were presented in Figure 4.14. The model predicted that the disk will undergo a snap-buckling transition at about 35 seconds later being flipped, it was corresponding to experiments (36 ± 2 s.). A sudden ($\Delta t < 10^{-6}$ s) curvature change was predicted by the model in contrast to the experimental value (~ 2 ms). The discrepancy originates from the neglection of inertia effect in the modelling. In Figure 4.14b, strain energy change of the disk at different preparation conditions (t_{prep} = 45 ~ 240 s) was plotted. After a certain period of time for developing transition forces, sudden drop of

elastic energy was accompanied by the curvature change. The extent of elastic energy drop corresponded to the potential energy change calculated in Figure 4.13b, which represents that most of energy for snap-jumping was Considering the energy loss due to the adhesion between the substrate and the frictional loss by the air, the agreement between the experimental results and the numeric model was remarkable.

The key development of the designed snapping shells presented here is the ability to achieve multiple snap-through jump transitions without additional solvent, or fuel. We measured the output energy of each jump of shells with the same geometry but different times of preparation in order to demonstrate the ability to optimize the cumulative energy transferred from a single device (Figure 4.13c). Although the maximum first jump height was acquired for t_{prep} ~ 180 s, the maximum energy transferred occurred for discs with t_{prep} ~ 45 s (ΔE_{total} ~ 180 μJ).

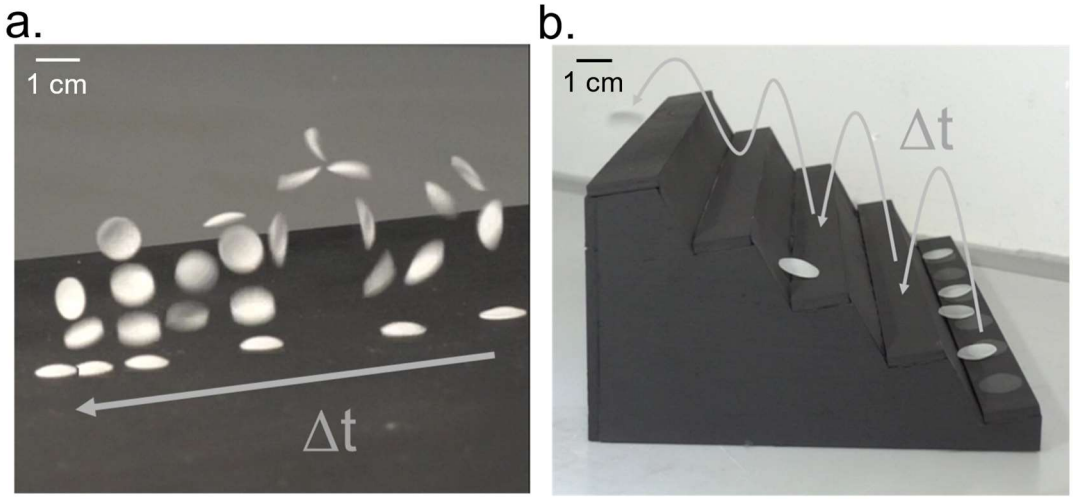

Figure 0.53 Application of the autonomous snapping mechanism for the various performance requirements and purposes. (a) A snapping shell going down a sloped substrate (angle ~ 6°) demonstrating a strategy of translating vertical displacement to horizontal displacement (b) Strategies for overcoming performance limits in the system. Using the ability of repeatable jumps, a potential limit in the jump height (~ 85 mm) of snapping shell was overcome.

The autonomous snapping mechanism can be used to complete complex tasks. For example, the vertical displacement of a jumping shell was directed into horizontal displacement with consecutive snap-jumps occurring on a sloped substrate (Figure 4.15a). Additionally, multiple smaller vertical jumps were used to climb a ladder autonomously (Figure 4.15b).

4.6.4 **Controlled biasing for the improved probability of multiple jumps**

Since we utilized the asymmetric evaporation rate of solvent between the convex surface, which is exposed to air, and the concave surface, which is covered by a substrate, to build large transition force for snap-through buckling transition, the probability of landing in the right position (concave-down) is important for the autonomous repeatable jumping.

We tested several ideas to increase the probability of repeatable jumping by biasing the landing position, such as blowing of air from the side to control the stability of landing position, connecting two jumping shells to make at least one jumping shell have concave-down position, or controlling the slope of substrate to roll down the concave surface.

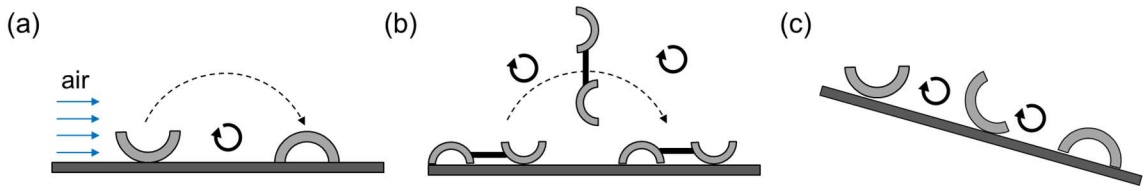

Figure 0.54 Schematics of various methods tested for biasing preferred landing position of jumping shells to improve the probability of autonomous repeatable jumping. (a) Blowing of air from one side (b) Connecting two jumping shells to increase the probability of proper landing (c) Sloped substrate to control the stability of landing position

4.7 Conclusions

In this contribution, we presented novel design principles for fabricating autonomously controlled power amplified polymer gel devices. We utilized meta-stable structures and asymmetric transformation paths, occurring during the deswelling of a polymer gel, to generate repeated, high-speed motion that could be harnessed to achieve multiple, autonomous jumping events. Most importantly, the principles outlined here provide a broad base for utilizing appropriately designed snap-through structures for a variety of energy-efficient movements.

4.8 Acknowledgement

Y. Kim would like to thank Jay van den Berg for the collaboration on the fabrication of snap-jumping shells and testing apparatus, and the data collections on the kinematics of jumping shells. This material is based upon work supported by, or in part by, the U. S. Army Research Laboratory and the U. S. Army Research Office under contract/grant number W911NF-15-1-0358.

CHAPTER 5

CONCLUDING REMARKS

5.1 Summary of work

The work presented in this thesis is focused on understanding how material properties and geomtery are related to impulsive motion of syntheitic systems. Specifically, we have focused on two goals: 1) establish the principles of fabrication for impulsive components, and, 2) resolve the roles of materials properties and geometry for achieving asymmetric energy flow.

We used scalable fabrication methods, such as flow coating, molding, laser cutting and engraving to prepare polymeric gels with asymmetric cross-sectional geometries. We utilized unbalanced distribution of surface-mediated stresses, including interfacial tension and surface swelling-indued compression across the neutral bending axis of a polymeric gel to induce global bending deformation of the object. These new design concepts aided us in fabricating unprecedented mesoscale actuators that can exhibit large system strain change and fast helical contraction in response to various types of stimuli.

We analyzed the surface stress-induced bending of polymeric gels by numerical and analytical methods. With these efforts, we could describe the underlying materials and geometric mechanisms. Scaling laws and numerical models were developed and harnessed to model various non-equilibrium swelling-induced deformations, including snap-driven jumping devices.

We developed a model impulsive system, which integrates important impulsive components: latching mechanism (bi-stable buckling), motor (drying stress), spring (elastic buckling), and energy supply (solvent swelling), within a single-body system. Non-equilibrium swelling states were harnessed to induce transient buckling of thin polymeric gels. Taking advantages of buckling instabilities, the intrinsic scaling relation between the size of system and the speed of swelling-induced motion was overcome, which were the main drawbacks of typical polymeric gel actuators. Furthermore, continous change in the swelling state of polymeric gels was utilized to generate autonomous, snap-through buckling transitions of the transiently buckled gels. These devices, and the broader underlying design principles, provide the first demonstration of an autonomous, self-regenerating high-speed movement, marking a significant advance in the development of energy-efficient, high speed motion important for microscale robots and actuated devices.

5.2 Future directions

While this thesis does answer many questions related to the influence of materials and geometries in the surface-stress induced dynamic shape-change phenomena of polymeric gels, it also leaves many open questions and future experiments. In this section, we propose some significant questions that need to be examined for the development of the design principle and other relevant researches on polymeric gels.

Regarding the stimuli-responsive helical contraction of mesoribbons, we have pointed out the significant influence of stimuli dynamics on the speed of helical contraction. We have confirmed this influence by conducting experiments under two different stimuli conditions: slow temperature ramping and fast pH change. However,

studies on the dynamics of stimuli were limited due to the difficulties in measuring fast, local change of temperature or pH. We predict that helical contractions would be accelerated by the use of faster stimuli conditions, such as light-assisted phase transition, including plasmonic heating or light-responsive phase transition (e.g., spyropyran-based dynamic materials [103, 136–138]). We have tried to incorporate gold nanoparticles or copolymers of NIPAm-spiropyran derivatives to mesoribbons, but failed to create discrete, well-defined mesoribbons by flow coating. We assumed that the incompatibility between the material and the substrate (glass) or sacrificial layer (polyvinyl alcohol) prevented the formation of well-defined mesoribbons. If this problem was overcome, the fabrication of remotely and locally controllable helical actuators with potentially improved kinetic performances would be possible.

In this thesis, we did not rigorously exploit the advantages of the different path of bending between the transient swelling process and transient deswelling process. The opposite sign of bending, for example, would be useful for creating self-tying structures or self-locking structures applicable for suturing wounds or self-healing of microscale devices. The dependence on the stimuli dynamics would be useful for creating chemical sensors or temperature sensors that react to the gradient of stimulus change.

We have open questions regarding the snapping shells as well. We have tried to realize the snap-jumping mechanism with hydrogel and water since the efficient utilization of ambient heat and abundant resources would result in the development of new types of energy harvesting devices [139].

BIBLIOGRAPHY

[1] L. Ionov, Polymeric Actuators. *Langmuir*. **31**, 5015–5024 (2015).

[2] A. O'Halloran, F. O'Malley, P. McHugh, A review on dielectric elastomer actuators, technology, applications, and challenges. *J. Appl. Phys.* **104**, 1–10 (2008).

[3] M. Elwenspoek, R. Legtenberg, a W. Groeneveld, "Comb-drive actuators for large displacements" (1999).

[4] A. . Fallis, *Piezoelectric ceramics* (Academic Press, 2013), vol. 53.

[5] W. L. Benard, H. Kahn, A. H. Heuer, M. A. Huff, Thin-film shape-memory alloy actuated micropumps. *J. Microelectromechanical Syst.* **7**, 245–251 (1998).

[6] A. Lendlein, R. Langer, Biodegradable, elastic shape-memory polymers for potential biomedical applications. *Science.* **296**, 1673–1676 (2002).

[7] H. Yuk, S. Lin, C. Ma, M. Takaffoli, N. X. Fang, X. Zhao, Hydraulic hydrogel actuators and robots optically and sonically camouflaged in water. *Nat. Commun.* **8**, 14230 (2017).

[8] S. Russo, T. Ranzani, C. J. Walsh, R. J. Wood, An Additive Millimeter-Scale Fabrication Method for Soft Biocompatible Actuators and Sensors. *Adv. Mater. Technol.* **2**, 1700135 (2017).

[9] R. K. Katzschmann, J. DelPreto, R. MacCurdy, D. Rus, Exploration of underwater life with an acoustically controlled soft robotic fish. *Sci. Robot.* **3**, eaar3449 (2018).

[10] G. N. T. Brian, J. A., Paul, E. K., and Collin, *Plants in Action: Adaptation in Nature, Performance in Cultivation* (Macmillan Education Australia, 2010).

[11] S. Armon, E. Efrati, R. Kupferman, E. Sharon, Geometry and mechanics in the opening of chiral seed pods. *Science.* **333**, 1726–1729 (2011).

[12] Y. Forterre, J. M. Skotheim, J. Dumals, L. Mahadevan, How the Venus flytrap snaps. *Nature*. **433**, 421–425 (2005).

[13] E. Reyssat, L. Mahadevan, Hygromorphs: From pine cones to biomimetic bilayers. *J. R. Soc. Interface*. **6**, 951–957 (2009).

[14] W. K. Silk, On the curving and twining of stems. *Environ. Exp. Bot.* **29**, 95–109 (1989).

[15] L. Ionov, Hydrogel-based actuators: Possibilities and limitations. *Mater. Today*. **17** (2014), pp. 494–503.

[16] R. M. Erb, J. S. Sander, R. Grisch, A. R. Studart, Self-shaping composites with programmable bioinspired microstructures. *Nat. Commun.* **4**, 1712 (2013).

[17] A. Sydney Gladman, E. A. Matsumoto, R. G. Nuzzo, L. Mahadevan, J. A. Lewis, Biomimetic 4D printing. *Nat. Mater.* **15**, 413–8 (2016).

[18] S. P. Timoshenko, J. M. Gere, *Theory Of Elastic Stability 2E* (Dover Publications, 1963).

[19] A. Pandey, D. E. Moulton, D. Vella, D. P. Holmes, Dynamics of snapping beams and jumping poppers. *Epl*. **105**, 24001 (2014).

[20] D. Chen, J. Yoon, D. Chandra, A. J. Crosby, R. C. Hayward, Stimuli-responsive buckling mechanics of polymer films. *J. Polym. Sci. Part B Polym. Phys.* **52**, 1441–1461 (2014).

[21] Y. Klein, E. Efrati, E. Sharon, Shaping of elastic sheets by prescription of non-Euclidean metrics. *Science.* **315**, 1116–1120 (2007).
[22] J. Kim, J. a. Hanna, M. Byun, C. D. Santangelo, R. C. Hayward, Designing Responsive Buckled Surfaces by Halftone Gel Lithography. *Science.* **335**, 1201–1205 (2012).
[23] J. H. Na, N. P. Bende, J. Bae, C. D. Santangelo, R. C. Hayward, Grayscale gel lithography for programmed buckling of non-Euclidean hydrogel plates. *Soft Matter*. **12**, 4985–4990 (2016).
[24] J. H. Na, A. A. Evans, J. Bae, M. C. Chiappelli, C. D. Santangelo, R. J. Lang, T. C. Hull, R. C. Hayward, Programming reversibly self-folding origami with micropatterned photo-crosslinkable polymer trilayers. *Adv. Mater.* **27**, 79–85 (2015).
[25] P. J. Flory, J. Rehner, in *The Journal of Chemical Physics* (1943), vol. 11, pp. 512–520.
[26] Y. Hu, X. Chen, G. M. Whitesides, J. J. Vlassak, Z. Suo, Indentation of polydimethylsiloxane submerged in organic solvents. *J. Mater. Res.* **26**, 785–795 (2011).
[27] M. A. Biot, General theory of three-dimensional consolidation. *J. Appl. Phys.* **12**, 155–164 (1941).
[28] J. Yoon, S. Cai, Z. Suo, R. C. Hayward, Poroelastic swelling kinetics of thin hydrogel layers: Comparison of theory and experiment. *Soft Matter*. **6**, 6004–6012 (2010).
[29] G. W. Scherer, Measurement of permeability I. Theory. *J. Non. Cryst. Solids*. **113**, 107–118 (1989).
[30] N. Bouklas, R. Huang, Swelling kinetics of polymer gels: Comparison of linear and nonlinear theories. *Soft Matter*. **8**, 8194–8203 (2012).
[31] J. W. Gibbs, On the equilibrium of heterogeneous substances. *Am. J. Sci.* **s3-16**, 441–458 (1878).
[32] W. Hong, X. Zhao, J. Zhou, Z. Suo, A theory of coupled diffusion and large deformation in polymeric gels. *J. Mech. Phys. Solids*. **56**, 1779–1793 (2008).
[33] W. Hong, Z. Liu, Z. Suo, Inhomogeneous swelling of a gel in equilibrium with a solvent and mechanical load. *Int. J. Solids Struct.* **46**, 3282–3289 (2009).
[34] D. P. Holmes, M. Roché, T. Sinha, H. A. Stone, Bending and twisting of soft materials by non-homogenous swelling. *Soft Matter*. **7**, 5188–5193 (2011).
[35] J. M. Skotheim, L. Mahadevan, Plant science: Physical limits and design principles for plant and fungal movements. *Science.* **308**, 1308–1310 (2005).
[36] X. Yang, G. Li, T. Cheng, Q. Zhao, C. Ma, T. Xie, T. Li, W. Yang, Bio-Inspired Fast Actuation by Mechanical Instability of Thermoresponding Hydrogel Structures. *J. Appl. Mech.* **83**, 071005 (2016).
[37] S. Jiang, F. Liu, A. Lerch, L. Ionov, S. Agarwal, Unusual and Superfast Temperature-Triggered Actuators. *Adv. Mater.* **27**, 4865–4870 (2015).
[38] Q. Zhao, X. Yang, C. Ma, D. Chen, H. Bai, T. Li, W. Yang, T. Xie, A bioinspired reversible snapping hydrogel assembly. *Mater. Horizons*. **3**, 422–428 (2016).
[39] C. S. Haines, N. Li, G. M. Spinks, A. E. Aliev, J. Di, R. H. Baughman, New twist on artificial muscles. *Proc. Natl. Acad. Sci.* **113**, 11709–11716 (2016).
[40] C. S. Haines, M. D. Lima, N. Li, G. M. Spinks, J. Foroughi, J. D. Madden, S. H.

Kim, S. Fang, M. Jung de Andrade, F. Goktepe, O. Goktepe, S. M. Mirvakili, S. Naficy, X. Lepro, J. Oh, M. E. Kozlov, S. J. Kim, X. Xu, B. J. Swedlove, G. G. Wallace, R. H. Baughman, Artificial muscles from fishing line and sewing thread. *Science.* **343**, 868–872 (2014).

[41] A. Upadhyaya, M. Baraban, J. Wong, P. Matsudaira, A. Van Oudenaarden, L. Mahadevan, Power-limited contraction dynamics of Vorticella convallaria: An ultrafast biological spring. *Biophys. J.* **94**, 265–272 (2008).

[42] Y. Moriyama, H. Okamoto, H. Asai, Rubber-like elasticity and volume changes in the isolated spasmoneme of giant Zoothamnium sp. under Ca2+-induced contraction. *Biophys. J.* **76**, 993–1000 (1999).

[43] K. M. Halanych, Invertebrates; Invertebrate Zoology: A Functional Evolutionary Approach. *Syst. Biol.* **53**, 662–664 (2004).

[44] S. Ryu, P. Matsudaira, Unsteady Motion, Finite Reynolds Numbers, and Wall Effect on Vorticella convallaria Contribute Contraction Force Greater than the Stokes Drag. *Biophys. J.* **98**, 2574–2581 (2010).

[45] J. T. Pham, J. Lawrence, D. Y. Lee, G. M. Grason, T. Emrick, A. J. Crosby, Highly stretchable nanoparticle helices through geometric asymmetry and surface forces. *Adv. Mater.* **25**, 6703–6708 (2013).

[46] J. T. Pham, A. Morozov, A. J. Crosby, A. Lindner, O. Du Roure, Deformation and shape of flexible, microscale helices in viscous flow. *Phys. Rev. E - Stat. Nonlinear, Soft Matter Phys.* **92**, 1–5 (2015).

[47] D. M. Barber, A. J. Crosby, T. Emrick, Mesoscale Block Copolymers. *Adv. Mater.* **30**, 1706118 (2018).

[48] S. Mora, C. Maurini, T. Phou, J. M. Fromental, B. Audoly, Y. Pomeau, Solid drops: Large capillary deformations of immersed elastic rods. *Phys. Rev. Lett.* **111**, 114301 (2013).

[49] S. Douezan, M. Wyart, F. Brochard-Wyart, D. Cuvelier, Curling instability induced by swelling. *Soft Matter*. **7**, 1506–1511 (2011).

[50] Z. Ding, W. Toh, J. Hu, Z. Liu, T. Y. Ng, A simplified coupled thermo-mechanical model for the transient analysis of temperature-sensitive hydrogels. *Mech. Mater.* **97**, 212–227 (2016).

[51] F. Lai, H. Li, Transient modeling of the reversible response of the hydrogel to the change in the ionic strength of solutions. *Mech. Mater.* **43**, 287–298 (2011).

[52] W. Toh, Z. Liu, T. Y. Ng, W. Hong, Inhomogeneous Large Deformation Kinetics of Polymeric Gels. *Int. J. Appl. Mech.* **05**, 1350001 (2013).

[53] Z. Duan, J. Zhang, Y. An, H. Jiang, Simulation of the Transient Behavior of Gels Based on an Analogy Between Diffusion and Heat Transfer. *J. Appl. Mech.* **80**, 041017 (2013).

[54] J. Zhang, X. Zhao, Z. Suo, H. Jiang, A finite element method for transient analysis of concurrent large deformation and mass transport in gels. *J. Appl. Phys.* **105**, 093522 (2009).

[55] W. Toh, Z. Ding, T. Yong Ng, Z. Liu, Wrinkling of a Polymeric Gel During Transient Swelling. *J. Appl. Mech.* **82**, 061004 (2015).

[56] D. De Kee, Q. Liu, J. Hinestroza, Viscoelastic (Non-Fickian) Diffusion. *Can. J. Chem. Eng.* **83**, 913–929 (2005).

[57] M. Parti, Mass transfer biot numbers. *Period. Polytech. Mech. Eng.* **38**, 109–122

(1994).
[58] J. N. Lee, C. Park, G. M. Whitesides, Solvent Compatibility of Poly(dimethylsiloxane)-Based Microfluidic Devices. *Anal. Chem.* **75**, 6544–6554 (2003).
[59] V. Pratt, in *ACM SIGGRAPH Computer Graphics* (ACM Press, New York, New York, USA, 2005), vol. 21, pp. 145–152.
[60] S. P. Obukhov, M. Rubinstein, R. H. Colby, Network Modulus and Superelasticity. *Macromolecules*. **27**, 3191–3198 (1994).
[61] P. J. Flory, Thermodynamics of High Polymer Solutions. *J. Chem. Phys.* **9**, 660–660 (1941).
[62] M. L. Huggins, Solutions of Long Chain Compounds. *J. Chem. Phys.* **9**, 440–440 (1941).
[63] Y. Hu, X. Zhao, J. J. Vlassak, Z. Suo, Using indentation to characterize the poroelasticity of gels. *Appl. Phys. Lett.* **96**, 121904 (2010).
[64] J. Zhang, X. Zhao, Z. Suo, H. Jiang, A finite element method for transient analysis of concurrent large deformation and mass transport in gels. *J. Appl. Phys.* **105**, 1–9 (2009).
[65] W. Toh, Z. Ding, T. Yong Ng, Z. Liu, Wrinkling of a Polymeric Gel During Transient Swelling. *J. Appl. Mech.* **82**, 061004 (2015).
[66] T. Mora, A. Boudaoud, Buckling of swelling gels. *Eur. Phys. J. E*. **20**, 119–124 (2006).
[67] B. Dortdivanlioglu, C. Linder, Diffusion-driven swelling-induced instabilities of hydrogels. *J. Mech. Phys. Solids*. **125**, 38–52 (2019).
[68] W. Hong, Z. Liu, Z. Suo, Inhomogeneous swelling of a gel in equilibrium with a solvent and mechanical load. *Int. J. Solids Struct.* **46**, 3282–3289 (2009).
[69] S. A. Chester, C. V. Di Leo, L. Anand, A finite element implementation of a coupled diffusion-deformation theory for elastomeric gels. *Int. J. Solids Struct.* **52**, 1–18 (2015).
[70] Y. Liu, H. Zhang, J. Zhang, Y. Zheng, Transient swelling of polymeric hydrogels: A new finite element solution framework. *Int. J. Solids Struct.* **80**, 246–260 (2016).
[71] J. L. Duda, J. S. Vrentas, S. T. Ju, H. T. Liu, Prediction of diffusion coefficients for polymer-solvent systems. *AIChE J.* **28**, 279–285 (1982).
[72] W. Shyy, H. Aono, S. K. Chimakurthi, P. Trizila, C.-K. Kang, C. E. S. Cesnik, H. Liu, Recent progress in flapping wing aerodynamics and aeroelasticity. *Prog. Aerosp. Sci.* **46**, 284–327 (2010).
[73] F. Delcomyn, Insect walking and robotics. *Annu. Rev. Entomol.* **49**, 51–70 (2004).
[74] N. T. Jafferis, E. F. Helbling, M. Karpelson, R. J. Wood, Untethered flight of an insect-sized flapping-wing microscale aerial vehicle. *Nature*. **570**, 491–495 (2019).
[75] J. D. W. Madden, N. a. Vandesteeg, P. a. Anquetil, P. G. a Madden, A. Takshi, R. Z. Pytel, S. R. Lafontaine, P. a. Wieringa, I. W. Hunter, Artificial muscle technology: Physical principles and naval prospects. *IEEE J. Ocean. Eng.* **29**, 706–728 (2004).
[76] D. S. Smith, The structure of intersegmental muscle fibers in an insect, Periplaneta americana L. *J. Cell Biol.* **29**, 449–459 (1966).
[77] A. R. Gillies, R. L. Lieber, Structure and function of the skeletal muscle extracellular matrix. *Muscle and Nerve*. **44** (2011), pp. 318–331.

[78] R. Chelakkot, A. Gopinath, L. Mahadevan, M. F. Hagan, Flagellar dynamics of a connected chain of active, polar, Brownian particles. *J. R. Soc. Interface*. **11**, 20130884 (2014).
[79] S. Ryu, R. E. Pepper, M. Nagai, D. C. France, Vorticella: A protozoan for bio-inspired engineering. *Micromachines*. **8** (2017), p. 4.
[80] E. M. Purcell, Life at low Reynolds number. *Am. J. Phys.* **45**, 3–11 (1977).
[81] T. Qiu, T. C. Lee, A. G. Mark, K. I. Morozov, R. Münster, O. Mierka, S. Turek, A. M. Leshansky, P. Fischer, Swimming by reciprocal motion at low Reynolds number. *Nat. Commun.* **5**, 5119 (2014).
[82] L. Mahadevan, P. Matsudaira, Motility powered by supramolecular springs and ratchets. *Science.* **288** (2000), pp. 95–99.
[83] T. WEIS-FOGH, W. B. AMOS, Evidence for a New Mechanism of Cell Motility. *Nature*. **236**, 301–304 (1972).
[84] M. Knoblauch, W. S. Peters, Biomimetic actuators: Where technology and cell biology merge. *Cell. Mol. Life Sci.* **61** (2004), pp. 2497–2509.
[85] X. Cheng, Y. Zhang, Micro/Nanoscale 3D Assembly by Rolling, Folding, Curving, and Buckling Approaches. *Adv. Mater.*, 1901895 (2019).
[86] Z. L. Wu, M. Moshe, J. Greener, H. Therien-Aubin, Z. Nie, E. Sharon, E. Kumacheva, Three-dimensional shape transformations of hydrogel sheets induced by small-scale modulation of internal stresses. *Nat. Commun.* **4**, 1586 (2013).
[87] H. Li, C. Tan, L. Li, Review of 3D printable hydrogels and constructs. *Mater. Des.* **159**, 20–38 (2018).
[88] H. S. Kim, C. H. Lee, P. K. Sudeep, T. Emrick, A. J. Crosby, Nanoparticle stripes, grids, and ribbons produced by flow coating. *Adv. Mater.* **22**, 4600–4604 (2010).
[89] S. W. Hong, J. Xia, Z. Lin, Spontaneous formation of mesoscale polymer patterns in an evaporating bound solution. *Adv. Mater.*, 1413–1417 (2007).
[90] C. Wu, X. Wang, Globule-to-coil transition of a single homopolymer chain in solution. *Phys. Rev. Lett.* **80**, 4092–4094 (1998).
[91] K. Zhou, Y. Lu, J. Li, L. Shen, G. Zhang, Z. Xie, C. Wu, The Coil-to-Globule-to-Coil Transition of Linear Polymer Chains in Dilute Aqueous Solutions: Effect of Intrachain Hydrogen Bonding. *Macromolecules*. **41**, 8927–8931 (2008).
[92] E. A. Clark, J. E. G. Lipson, LCST and UCST behavior in polymer solutions and blends. *Polymer*. **53**, 536–545 (2012).
[93] N. A. Platé, T. L. Lebedeva, L. I. Valuev, Lower critical solution temperature in aqueous solutions of N-alkyl-substituted polyacrylamides. *Polym. J.* **31**, 21–27 (1999).
[94] Y. Katsumoto, T. Tanaka, K. Ihara, M. Koyama, Y. Ozaki, Contribution of intramolecular C=O···H-N hydrogen bonding to the solvent-induced reentrant phase separation of poly(N-isopropylacrylamide). *J. Phys. Chem. B*. **111**, 12730–12737 (2007).
[95] L. Chen, M. Liu, L. Lin, T. Zhang, J. Ma, Y. Song, L. Jiang, Thermal-responsive hydrogel surface: Tunable wettability and adhesion to oil at the water/solid interface. *Soft Matter*. **6**, 2708–2712 (2010).
[96] D. Cunliffe, C. De Las Heras Alarcón, V. Peters, J. R. Smith, C. Alexander, Thermoresponsive surface-grafted poly(N-isopropylacrylamide) copolymers: Effect of phase transitions on protein and bacterial attachment. *Langmuir*. **19**,

2888–2899 (2003).
[97] Y. Dong, X. Zhu, F. Shi, J. Nie, Surface photo-anchored PNIPAM crosslinked membrane on glass substrate by covalent bonds. *Appl. Surf. Sci.* **307**, 7–12 (2014).
[98] V. P. Gilcreest, W. M. Carroll, Y. A. Rochev, I. Blute, K. A. Dawson, A. V. Gorelov, Thermoresponsive poly(N-isopropylacrylamide) copolymers: Contact angles and surface energies of polymer films. *Langmuir*. **20**, 10138–10145 (2004).
[99] K. N. Plunkett, X. Zhu, J. S. Moore, D. E. Leckband, PNIPAM chain collapse depends on the molecular weight and grafting density. *Langmuir*. **22**, 4259–4266 (2006).
[100] R. Pelton, Poly(N-isopropylacrylamide) (PNIPAM) is never hydrophobic. *J. Colloid Interface Sci.* **348**, 673–674 (2010).
[101] R. Pelton, Temperature-sensitive aqueous microgels. *Adv. Colloid Interface Sci.* **85**, 1–33 (2000).
[102] J. Zhang, L. Y. Chu, Y. K. Li, Y. M. Lee, Dual thermo- and pH-sensitive poly(N-isopropylacrylamide-co-acrylic acid) hydrogels with rapid response behaviors. *Polymer*. **48**, 1718–1728 (2007).
[103] A. Garcia, M. Marquez, T. Cai, R. Rosario, Z. Hu, D. Gust, M. Hayes, S. A. Vail, C. Do Park, Photo-, thermally, and pH-responsive microgels. *Langmuir*. **23**, 224–229 (2007).
[104] A. Ahiabu, M. J. Serpe, Rapidly Responding pH-and Temperature-Responsive Poly (N-Isopropylacrylamide)-Based Microgels and Assemblies. *ACS Omega*. **2**, 1769–1777 (2017).
[105] D. Y. Lee, J. T. Pham, J. Lawrence, C. H. Lee, C. Parkos, T. Emrick, A. J. Crosby, Macroscopic Nanoparticle Ribbons and Fabrics. *Adv. Mater.* **25**, 1248–1253 (2013).
[106] S. Choudhary, J. Pham, A. Crosby, MESOSCALE POLYMER ASSEMBLIES Materials Research Science and Engineering on Polymers Polymer Poster Symposium (2013).
[107] D. Y. Lee, J. T. Pham, J. Lawrence, C. H. Lee, C. Parkos, T. Emrick, A. J. Crosby, Macroscopic nanoparticle ribbons and fabrics. *Adv. Mater.* **25**, 1248–1253 (2013).
[108] H. S. Kim, C. H. Lee, P. K. Sudeep, T. Emrick, A. J. Crosby, Nanoparticle stripes, grids, and ribbons produced by flow coating. *Adv. Mater.* **22**, 4600–4604 (2010).
[109] S. K. Wu, J. F. Rabek, Benzophenone-initiated photo-crosslinking of polynorbornene in the solid state. *Polym. Degrad. Stab.* **21**, 365–376 (1988).
[110] J. Kim, J. A. Hanna, M. Byun, C. D. Santangelo, R. C. Hayward, Designing responsive buckled surfaces by halftone gel lithography. *Science.* **335**, 1201–1205 (2012).
[111] Y. Hu, E. P. Chan, J. J. Vlassak, Z. Suo, Poroelastic relaxation indentation of thin layers of gels. *J. Appl. Phys.* **110**, 086103 (2011).
[112] J. Liu, J. Huang, T. Su, K. Bertoldi, D. R. Clarke, Structural transition from helices to hemihelices. *PLoS One*. **9** (2014).
[113] J. Huang, J. Liu, B. Kroll, K. Bertoldi, D. R. Clarke, Spontaneous and deterministic three-dimensional curling of pre-strained elastomeric bi-strips. *Soft Matter*. **8**, 6291–6300 (2012).
[114] S. Mondal, M. Phukan, A. Ghatak, Estimation of solid–liquid interfacial tension using curved surface of a soft solid. *Proc. Natl. Acad. Sci.* **112**, 12563–12568

(2015).
[115] J. Zhang, R. Pelton, Y. Deng, Temperature-Dependent Contact Angles of Water on Poly(N-isopropylacrylamide) Gels. *Langmuir*. **11**, 2301–2302 (1995).
[116] M. Kim, T. R. Powers, Deformation of a helical filament by flow and electric or magnetic fields. *Phys. Rev. E*. **71**, 021914 (2005).
[117] J. Bae, J. H. Na, C. D. Santangelo, R. C. Hayward, Edge-defined metric buckling of temperature-responsive hydrogel ribbons and rings. *Polymer*. **55**, 5908–5914 (2014).
[118] H. G. Schild, M. Muthukumar, D. A. Tirrell ', Cononsolvency in Mixed Aqueous Solutions of. *Macromol. J. Chem. Phys*. **24**, 948–952 (1991).
[119] C. Scherzinger, A. Schwarz, A. Bardow, K. Leonhard, W. Richtering, Cononsolvency of poly-N-isopropyl acrylamide (PNIPAM): Microgels versus linear chains and macrogels. *Curr. Opin. Colloid Interface Sci.* **19**, 84–94 (2014).
[120] R. O. R. Costa, R. F. S. Freitas, Phase behavior of poly (N-isopropylacrylamide) in binary aqueous solutions. *Polymer*. **43**, 5879–5885 (2002).
[121] G. Vazquez, E. Alvarez, J. M. Navaza, Surface Tension of Alcohol + Water from 20 to 50 °C. *J. Chem. Eng. Data*. **40**, 611–614 (1995).
[122] M. Ilton, M. Saad Bhamla, X. Ma, S. M. Cox, L. L. Fitchett, Y. Kim, J. sung Koh, D. Krishnamurthy, C. Y. Kuo, F. Z. Temel, A. J. Crosby, M. Prakash, G. P. Sutton, R. J. Wood, E. Azizi, S. Bergbreiter, S. N. Patek, The principles of cascading power limits in small, fast biological and engineered systems. *Science.* **360**, eaao1082 (2018).
[123] S. J. Gerbode, J. R. Puzey, A. G. McCormick, L. Mahadevan, How the Cucumber Tendril Coils and Overwinds. *Science.* **337**, 1087–1091 (2012).
[124] S. Poppinga, L. E. Daber, A. S. Westermeier, S. Kruppert, M. Horstmann, R. Tollrian, T. Speck, Biomechanical analysis of prey capture in the carnivorous Southern bladderwort (Utricularia australis). *Sci. Rep.* **7**, 1–10 (2017).
[125] S. Poppinga, C. Weisskopf, A. S. Westermeier, T. Masselter, T. Speck, Fastest predators in the plant kingdom: Functional morphology and biomechanics of suction traps found in the largest genus of carnivorous plants. *AoB Plants*. **8**, 1–25 (2016).
[126] D. P. Holmes, A. J. Crosby, Snapping surfaces. *Adv. Mater.* **19**, 3589–3593 (2007).
[127] H. Lee, C. Xia, N. X. Fang, First jump of microgel; Actuation speed enhancement by elastic instability. *Soft Matter*. **6**, 4342–4345 (2010).
[128] S. Maeda, Y. Hara, T. Sakai, R. Yoshida, S. Hashimoto, Self-walking gel. *Adv. Mater.* **19**, 3480–3484 (2007).
[129] R. Yoshida, Self-oscillating polymer gel as novel biomimetic materials exhibiting spatiotemporal structure. *Colloid Polym. Sci.* **289**, 475–487 (2011).
[130] D. W. Haldane, M. M. Plecnik, J. K. Yim, R. S. Fearing, Robotic vertical jumping agility via Series-Elastic power modulation. *Sci. Robot.* **1**, eaag2048 (2016).
[131] A. N. Zaikin, A. M. Zhabotinsky, Concentration wave propagation in two-dimensional liquid-phase self-oscillating system. *Nature*. **225**, 535–537 (1970).
[132] I. M. Smallwood, *Handbook of Organic Solvent Properties* (Butterworth-Heinemann, 2012).
[133] Z. Duan, J. Zhang, Y. An, H. Jiang, Simulation of the Transient Behavior of Gels

Based on an Analogy Between Diffusion and Heat Transfer. *J. Appl. Mech.* **80**, 041017 (2013).
[134] W. Thomson, 4. On the Equilibrium of Vapour at a Curved Surface of Liquid. *Proc. R. Soc. Edinburgh*. **7**, 63–68 (1872).
[135] J. P. Olberding, S. M. Deban, Effects of temperature and force requirements on muscle work and power output. *J. Exp. Biol.* **220**, 2017–2025 (2017).
[136] R. Klajn, Spiropyran-based dynamic materials. *Chem. Soc. Rev.* **43** (2014), pp. 148–184.
[137] B. Ziółkowski, L. Florea, J. Theobald, F. Benito-Lopez, D. Diamond, Self-protonating spiropyran-co-NIPAM-co-acrylic acid hydrogel photoactuators. *Soft Matter*. **9**, 8754–8760 (2013).
[138] J. E. Stumpel, D. Liu, D. J. Broer, A. P. H. J. Schenning, Photoswitchable hydrogel surface topographies by polymerisation-induced diffusion. *Chem. - A Eur. J.* **19**, 10922–10927 (2013).
[139] X. Chen, D. Goodnight, Z. Gao, A. H. Cavusoglu, N. Sabharwal, M. Delay, A. Driks, O. Sahin, Scaling up nanoscale water-driven energy conversion into evaporation-driven engines and generators. *Nat. Commun.* **6**, 1–7 (2015).